SYNTHESIS OF IRON(II) DOPED COPPER FERRITES AS NOVEL HETEROGENEOUS PHOTO-FENTON CATALYSTS

DOI:10.18136/PE.2021.785

Engr. Asfandyar Khan

Doctoral School of Chemical Engineering and Material Sciences

Research Group of Environmental and Inorganic Photochemistry

Center for Natural Sciences

University of Pannonia

Veszprém

2021

A dissertation submitted to University of Pannonia

for

the degree of Doctor of Philosophy

SYNTHESIS OF IRON(II) DOPED COPPER FERRITES AS NOVEL HETEROGENEOUS PHOTO-FENTON CATALYSTS

Thesis for obtaining a PhD degree in the Doctoral School of CHEMICAL ENGINEERING AND MATERIAL SCIENCES of the University of Pannonia

in the branch of ENGINEERING Sciences

Written by ASFANDYAR KHAN

Supervisor(s): Dr. OTTÓ HORVÁTH, DSc and Dr. ZSOLT VALICSEK, PhD

propose acceptance (yes / no) …….
[SIGNATURE(S) OF SUPERVISOR(S)]

As reviewer, I propose acceptance of the thesis:

Name of Reviewer: Dr. Sándor Kurunczi, PhD yes / no.…….
[REVIEWER]

Name of Reviewer: Dr. Gábor Kovács, PhD yes / no …….
[REVIEWER]

The PhD-candidate has achieved ….....% at the public discussion.

Veszprém/Keszthely,.....2021

…….
[SIGNATURE OF THE CHAIRMAN OF THE COMMITTEE]

The grade of the PhD Diploma …..... (…….. %)
Veszprém/Keszthely,.....2021

…….
[SIGNATURE OF THE CHAIRMAN OF UDHC]

Declaration

The undersigned ***"Asfandyar Khan"*** PhD student, declare that the thesis was made at the University of Pannonia, Center for Natural Sciences, Research Group of Environmental and Inorganic Photochemistry, Doctoral School of Chemical Engineering and Material Sciences, in order to obtain the Doctor of Philosophy degree in Bio, Environmental and Chemical Engineering.

I hereby declare upon my honour that the present thesis is entirely my intellectual property based on my own original ideas and I used only the sources which are listed in the bibliography. I have not submitted this thesis for any other thesis purpose before.

Veszprém,

Signature

The undersigned ***"Prof. Dr. Ottó Horváth and Dr. Zsolt Valicsek"***, as supervisors, declare that the thesis was made at the University of Pannonia, Center for Natural Sciences, Research Group of Environmental and Inorganic Photochemistry, in order to obtain the Doctor of Philosophy degree in Bio, Environmental and Chemical Engineering.

I declare that I authorize the PhD thesis.

Veszprém,

Signature

Abstract

Heterogeneous photo-Fenton type systems have got considerable fame in the field of wastewater treatment due to their reusability and appreciable photoactivity within a wide pH range. The present research investigates the synthesis and structural elucidation of simple metal oxides ($Cu^{II}O$, $Fe^{II}O$, $Fe^{III}_2O_3$) and iron(II)-doped copper ferrite ($Cu^{II}_{(x)}Fe^{II}_{(1-x)}Fe^{III}_2O_4$, x = 0, 0.2, 0.4, 0.6, 0.8, 1.0) nanoparticles (NPs) and their photocatalytic applications for the degradation of methylene blue (MB) and rhodamine B as model dyes.

The NPs were prepared via simple co-precipitation technique and calcination. The NPs were characterized by using Raman spectroscopy, X-ray diffractometry (XRD), scanning electron microscopy (SEM) combined with energy dispersive spectroscopy (EDS), inductively coupled plasma (ICP), Brunauer–Emmett–Teller (BET), and diffuse reflectance spectroscopy (DRS). SEM revealed the structural changes from the spherical-like particles into needle-like fine particles as the consequence of the increasing ratio of copper(II) in the ferrites, accompanied by the decrease of the optical band-gap energies from 2.02 to 1.25 eV. The specific surface areas of these catalysts were in a considerable correlation with their morphologies. Iron(II) doped copper ferrites exhibited an inverse spinel (instead of spinel) structure: metal ions with +2 charge (Fe^{2+} or Cu^{2+}) were in octahedral position, while half of the Fe^{3+} ions were in tetrahedral one. Inverse spinal structure does not change during the substitution of Cu^{2+} ions to Fe^{2+} in the iron(II) doped copper ferrites. Also, the inverse spinel structure was confirmed by Raman spectra of NPs.

All the simple metal oxides and doped ferrites were applied in heterogeneous photo-Fenton systems for MB degradation. NP-3 was confirmed to be the most efficient photocatalyst in the prepared series. Based on these experiments, the optimized reaction conditions, such as catalyst dosage, hydrogen peroxide concentration, and pH, were confirmed to be 400 mg/L, 1.76×10^{-1} mol/L, and 7.5, respectively. The UV-visible spectra of MB were recorded before and after degradation (at optimized conditions) and compared; the latter one revealed no peak in the UV/visible region, which clearly indicated the complete degradation of dye from the aqueous medium. It was also confirmed that at optimized conditions, all doped copper ferrites were photocatalytically active. Also, in the case of RhB, NP-3 proved to be the most efficient photocatalyst in the series prepared, and

the optimized reaction conditions, such as catalyst dosage, hydrogen peroxide concentration, and pH, were determined to be 500 mg/L, 8.88×10^{-2} mol/L, and 7.5, respectively. All doped copper ferrites were active photocatalysts at optimized conditions.

In five-cycle reusability experiments, NP-3 and composite ($Cu^{II}O/Fe^{II}O/Fe^{III}_2O_3$) showed increases of the apparent kinetic constant up to the third cycle. While the fourth and fifth cycles delivered slight decreases of the reaction rate in the case of NP-3, no significant increase for composite ($Cu^{II}O/Fe^{II}O/Fe^{III}_2O_3$) was observed. Both ICP measurements and spectrophotometry checked the leaching of metal ions into the solution phase. It was confirmed that less than 1% of metal ions remained in the aqueous solution after removing the catalyst.

Based on comparison studies, it can be concluded that NP-3, metal oxide composite ($Cu^{II}O/Fe^{II}O/Fe^{III}_2O_3$) and $Cu^{II}O$ alone have strong degradation potential for recalcitrant organic compounds. In addition simple metal oxides and all doped copper ferrites revealed appreciable antibacterial activities against the gram-negative bacterium *Vibrio fischeri* in a bioluminescence inhibition assay.

Abbreviations

AOPs	Advanced oxidation process
BET	Brunauer-Emmett-Teller
COD	Chemical oxygen demand
CB	Conduction band
DRS	Diffuse reflectance spectroscopy
DO	Dissolved oxygen
EDX	Energy dispersive X-ray
EDCs	Endocrine disrupting compounds
ICP-OES	Inductively coupled optical emission spectrometry
IR	Infrared radiations
MB	Methylene blue
MO	Methyl orange
NPs	Nanoparticles
PCPs	Personal care products
PSD	Particle size distribution
RR198	Reactive Red 198
RhB	Rhodamine B
RR120	Reactive Red 120
ROS	Reactive oxygen species
SEM	Scanning electron microscopy
UN	United Nations
USEPA	United States Environmental Protection Agency
UV	Ultraviolet radiations
VB	Valence band
XRD	X-ray diffractometry

Table of Contents

Declaration IV

Abstract V

Abbreviations VII

Table of Contents VIII

List of Tables XII

List of Figures XIII

1. Introduction 1

2. Literature review 4

2.1 Nanotechnology 4

2.2 Metal oxide nanoparticles 4

2.3 Advance oxidation processes (AOPs) 5

2.3.1 Fenton reaction 6

2.4 Photocatalysis 7

2.4.1 Heterogeneous photocatalysis 9

2.5 Ferrites 11

2.5.1 Copper ferrites 14

2.5.2 Mixed metal ferrites 15

2.5.3 Relation between ferrites structure and its catalytic properties 16

2.5.4 Applications of ferrites 17

2.5.4.1 Antibacterial property of ferrites 17

2.5.4.2 Removal of inorganic pollutants 18

2.5.4.3 Removal of organic pollutants 18

2.5.5 Methods for synthesizing ferrites NPs 19

2.5.5.1 Co-precipitation methods 20

2.5.5.2 Thermal methods 21
2.5.5.3 Sol-gel and citrate methods 21
2.5.5.4 Solid-state reaction methods 22
2.5.5.5 Microemulsion methods 23
2.6 Photocatalytic reactors 23
2.6.1 Structure of photocatalytic reactors in water remediation 24
2.6.2 Suspended and immobilized photocatalytic systems 24
2.6.3 Key operational parameters of a suspended photocatalytic reactor 25
2.6.3.1 Catalyst dosage 25
2.6.3.2 Temperature 26
2.6.3.3 pH 26
2.6.3.4 Dissolved oxygen (DO) 27
2.6.3.5 Concentration of contaminants 28
2.6.3.6 Wavelength of energy source and its intensity 28
2.7 Research objective 29
3. Materials and Methods 32
3.1 Materials 32
3.2 Fabrication of simple metal oxide and ferrite NPs 32
3.3 Experimental composition of NPs 35
3.4 Characterization of NPs 36
3.4.1 Inductively coupled plasma (ICP) measurements 36
3.4.2 X-ray diffraction (XRD) measurements 36
3.4.3 Determination of specific surface areas 37
3.4.4 Raman spectroscopic measurements 37
3.4.5 Scanning electron microscopy (SEM) 37

3.4.6 Energy dispersive X-ray spectroscopy (EDS) 38
3.4.7 Measurement of particle size distribution (PSD) 38
3.4.8 Diffuse reflectance spectroscopy (DRS) 38
3.5 Assessment of Photocatalytic Activity 39
3.5.1 Energy source and photo-reactor configuration 39
3.5.2 Photocatalytic experiments using methylene blue as model compound 39
3.5.3 Photocatalytic experiments using rhodamine b as model compound 41
3.6 Investigating the stability of catalysts 42
3.7 Investigating the reusability of catalysts 42
3.8 Total organic carbon (TOC) measurements 43
3.9 Antimicrobial assessments 43
4. Results and discussions 44
4.1 Assessment of the experimental Cu/Fe ratios in the synthesized catalysts 44
4.2 Characterization of simple metal oxides and iron(II) doped copper ferrites NPs 44
4.2.1 Particle size distribution (PSD) 44
4.2.2 X-ray diffraction (XRD) measurements 45
4.2.3 Raman measurements 49
4.2.4 Scanning electron microscopy (SEM) measurements 50
4.2.5 Energy dispersive x-ray (EDX) spectroscopy measurements 53
4.2.6 Determination of specific surface areas 57
4.2.7 Diffuse reflectance spectroscopy (DRS) measurements 58
4.3 Evaluation of photocatalytic activity of $Cu^{II}_{(x)}Fe^{II}_{(1-x)}Fe^{III}_{2}O_4$ NPs for MB degradation 60
4.3.1 Effect of $Cu^{II}_{0.4}Fe^{II}_{0.6}Fe^{III}_{2}O_4$ dosage on MB degradation 63
4.3.2 Effect of H_2O_2 concentration on MB degradation 64

4.3.3 Effect of pH on MB degradation 65

4.3.4 Summarizing the optimized photocatalytic conditions for MB 66

4.3.5 MB degradation mechanism 68

4.4 Evaluation of Photocatalytic Activity of $Cu^{II}_{(x)}Fe^{II}_{(1-x)}Fe^{III}_{2}O_4$ NPs for RhB degradation 71

4.4.1 Effect of catalyst dosage 74

4.4.2 Effect of hydrogen peroxide concentration 75

4.4.3 Effect of pH 77

4.4.4 Summarizing the optimized conditions for RhB degradation 80

4.4.5 Degradation mechanism for RhB 80

4.5 Comparison of the photocatalytic performance of simple metal oxides, doped (NP-3) and metal oxides composite 82

4.6 Reusability of NPs 84

4.7 Antimicrobial results 86

5. New scientific results 88

6. Acknowledgement 91

7. Funding 91

8. References 92

List of Tables

Table 1. Band gap energies (eV vs. NHE) of commonly used ferrites [58] 12

Table 2. Theoretical stoichiometric compositions of the solutions used in the synthesis of oxide and iron(II) doped copper ferrite NPs 33

Table 3. Comparison of theoretical and experimental Cu/Fe ratios of the catalysts prepared 44

Table 4. Specific surface areas (BET) of the catalysts prepared. 58

Table 5. Control experiments for MB degradation. Concentrations: MB = 1.5×10^{-5} mol/L, NP-3 = 22.73 mg/L, H_2O_2 = 1.01×10^{-2} mol/L, temperature = 25±2 °C and irradiation time = 140 min. 60

Table 6. Control experiments for RhB degradation. Concentrations: RhB = 1.75×10^{-5} mol/L, NP-3 = 400 mg/L, H_2O_2 = 1.76×10^{-1} mol/L, pH = 7.5, temperature = 25±2 °C, and irradiation time = 140 min. 72

Table 7. Comparison of reaction rate during RhB degradation at pH around 12 under different experimental conditions 78

List of Figures

Figure 1. Schematic representation of the main photochemical reactions producing reactive oxygen species [25]..... 6
Figure 2. Classification of Advanced Oxidation Processes (AOPs)[37]. 9
Figure 3. Band-gap energy, VB and CB for various semiconductors [55]. 11
Figure 4. Methyl orange chemical structure 19
Figure 5. Design of a suspended (slurry) type photocatalytic reactor [168]..... 26
Figure 6. Solar spectrum representing the proportion of UV, visible and IR radiations [187] 29
Figure 7. Chemical structure of model dyes 31
Figure 8. Flow chart representing the steps of $Cu^{II}O$ NPs synthesis using a simple co-precipitation technique 34
Figure 9. Dark powdered catalysts obtained after calcination process as results of co-precipitation and calcination process 35
Figure 10. Configuration of the photocatalytic reactor fitted directly inside an S600 spectrophotometer (A), schematic representation of the photocatalytic reaction showing the stirring mechanism and visible light irradiation (B). 39
Figure 11. Particle size distribution of $Cu^{II}_{0.4}Fe^{II}_{0.6}Fe^{III}_2O_4$ (NP-3) 45
Figure 12. X-ray diffraction (XRD) diffractograms of iron(II) doped copper ferrites compared to those of the simple oxides of the given metal ions. The characteristic Miller indices indicated for the compounds the standards of which were earlier studied by XRD are taken from the International Centre for Diffraction Data. 47
Figure 13. Comparison of the average crystallite size of simple metal oxides and copper doped ferrites 48
Figure 14. X-ray diffraction (XRD) diffractograms of NP-3, synthesized with increase in the calcination temperature. The characteristic Miller indices indicated of the standard compounds are taken from the International Centre for Diffraction Data. 48
Figure 15. Raman spectra of iron(II) doped copper ferrites compared to those of the simple oxides of the given metal ions. 50
Figure 16. Scanning electron microscopy (SEM) images of synthesized catalysts: (A) $Cu^{II}O$, (B) $Fe^{III}_2O_3$, (C) $Fe^{II}O$ and (D) NP-3 51

Figure 17. Scanning electron microscopy (SEM) images of $Cu^{II}_{(x)}Fe^{II}_{(1-x)}Fe^{III}_2O_4$: (A) x = 0 NP-1, (B) x = 0.2 NP-2, (C) x = 0.4 NP-3, (D) x = 0.6 NP-4, (E) x = 0.8 NP-5, (F) x = 1 NP-6 ferrites. 52
Figure 18. Scanning electron microscopy (SEM) images of NP-3 catalyst synthesized under different calcination temperatures: (A) 150 °C (B) 300 °C (C) 450 °C and (D) 550 °C. 53
Figure 19. EDX spectra (recorded in scan mode) for simple metal oxide NPs (A) $Cu^{II}O$ (B) $Fe^{III}_2O_3$, (C) $Fe^{II}O$ and (D) NP-3..... 54
Figure 20. EDX spectra (recorded in scan mode) of doped ferrites ($Cu^{II}_{(x)}Fe^{II}_{(1-x)}Fe^{III}_2O_4$): (A) x = 0 NP-1 (B) x = 0.4 NP-3 and (C) x = 0.8 NP-5. 55
Figure 21. EDX spectra (recorded in spot mode) of the NP-5 catalyst ($Cu^{II}_{(x)}Fe^{II}_{(1-x)}Fe^{III}_2O_4$, x=0.8), regarding the spot on cubic (A) and needle-like (B) structure. 56
Figure 22. EDX spectra (recorded in scan mode) of doped ferrites NP-3 under different calcination temperatures: (A) 300 °C (B) 450 °C (C) 500 °C and (D) 550 °C..... 57
Figure 23. Kulbelka-Munk function for determination of the band-gap energy (E_{bg}) of NP-3..... 58
Figure 24. Band-gap energies (E_{bg}) of iron (II) doped copper ferrite NPs as the function of Cu^{2+}content for comparison to those of the simple metal oxides. The E_{bg} results of simple metal oxide NPs ($Cu^{II}O$, $Fe^{II}O$, and $Fe^{III}_2O_3$) are also added for comparison. 59
Figure 25. Spectral change during Methylene Blue degradation in photocatalytic system containing NP-3 (x = 0.4). The inset shows the absorbance vs. time plot at 665 nm. Concentrations: MB = 1.5×10^{-5} mol/L, NP-3 = 22.73 mg/L, initial pH = 7.5, H_2O_2 = 1.01×10^{-2} mol/L, temperature = 25±2 °C and irradiation time = 140 min. 61
Figure 26. The logarithm of the absorbance at λ_{max}=665 nm vs. time plot for the degradation of MB (see the inset of Fig. 25). 62
Figure 27. Photocatalytic efficiency in terms of apparent kinetic constant (compared to the control experiment) depending on the Cu^{2+}:Fe^{2+} ratio in $Cu^{II}_{(x)}Fe^{II}_{(1-x)}Fe^{III}_2O_4$. Concentrations were suggested by Singh *et al.* [108]: MB = 1.5×10^{-5} mol/L, NPs = 22.73 mg/L, initial pH = 7.5, H_2O_2 = 1.01×10^{-2} mol/L, temperature = 25±2 °C and irradiation time = 140 min. 62

Figure 28. Effect of NP-3 (x = 0.4) concentration on the reaction rate constant of degradation. Concentrations: MB = 1.5×10^{-5} mol/L, conc. of H_2O_2 = 1.01×10^{-2} mol/L, initial pH = 7.5, temperature = 25±2 °C and irradiation time = 140 min. 64
Figure 29. Effect of H_2O_2 concentration on the reaction rate constant of MB degradation in the absence of NP. Concentrations: MB = 1.5×10^{-5} mol/L, temperature = 25±2 °C and irradiation time = 140 min. 64
Figure 30. Effect of H_2O_2 concentration on the reaction rate constant of MB degradation. Concentrations: NP-3 = 400 mg/L, MB = 1.5×10^{-5} mol/L, initial pH = 7.5, temperature = 25±2 °C and irradiation time = 140 min. 65
Figure 31. Effect of pH on the rate constant of MB degradation. Concentrations: NP-3 = 400 mg/L, conc. of MB = 1.5×10^{-5} mol/L, conc. of H_2O_2 = 1.76×10^{-1} mol/L, temperature = 25±2 °C and irradiation time = 140 min. 66
Figure 32. Relative degradation efficiency (compared to the photodegradation of MB without catalysts (control)) depending on the ratio Cu^{2+}:Fe^{2+} in $Cu^{II}_{(x)}Fe^{II}_{(1-x)}Fe^{III}_2O_4$ at the optimized concentrations: MB = 1.5×10^{-5} mol/L, NPs = 400 mg/L, initial pH = 7.5, H_2O_2 = 1.76×10^{-1} mol/L, temperature = 25±2 °C and irradiation time = 140 min. 67
Figure 33. Effect of the calcination temperature of the NP-3 (x=0.4) catalyst on the apparent kinetic constant of MB degradation. Concentrations: NP-3 = 400 mg/L, MB = 1.5×10^{-5} mol/L, conc. of H_2O_2 = 1.76×10^{-1} mol/L, and irradiation time = 140 min. 68
Figure 34. Schematic diagram for the degradation mechanism of organic pollutants in heterogeneous photo-Fenton system. 69
Figure 35. (A) Methylene blue spectrum, (B) UV/visible spectrum obtained after MB degradation using NP-3 ($Cu^{II}_{0.4}Fe^{II}_{0.6}Fe^{III}_2O_4$), Concentrations: MB = 1.5×10^{-5} mol/L, NPs = 400 mg/L, initial pH = 7.5, H_2O_2 = 1.76×10^{-1} mol/L, temperature = 25±2 °C, and time = 140 min. 70
Figure 36. Visual representation of MB before and after photo-Fenton degradation in the photo-reactor (cuvette). (A) Mixture of MB + NP-3 before photocatalysis, (B) MB + NP-3 after photocatalysis and (C) clear solution obtained after separation of solid catalyst from (B). 70
Figure 37. Measurements of total organic carbon (TOC) during MB photocatalysis at optimized conditions 71

Figure 38. Spectral change during Rhodamine B degradation in photocatalytic system containing NP-3 (x = 0.4). The inset shows the absorbance vs. time plot at λ_{max}=554 nm. Concentrations: RhB = 1.75×10^{-5} mol/L, NP-3 = 400 mg/L, initial pH = 7.5, H_2O_2 = 1.76×10^{-1} mol/L, temperature = 25±2 °C and irradiation time =140 min. 73
Figure 39. The logarithm of the absorbance at λ_{max}=554 nm vs. time plot for the degradation of RhB (see the inset of Fig. 38). 73
Figure 40. Photocatalytic efficiency depending on the ratio Cu^{2+}:Fe^{2+} in $Cu^{II}_{(x)}Fe^{II}_{(1-x)}Fe^{III}_2O_4$. Concentrations: RhB = 1.75×10^{-5} mol/L, NPs = 400 mg/L, initial pH = 7.5, temperature = 25±2 °C, irradiation time = 140 min, and H_2O_2 = 1.76×10^{-1} mol/L 74
Figure 41. Effect of NP-3 ($Cu^{II}_{(0.4)}Fe^{II}_{(0.6)}Fe^{III}_2O_4$) concentration on the RhB degradation. Concentrations: RhB = 1.75×10^{-5} mol/L, conc. of H_2O_2 = 1.76×10^{-1} mol/L, irradiation time = 140 min, temperature = 25±2 °C, and initial pH = 7.5. 75
Figure 42. Effect of H_2O_2 concentration on the RhB degradation in the absence of NPs. Concentrations: RhB = 1.75×10^{-5} mol/L, irradiation time = 140 min, temperature = 25±2 °C, and initial pH = 7.5. 76
Figure 43. Effect of H_2O_2 concentration on the RhB degradation in the presence of NPs. Concentrations: RhB = 1.75×10^{-5} mol/L, NP-3 = 500 mg/L, irradiation time = 140 min, temperature = 25±2 °C, and initial pH = 7.5. 76
Figure 44. Effect of initial pH on the apparent kinetic constant of RhB degradation in the absence of NPs. Concentrations: conc. of RhB = 1.75×10^{-5} mol/L, irradiation time = 140 min, and conc. of H_2O_2 = 8.88×10^{-2} mol/L 79
Figure 45. Effect of pH on the apparent kinetic constant of RhB degradation in the presence of NPs. Concentrations: NP-3 = 500 mg/L, conc. of RhB = 1.75×10^{-5} mol/L, temperature = 25±2 °C, irradiation time = 140 min, and conc. of H_2O_2 = 8.88×10^{-2} mol/L 79
Figure 46. Relative degradation efficiency (compared to the photodegradation of RhB without catalysts (control)), depending on the ratio Cu^{2+}:Fe^{2+} in $Cu^{II}_{(x)}Fe^{II}_{(1-x)}Fe^{III}_2O_4$ at the optimized conditions; concentrations: RhB = 1.75×10^{-5} mol/L, NPs = 500 mg/L, initial pH = 7.5, irradiation time = 140 min, temperature = 25±2 °C, and H_2O_2 = 8.88×10^{-2} mol/L. 80
Figure 47. Rhodamine B degradation reaction proposed pathways, using iron (II) doped copper ferrites under visible light irradiation [217]. 81

Figure 48. (A) Rhodamine B spectrum, (B) UV/visible spectrum obtained after RhB degradation using NP-3 ($Cu^{II}_{0.4}Fe^{II}_{0.6}Fe^{III}_2O_4$), Concentrations: NPs = 500 mg/L, H_2O_2 = 8.88×10^{-2} mol/L, RhB = 1.75×10^{-5} mol/L, initial pH = 7.5, temperature = 25±2 °C, and irradiation time = 140 min. 82
Figure 49. Visual representation of RhB before and after photo-Fenton degradation in the photo-reactor (cuvette). (A) Mixture of RhB + NP-3 before photocatalysis, (B) RhB + NP-3 after photocatalysis and (C) clear solution obtained after separation of solid catalyst from (B). 82
Figure 50. Comparison of apparent kinetic constants of $Fe^{II}O$, $Fe^{III}_2O_3$, $Cu^{II}O$, NP-3 ($Cu^{II}_{0.4}Fe^{II}_{0.6}Fe^{III}_2O_4$), and ($Cu^{II}O/Fe^{II}O/ Fe^{III}_2O_3$) composite. Concentrations: MB = 1.5×10^{-5} mol/L, NPs = 400 mg/L, irradiation time = 140 min, temperature = 25±2 °C, and $H_2O_2 = 1.76\times10^{-1}$ mol/L 83
Figure 51. Comparison of apparent kinetic constants of $Fe^{II}O$, $Fe^{III}_2O_3$, $Cu^{II}O$, NP-3 ($Cu^{II}_{0.4}Fe^{II}_{0.6}Fe^{III}_2O_4$), and ($Cu^{II}O/Fe^{II}O/Fe^{III}_2O_3$) composite in the photodegradation of RhB. Concentrations: RhB = 1.75×10^{-5} mol/L, NPs = 400 mg/L, irradiation time = 140 min, temperature = 25±2 °C, and $H_2O_2 = 1.76\times10^{-1}$ mol/L 84
Figure 52. The effect of the reuse of the NP-3 catalyst on the relative efficiency the MB degradation. Concentrations: NP-3 = 400 mg/L, conc. of MB = 1.5×10^{-5} mol/L, pH = 7.5, time = 140 min, temperature = 25±2 °C, and conc. of $H_2O_2 = 1.76 \times 10^{-1}$ mol/L. 85
Figure 53. The effect of the reuse of ($Cu^{II}O/Fe^{II}O/Fe^{III}_2O_3$) composite catalyst on the relative efficiency the MB degradation. Conc. of composite = 400 mg/L, conc. of MB = 1.5×10^{-5} mol/L, temperature = 25±2 °C, time = 140 min, and conc. of $H_2O_2 = 1.76\times10^{-1}$ mol/L. 85
Figure 54. Comparison of bacterial inhibition percentage of doped copper ferrites against gram negative *Vibrio fischeri* 87
Figure 55. Proposed mechanism for the attachment of nanoparticles to *Vibrio fischeri*. (A) Bacteria and nanoparticles before attachment (B) after attachment 87
Figure 56. Comparison of bacterial inhibition percentage of $Fe^{II}O$, $Fe^{III}_2O_3$, $Cu^{II}O$, and doped NP-3 ($Cu^{II}_{0.4}Fe^{II}_{0.6}Fe^{III}_2O_4$) 88

1. Introduction

Water, a precious resource is vital for the survival of all living organisms. The growing world population demands industrialization which consumes a large amount of water supply, ultimately causing water pollution. This is a major threat to our health and ecosystem and has become a matter of significant concern to society and the economy [1, 2]. Almost all types of water resources are continuously polluted with hazardous compounds across the globe. The increase in pollution and decreased in energy resources are the immediate and vital challenges the world faces in the current era. A report, presented by the United Nations (UN) stated that two-thirds of the world population would face fresh water shortage until 2025 [3]. The pollutants and wastes from human activities are discharged into natural water resources, altering water quality and making it unfit for eco-system, human use, and aquatic life. The major water pollutants are textile dyes, pigments, finishes, pesticides, herbicides, and heavy inorganic metals such as lead, mercury, cadmium, chromium [4, 5]. Additionally, the utilization of new potential pollutants with mutagenic and carcinogenic effects, such as personal care products, endocrine disrupting compounds, and some medically active compounds, could also appear in these water bodies. Most of these pollutants are reported to have harmful effects even at trace amount and compromise human and marine health. The inappropriate disposal of these pollutants in third-world countries is provoked due to the unreliable conventional treatment methods [6].

The integral part of the textile industry effluents in water sources are mainly composed of organic dyes and pigments with an estimated annual production of 450,000 tons globally. Additionally, more than 11% is lost during the dyestuff synthesis, textile dyeing, and finishing processes [7, 8]. A significant portion of these dyes are noxious, mutagenic, and potentially carcinogenic and their removal from the industrial effluents is a significant challenge for environmental researchers [7].

In conventional wastewater treatment processes, the separation of pollutants occurs via mechanical, physical, chemical and biological methods. The larger particles are removed from the water suspension in the primary treatment by filtration and subsequently sent to a secondary treatment facility where the pollutants are removed biologically. The

conventional processes are often not reliable enough for the complete removal of the mentioned pollutants [7]. In general, filtration and adsorption of pollutants from wastewater enhance the water quality to a certain extent but produce post-process wastes, which are pollutant rich, and need further treatments. Additionally, some pollutants found in the effluents of textile industry wastewaters are recalcitrant and non-biodegradable, which demands a tertiary treatment process [8].

United States Environmental Protection Agency (USEPA) has imposed strict regulations to remove these potentially harmful compounds. Thus, researchers have focused on the advanced oxidation processes (AOPs) [9], which have been applied for potential tertiary treatments of the mentioned pollutants in various wastewaters. Within the past few decades, widespread research has been accomplished worldwide as a step in improving these technologies [9, 10]. Incineration or wet oxidation processes are preferred for removing high concentrations of organic substances, e.g., with chemical oxygen demand (COD) of more than 20 g/ml, while for low concentrations of organics, AOPs are highly recommended. In general, AOPs utilize the *in situ* produced highly reactive species (i.e. $^{\bullet}OH$, H_2O_2, O_3, $^{\bullet}O_2^-$) for complete or partial mineralization of stubborn organic compounds [11].

Heterogeneous photocatalysis, a class of AOPs, employing semiconductor catalysts such as, Fe_2O_3, TiO_2, ZnS, ZnO, and CdS, revealed its applicability in degrading hazardous organics compounds into carbon dioxide and water [11]. Titanium dioxide (TiO_2) has delivered a better catalytic performance under the UV range (300 nm < λ < 390 nm) and remains stable for several catalytic cycles. However, the major limitation of TiO_2 is its lower activity under visible-light irradiation due to its higher band-gap energy [11]. Hence, the researchers started to explore heterogeneous catalysts which are cheap, easy to operate, applicable under wide a pH range, consume visible light with better photocatalytic activity, reusable and easily separable. Many metal oxides based on Cu, Fe, Zn, etc., were explored to overcome the limitations posed by TiO_2. Ferrites belong to the class of heterogeneous type catalysts which are active under visible light, cost-efficient, easy to operate under a wide pH range with better photocatalytic performance. Ferrites can be doped with other elements to increase their photocatalytic performance. Several doped, composite-type, and

undoped ferrites were explored for the photocatalytic degradation of organic dyes, pigments, and other pollutants. In addition to photoactivity, several ferrites showed antibacterial activity, too.

Based on these investigations, composite-type and doped ferrites display better photocatalytic activity than undoped ones. This study aimed to investigate the fabrication and elucidation of structural peculiarities of iron(II) doped copper ferrites. Furthermore, the photocatalytic activity was studied using two model pollutants: methylene blue (MB) and rhodamine b (RhB). The key features of these catalysts are; (1) easy and cost-efficient synthesis process, (2) simple reactor configuration, (3) operation at ambient operating temperature and pressure, (4) complete mineralization of organics into safe compounds without producing secondary pollution, (5) reusability, (6) easy separation, and (7) antibacterial/disinfection properties.

2. Literature review

2.1 Nanotechnology

Nanotechnology or nanoscience is considered as one of the vibrant research areas in material science in the current era. For the first time, the word “nanotechnology” was introduced by Japanese scientist Norio Taniguchi at the University of Tokyo, Japan [12, 13]. The word “nano” indicates 10^{-9} m, which is one-billionth of a meter. The properties of nanoparticles (NPs) are based on their size, morphology, distribution, and surface area [14]. During the past decade, at the forefront of science and technologies, the advanced applications of novel NPs are increasing rapidly. Nanotechnology has played a revolutionary role in the industrial field, especially the nanomaterials morphological structures that display significantly unique electronic, chemical, biological, and physical properties. The morphology, size, composition, shape, and crystallinity of NPs determine their intrinsic properties. The narrow size distribution of NPs is their fundamental property, which is needed to achieve a reliable material response [14].

Nanomaterials have extent applicability in catalysis, microelectronics, solar cell, biosensing, diagnostics, drug delivery, cell imaging and labeling, optoelectronics, single-electron transistors, surface-enhanced Raman spectroscopy, nonlinear optical devices, and photonic band-gap materials [15, 16].

2.2 Metal oxide nanoparticles

Metal oxides are considered as materials with large potential in material science, chemistry, and physics [17, 18]. Many metallic elements can form a large variety of oxide compounds [19]. Based on their physico-chemical properties, nano-sized metal oxides offer particular applicability in the industrial sector such as catalysts, ceramics, absorbents, and sensors [20, 21].

Metal oxides are used for both their redox and acid/base properties in the context of absorption and catalysis [22]. The key chemical properties of metal oxides necessary for their utilization as catalysts or absorbents are as follows [19];

(I) oxidation state at surface layers,

(II) coordination environment of surface atoms

(III) redox properties

Oxide NPs with s or p valence electrons in their orbitals tend to be more effective for acid/base catalysis. In contrast, those having d or f valence electrons offer many uses. In specific reaction conditions, a solid redox catalyst undergoes reduction and re-oxidation by releasing surface lattice oxygen anions and captivating oxygen from the gas phase [19].

Generally, optical conductivity is considered one of the major properties of metal oxides which can be determined by absorption and reflectivity measurements [18]. In nanocrystalline semiconductors, both linear and nonlinear optical properties occur due to transitions between electron and hole discrete or quantized electronic levels. However, in light absorption, e.g., the optical band gap and all other electronic transitions existing in the optical absorption spectrum, and the effective mass theory (EMA) forecasts a r^{-2} dependence, with a main r^{-1} correction term in the confinement solid regime. At the same time, free-exciton collision model (FECM) provides an exp(1/*r*) behaviour. Hence metal oxide semiconductors would present a first approximation regarding the inverse squared dependency of optical band-gap energy with the primary particle size. Also, the optical excitations that showed quantum-size confinement effects concern the excitation of optical phonons of oxides. In additions, the optical absorption features of metal oxide NPs are influenced by ‘‘nonstoichiometry’’ size-dependent defect effects [23].

Metal oxides can display ionic (anionic/cationic) or mixed ionic/electronic conductivity, which can be influenced by the solid’s nanostructure. Boltzmann statistics revealed that in a metal oxides the number of electronic charge carriers is a function of the band-gap energy. The major charge carriers are electrons and/or holes. The introduction of non-stoichiometry can help to enhance the number of “free” electron-holes of an oxide [24].

2.3 Advance oxidation processes (AOPs)

AOPs are aqueous phase oxidation methods based on the production of highly reactive species, such as hydroxyl radicals (•OH), during the mechanisms resulting in the degradation of the target pollutant [25] as shown in Equation (1) and Figure 1.

$$Organics + photocatalyst + hv \xrightarrow{HO^{\bullet}} Intermediates \longrightarrow Mineral\ acid \longrightarrow H_2O + CO_2 \quad (1)$$

In general, AOPs based chemical wastewater treatments can yield the complete mineralization of organic pollutants to innocuous products such as water, carbon dioxide and other simple inorganic compounds [26]. The degradation of non-biodegradable organic pollutants can produce biodegradable intermediates, which can be easily removed via secondary biological processes. Main AOPs comprise ultrasound-based electrochemical processes, UV/visible/solar-light-induced photocatalysis, and chemical oxidation utilizing some oxidants (O_3/H_2O_2), producing highly reactive $^{\bullet}OH$ radicals. Moreover, coupled AOPs, such as photo-Fenton, UV/H_2O_2, O_3/H_2O_2 and UV/O_3, have been proven to yield higher removal efficiencies. Chemical oxidants, such as hydrogen peroxide and ozone, have been intensely studied to degrade recalcitrant species in an aqueous medium [25, 26].

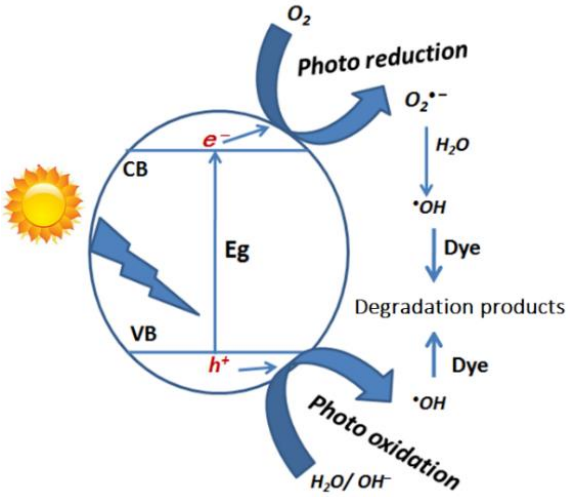

Figure 1. Schematic representation of the main photochemical reactions producing reactive oxygen species [25].

2.3.1 Fenton reaction

It is a catalytic reaction of hydrogen peroxide (H_2O_2) with iron ions (Fe^{2+}) that mainly produces hydroxyl ($^{\bullet}OH$) radicals as the principal oxidizing species (Equation (2)). The basic Fenton type reaction is as follows [27];

$$H_2O_2 + Fe^{2+} \longrightarrow Fe^{3+} + OH^{-} + {}^{\bullet}OH \quad (2)$$

However, the Fenton process initiated by other metals (Fe^{3+}, Cu^{2+}, Co^{2+}) is called Fenton-like reaction (Equation (3))[28].

$$H_2O_2 + Fe^{3+} \longrightarrow Fe^{2+} + HO_2^{\bullet} + H^+ \quad (3)$$

Photo-Fenton is the combination of UV/visible/solar light irradiation with Fenton reagents (hydrogen peroxide and iron ions), which synergistically produce more $^{\bullet}OH$ radicals. Therefore, the oxidation rate of photo-Fenton process is accelerated compared to Fenton process. Hydroxyl radicals (oxidation potential (E_0 = 2.80 V)) are able to degrade several potent compounds in industrial and municipal wastewater [29].

Generally, Fenton system is divided into two main categories, i.e., homogeneous and heterogeneous. In a homogeneous system, the iron species exists in the same phase as the reactants. Several studies explored the potential application of homogeneous photo-Fenton system for the treatment of recalcitrant wastewaters with the major limitation of the formation of large quantity of ferric hydroxide sludge, which is detrimental to our environment. In addition, large amount of catalyst is lost in sludge. However, strict pH requirements in the range of 2.8 – 3.5 are also considered as one of the big challenges for the conventional photo-Fenton system [29, 30].

The heterogeneous photo-Fenton system, where the catalyst (solid) and the reactants (liquid) exist in different phases, has overcomed some of the major limitations of its homogeneous counterpart. Especially, its applicability under wide pH range has gained growing concern in developing novel catalysts. Beside this, no sludge formation, reusability and easy removal of the catalyst from the aqueous medium are some of its advantages. However, slower oxidation rate due to presence of small amount of iron species on the catalyst surface is the major limitation of the heterogeneous system. That's why recent researches in this area are focused on the development of new hetero-catalysts with larger surface area, smaller particle size, and higher photocatalytic efficiencies, being applicable under wide pH range, reusable and easily separable [31].

2.4 Photocatalysis

In general, photocatalysis can be defined as the combined use of UV or visible light and a suitable photoactive catalyst in chemical reactions. Several organic compounds can

be degraded or utterly mineralized at the surface of heterogeneous photocatalysts or oxidized in the solution phase at atmospheric and ambient conditions due to the production of strong oxidation and reduction sites (Figure 1). This phenomenon occurs when the photocatalyst surface is irradiated with light at suitable wavelengths. Radicals are formed in solution, and photo-reaction proceeds, degrading pollutants. Photocatalysis is one of the most important advanced oxidation technologies. In addition to the oxidative treatment of wastewater, it also offers applications in the reductive deposition of metals from wastewater [32, 33].

In chemical reactions, catalysts are defined as compounds, when added to a reaction mixture, decrease the activation energy and, thus, ultimately increase the reaction rate. Generally, a catalyst is not used up or irreversibly changed during the reaction process but reduces the energy needed to approach the reaction transition state. Though, catalysts affect the reaction kinetics, while the equilibrium state remains unaffected [34]. Photocatalysts are divided into two categories; homogeneous catalysts and heterogeneous catalysts (Figure 2). In homogeneous systems, the catalysts exist in the same phase as the reagents do, while in heterogeneous systems, the catalysts' phase is different from that of the reagents [35, 36]. This study is focused on the heterogeneous photo Fenton-system, which is a sub-category of heterogeneous catalysis. Hence, it will be discussed in detail in the subsequent section.

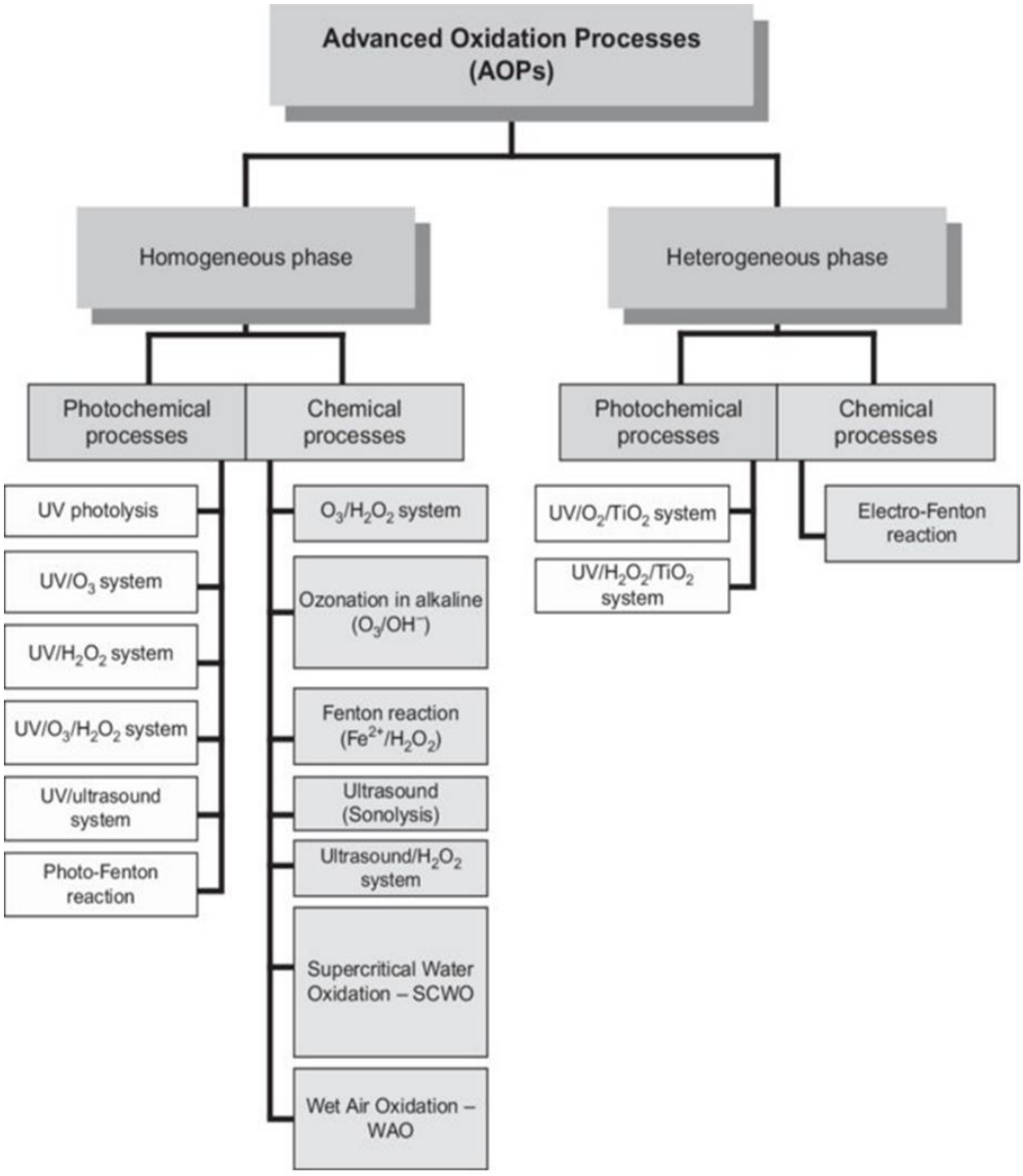

Figure 2. Classification of Advanced Oxidation Processes (AOPs)[37].

2.4.1 Heterogeneous photocatalysis

Heterogeneous photocatalysis can be defined as the acceleration of a photoreaction in the presence of a solid catalyst [38, 39]. In 1972, the discovery of photochemical splitting of water into hydrogen and oxygen in the presence of TiO_2 by Fujishima and Honda attracted researcher's interest in heterogeneous photocatalysis [40]. The recent research on photocatalysis has focused on using semiconductor photocatalysts to eliminate some inorganic and organic species from certain systems (aqueous or gas phase) in drinking water treatment, environmental remediation, and various medical and industrial

applications [41]. TiO_2 can oxidize inorganic and organic substrates in water/air via redox processes. The most prominent properties of TiO_2, for example, long-term photo-stability and chemical stability, have widened its practical applications in many commercial products such as catalysts, drugs, cosmetics, pharmaceuticals, foods, paints, solar cells, and sunscreens [42]. However, in photocatalysis, band gap is considered one of the key factor. TiO_2 belongs to the class of large band-gap semiconductors and usually exists in rutile (3.0 eV) and anatase (3.2 eV) phases. The photoactivity of TiO_2 to UV light has led to its applications in solar fuel production and environmental remediation [43]. Band-gap excitation of TiO_2 results in charge separation leading to the production of electrons in the conduction band (CB) and holes in the valence band (VB).

Surface adsorbed species help in scavenging of electrons and holes. Hence, visible-light-induced photocatalysis can be realized by doping TiO_2 with other short-band-gap semiconductors or sensitizing dyes [44]. Conversely, surface deposited materials' catalyst deactivation or poisoning is another challenge for practical use of TiO_2 in wastewater remediation [45]. TiO_2 revealed a quite low visible-light photocatalytic activity. However, extensive efforts were made to dope TiO_2 with certain ions such as Fe, Au, Ru, Ag, S, C, N, etc. [46].

The activation of the degradation process using pure TiO_2 needs light at wavelengths the corresponding energies above the band gap of the active anatase phase of 3.2 eV, i.e. $\lambda < 387$ nm [47]. Unfortunately, though, the solar spectrum contains only 5-8% UV, which is a considerable limitation. Hence, these catalysts demand artificial illumination to attain degradation of the organic material in water treatment plants [48]. The researchers' primary objective is to develop more stable, efficient catalysts, by which photo-reactions can be initiated and proceeded by utilization of naturally available sunlight. Significant developments have been reported in heterogeneous catalysis driven by visible light. Thus, the addition of dopants, accurate control of the stoichiometry of the mixed metal oxides as catalysts, particle size, shape and pore topology are all critical factors [49].

Due to the intrinsic nature of semiconductor oxides (such as, α-Fe_2O_3, ZrO_2, TiO_2, WO_3, ZnO, SnO_2, MoO_3) and semiconductor sulfides (such as, WS_2, MoS_2, CdS, ZnS, CdSe,), they are applied as potential candidates in catalysis of photo-induced chemical

reactions [50-53]. In general, when a photon having energy higher than the semiconductor bandgap value (E_{bg}), this energy is absorbed, and the electron (e^-) is promoted from the VB into the CB, thus creating a hole (h^+) in VB. These light-induced charged particles contribute to the photocatalytic decomposition processes. The positive charge carrier hole (h^+) facilitates the degradation of organic compounds via generating hydroxyl radicals ($^\bullet OH$), while the negative electrons (e^-) can also promote oxidative degradations via producing superoxide radicals ($^\bullet O_2$). Though, the photo-generated electron-hole pairs can easily recombine [54]. A photocatalyst must be cost-effective, stable in certain conditions, least toxic, and highly photoactive for practical applications.

The band-gap energy and band-edge positions of commonly used oxides, such as ZrO_2, Fe_2O_3, TiO_2, ZnO, SnO_2, and WO_3, are sufficiently good (Figure 3). Therefore, they can be successfully applied in photocatalytic degradation of hazardous compounds due to their inherently filled VB and empty CB [55].

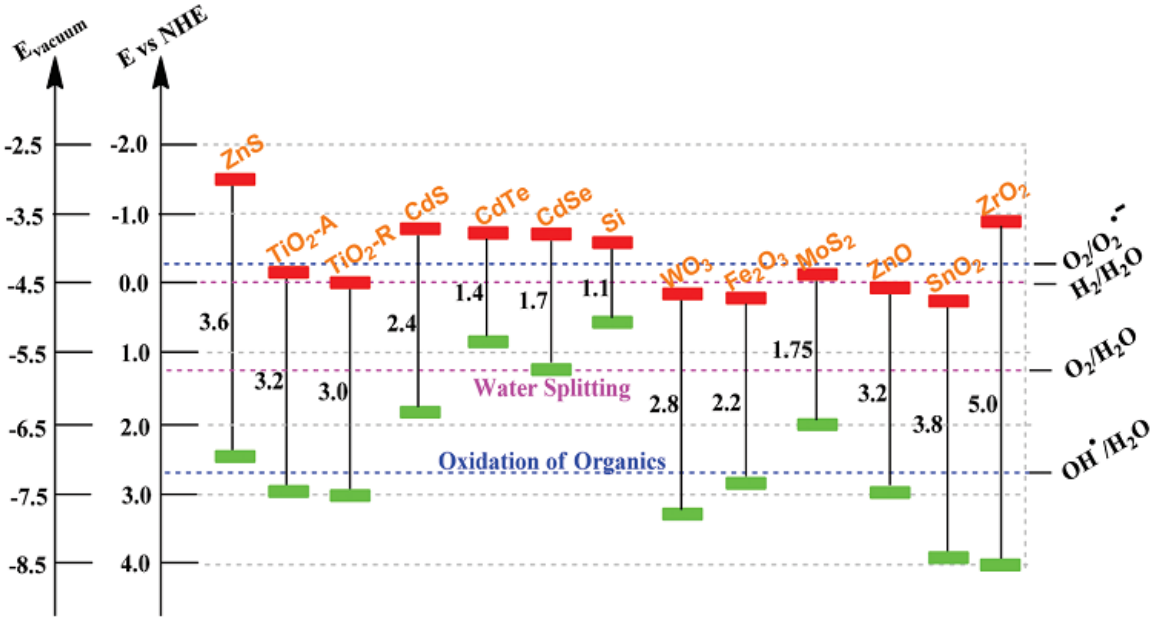

Figure 3. Band-gap energy, VB and CB for various semiconductors [55].

2.5 Ferrites

Ferrites are compounds with the general formula AB_2O_4, where A and B are metal ions, formed as powder or ceramic bodies having iron oxides (Fe_2O_3 and FeO) as their crucial constituent [56]. Maghemite (γ-Fe_2O_3) and magnetite (Fe_3O_4) are of significant

interest among ferrites. Based on crystalline structure, ferrites can be classified into: spinel (MFe_2O_4), hexagonal ($MFe_{12}O_{19}$), and garnet ($M_3Fe_5O_{12}$), where M represents one or more bivalent transition metals (Co, Fe, Zn, Cu, Ni, and Mn). The major advantages of ferrites are an appropriate band gap capable of absorbing visible light and the spinel crystalline structure, which enriched the efficiency by providing extra available catalytic sites [57]. The band-gap energies of some of these commonly used ferrites are shown in Table 1.

Table 1. Band gap energies (eV vs. NHE) of commonly used ferrites [58]

Ferrite	**Band gap (eV)**	**Ferrite**	**Band gap (eV)**
$CaFe_2O_4$	1.90	$ZnFe_2O_4$	1.92
$MgFe_2O_4$	2.18	$NiFe_2O_4$	2.19
$CoFe_2O_4$	1.88	$CuFe_2O_4$	1.32

Ferrites gained much interest in visible-light-induced photocatalytic degradation of contaminants in water and wastewater. The commonly investigated contaminants are specific dyes and pigments, organic and inorganic compounds, and some bacteria. Researchers devoted efforts to developing effective visible-light active photocatalysts, which can utilize the largest portion of the solar spectrum and artificial light energy sources. Metal oxide composite photocatalysts with two or more components have been explored to improve photocatalytic performance compared to the individual ones. After completing of chemical reactions, ferrites, due to their magnetic nature, can be quickly recovered from the reaction mixture [59]. Both undoped and doped transition ferrites are potential candidates in many practical and industrial applications such as catalysis [60], ecological hydrogen production [61], magnetic and electronic devices, treatment of exhaust gases [62], alkylation reactions [63], oxidative dehydrogenation of hydrocarbons [64], alcohols and hydrogen peroxide decomposition [65], crude petroleum hydrodesulphurization [66], oxidation reactions of compounds such as CH_4, H_2, CO [67] and chlorobenzene [68], phenol hydroxylation [69], and catalytic combustion of CH_4 [70].

In literature, cobalt, zinc, copper, nickel, aluminum, and several mixed-metal ferrites were investigated in photocatalytic reactions, principally in specific synthesis processes and degradation of organic compounds. Moreover, ferrites crystallite size, crystal structure, microstructure, photocatalytic and magnetic properties are strongly

influenced by synthesis conditions. Cobalt ferrites are usually synthesized in the range of 2 – 50 nm particle sizes, primarily by the co-precipitation method in the presence or absence of capping agents/surfactants [71]. A recent study reports the successful doping of manganese metal ion into cobalt ferrites at various concentrations for oxidation of toxic orange II dye [72]. Goyal *et al.* [73] improved the catalytic performance of spinel nanoferrites $CoFe_2O_4$ and $NiFe_2O_4$ catalysts via doping of Al into their lattice structure. Moreover, $CoFe_2O_4$ NPs are stable, possess high electron transfer ability and form hetero-junctions by coupling with other semiconductor materials [74].

Nano-sized undoped or doped nickel ferrites are commonly applied in catalytic processes. For example, high reactivity of $NiFe_2O_4$ NPs are well-known, hence, they serve as effective metal-doped ferrite catalysts in several industrial processes, for instance, in water–gas shift reactions [75]. Liang, J. *et al.* [76] developed nickel ferrite and graphene oxide ($NiFe_2O_4$-rGO) composite via ball milling method, which served as a visible-light active photocatalyst and revealed better photocatalytic performance. A study reported by Iftikhar *et al.* [77] also proved that the incorporation of rGO in the $Ni_{0.4}Co_{0.6}Er_{0.045}Fe_{1.95}O_4$/rGO nano-composite system delivered a better catalytic activity. Rahman *et al.* [78] reported the fabrication of $NiCe_{0.05}Fe_{1.95}O_4$/rGO nano-composite photocatalyst, which revealed enormous potential in visible-light induced photocatalytic applications. Khan *et al.* [79] presented a comprehensive report on the synthesis of $NiAl_xFe_{2-x}O_4$ ($0.0 = x \leq 0.5$) NPs and investigated their catalytic activity in visible-light induced degradation of methylene blue.

Pure spinel zinc ferrite ($ZnFe_2O_4$) and its composites are under scientists focus due to their remarkable properties and several practical applications [80]. In general, $ZnFe_2O_4$ are cost effective [81], less toxic, naturally available in abundance, eco-friendly, photochemically stable [82], visible-light active with band-gap energy of 1.9 eV [82], ferromagnetic, and low recombination rate on catalyst surface [83]. Jumeri *et al.* [84] prepared $ZnFe_2O_4$-rGO from $FeSO_4$ and ZnCl as the precursor materials via microwave-assisted hydrothermal method and investigated the catalytic performance of the composite material, using H_2O_2-assisted visible-light induced decomposition of methylene blue in aqueous medium. Recently, Baynosa *et al.* [80] fabricated mesoporous $ZnFe_2O_4$ NPs and

$ZnFe_2O_4$-rGO nanocomposite, using water as solvent, and investigated their activity in solar light induced catalytic degradation of methylene blue.

2.5.1 Copper ferrites

Copper ferrites ($CuFe_2O_4$) are considered one type of the prominent candidates of spinel ferrites due to their phase transitions, semiconducting properties, tetragonality variation, electrical switching, magnetic properties, thermal as well as chemical stabilities. They offer their potential applications in the fields of catalysis, lithium-ion batteries, gas sensing, bioprocessing, magnetic refrigeration, ferrofluids, recording devices, color imaging, and bioprocessing [85-87]. In general, $CuFe_2O_4$ can crystallize in tetragonal or cubic symmetry, depending on the synthesis technique. Naseri *et al.* [88] reported the fabrication, characterization, and magnetic properties of $CuFe_2O_4$ nanoparticles prepared by the thermal treatment method. $CuFe_2O_4$ exhibits several catalytic applications in the conversion of CO to CO_2 [89]. $CuFe_2O_4$ NPs (20 nm) were applied as recyclable heterogeneous initiators in the synthesis of 1,4-dihydropyridines. They reaction of substituted aromatic aldehydes, ethyl acetoacetate and ammonium acetate was attained in ethanol at room temperature, using copper ferrite nano powders. Their major advantages are cost-effectiveness, easy workup, significantly shorter reaction times, no isomerization during the reaction, reusability, and high yields of products [56]. Niyaz *et al.* [90] carried out the photocatalytic ozonation of organic dyes such as Reactive Red 198 (RR198) and Reactive Red 120 (RR120), using $CuFe_2O_4$ NPs synthesized via co-precipitation technique. Goyal *et al.* [91] explored the fabrication of MFe_2O_4 (M = Zn, Cu, Ni) via the sol-gel route and studied their catalytic efficiency for the reduction of nitrophenols in the presence of $NaBH_4$. They achieved better catalytic performance for $CuFe_2O_4$ in comparison to Zn and Ni ferrites. Zaharieva *et al.* [85] published the fabrication and characterization of $CuFe_2O_4$ nano-structures as photocatalysts and investigated their photocatalytic performance in UV-light induced degradation of malachite green dye. Kannaujia *et al.* [92] developed poly(acrylic acid-acrylamide-methacrylate) incorporated $CuFe_2O_4$ nanocomposites and explored their absorption and oxidation properties by using methylene blue.

Doping, immobilization and composite making are under continuous investigation in environmental remediation for the improvement of pollutant removal properties of the

catalysts. These techniques can enhance the adsorption capacity of a catalyst and minimize the recombination rate of the photo-generated electron-hole pairs. Recently, graphitic carbon nitride, graphene, nitrogen-doped carbon nanotubes, and activated carbon were mainly explored by researchers as carbon-based support materials for $CuFe_2O_4$, which served as a favourable catalyst in Fenton-like systems based on its large surface area and capability for electron transfer [93, 94]. Graphene-oxide as well as graphene exhibit large surface area, excellent mechanical strength, and extraordinary electrical conductivity. Hence, they are considered as the potential support materials for catalysts [95]. Several supported copper ferrites such as $CuFe_2O_4$@OMS-2 [96] have been applied to activate peroxymonosulphate to oxidize acid orange 7 dye. Zhao *et al.* [97] explored the visible-light-induced degradation of methyl orange by using $CuFe_2O_4$/AgBr catalyst. Arifin *et al.* [98] reported the fabrication of $CuFe_2O_4/TiO_2$ photocatalyst and studied it in visible-light-induced degradation of methylene blue dye. Recently, Kodasma *et al.* [94] reported the synthesis and characterization of $CuFe_2O_4$-graphene oxide catalysts and investigated its catalytic activity using UV-C induced degradation of Reactive Black 5 (RB5). Our research group synthesized needle-like iron(II) doped copper ferrites [99] and simple metal oxides [100] via co-precipitation technique, and investigated their catalytic activity in the photo-Fenton degradation of Methylene Blue and Rhodamine B. In addition, the efficiencies of homogeneous and heterogeneous photo-Fenton systems were also compared using Rhodamine B.

2.5.2 Mixed metal ferrites

Mixed metal ferrites in size ranging from ultrasmall particles (5–8 nm) up to 100 nm or more are commonly used in catalytic applications. Mixed metal ferrite NPs can be fabricated by various techniques, especially co-precipitation, micro-emulsion, sol-gel and microwave heating are widely explored [101]. Velinov *et al.* [56] reported that $Cu_{1-x}Co_xFe_2O_4$ ($0<x<1$) (8-40 nm) ferrites delivered a better catalytic performance in the oxidation of CH_3OH to CO and H_2 compared to simple $CuFe_2O_4$. Wang *et al.* [102] explored the fabrication of $Co_{1-x}Zn_xFe_2O_4$ ($0<x<1$) NPs (10.5–14.8 nm) via the hydrothermal method and studied their catalytic activity in natural-sunlight induced degradation of methyl blue in aqueous solution. Sathishkumar *et al.* [103] investigated the synthesis of $CoFe_2O_4/TiO_2$ (150 nm), as well as pure cobalt ferrite $CoFe_2O_4$ (50 nm), via

co-precipitation technique and explored their photocatalytic activity in visible-light-induced degradation of reactive red 120 (RR120). Velinov *et al.* [104] developed $Ni_{1-x}Zn_xFe_2O_4$ (x = 0, 0.2, 0.5, 0.8, 1.0) NPs via combination of two techniques such as chemical precipitation and spark plasma sintering (SPS). Several other mixed metal spinel ferrites are also explored in literature such as $Cu_{1-x}Cd_xFe_{1-x}Al_xCr_{1-x}Mn_xO_4$ ($0<x<1$), $Mn_{1-x}Cu_xFe_2O_4$ (x= 0, 0.25, 0.5, 0.75, 1.0), $Co_{1-x}Ni_xFe_2O_4$ (x= 0, 0.2, 0.4, 0.6), and $Ni_{1-y}Zn_yFe_2O_4$ (y= 1, 0.7, 0.5, 0.3) etc. A very recent study was focused on the synthesis of $CoMn_xFe_{2-x}O_4$ (x = 0.0, 0.2, 0.4, 0.6, 0.8 and 1.0) for oxidation of water-soluble orange II dye [72].

2.5.3 Relation between ferrites structure and its catalytic properties

Scientists are in a continuous quest to establish relationships between shape, structure, surface area, and particle size of ferrite NPs. In addition, the nature and the ratio of main metal atoms and doping ones are also crucial in the determination of their catalytic activity. Therefore, the efficiency of ultra-small spinel ferrites (Co, Cu, and Ni) was studied via UV–Vis spectrophotometry on the degradation of H_2O_2 and by oxidation of methylene blue [105]. In the H_2O_2 degradation study, Co^{2+} revealed to be the key factor in achieving better efficiency of the catalyst. However, in the case of methylene blue degradation, Cu ferrites revealed a better catalytic performance. Cubic spinel structure $CoFe_2O_4$ NPs (in size range of 2–6 nm) proved to be active catalysts in the degradation of methylene blue, using H_2O_2 [106]. In another study by Hao *et al.* [107], 3D flower-like $Co_{3-x}Fe_xO_4$ ferrite (specific surface area, 163 m^2/g) hollow spheres proved an effective catalyst for methylene blue oxidation using H_2O_2 as an oxidizing agent. Dom *et al.* [57] reported that the photocatalytic activity of orthorhombic $CaFe_2O_4$, spinel $MgFe_2O_4$ and $ZnFe_2O_4$ ferrites NPs, mainly depends on the crystallinity and surface area of the catalyst. Singh *et al.* [108] synthesized spherical Ni-doped $CoFe_2O_4$ NPs (4–6 nm), and found that the $Co_{0.4}Ni_{0.6}Fe_2O_4$ (having surface area 154.02 m^2/g) delivered the best performance in the reduction of 4-nitrophenol to 4-aminophenol by using a reducing agent ($NaBH_4$). An increase of the Mn^{3+} concentration in Co–Zn cubic spinel structure ferrites ($Co_{0.6}Zn_{0.4}Mn_xFe_{2-x}O_4$, x = 0.2, 0.4, 0.6, 0.8 and 1.0) enhanced the degradation rate of methyl orange [109]. Also, increase of the Cd^{2+} concentration in $Co_{0.6}Zn_{0.4}Cu_{0.2}Cd_xFe_{2-x}O_4$, x = 0.2, 0.4, 0.6 and 0.8) improved the photocatalytic degradation of methyl orange, which may be due to a decrease in the

band-gap energy [110]. In the visible-light-induced degradation of Rhodamine B [111], pure BFO ($BiFeO_3$) NPs showed lower activity than the composite BFO/γ-Fe_2O_3, which may be attributed to the heterojunction structure between BFO and γ-Fe_2O_3. Recently, Lassoued and Li [112] explored the influence of Ni addition to spinel $Ni_xCo_{1-x}Fe_2O_4$ catalysts on the decomposition rate of methylene blue (MB).

2.5.4 Applications of ferrites

Exploration of ferrites is becoming important due to their technical and magnetic properties. They serve as catalysts and adsorbents in biomedical, electronic materials and wastewater treatment. The primary application areas are briefly discussed below.

2.5.4.1 Antibacterial property of ferrites

Besides catalytic potential, ferrites also exhibit applications in biomedicine [113]. Ferrites have delivered an antimicrobial activity in the composite form having silver, such as Ag/$NiFe_2O_4$, Ag/$MgFe_2O_4$, and Ag/$ZnFe_2O_4$ and Ag/$CoFe_2O_4$ [114]. However, the composite of $NiFe_2O_4/TiO_2$ revealed high antimicrobial activity under UV irradiation, which is significantly higher than the application of UV light alone [115]. The production of hydroxyl radical ($^{\bullet}OH$) by ferrites is the key to achieve effectiveness against several bacteria. Li *et al.* [114] compared the antibacterial properties of Ag/$MgFe_2O_4$ with those of an antibiotic (streptomycin). The average inhibition zones of the ferrite photocatalyst are very close to that of the antibiotic (29.3 mm vs. 33.3 mm), which proved that the ferrite composite also has significant antimicrobial activity.

Samavati A. & Ismail A.F. [116] reported the synthesis and antibacterial properties of copper-substituted cobalt ferrite ($Cu_xCo_{1-x}Fe_2O_4$), where x = 0.0, 0.3, 0.5, 0.7 and 1.0) NPs. ZnO particles inhibit both gram-positive and gram-negative bacteria and they are also effective against high-temperature and high-pressure resistant spores [117]. ZnO NPs in small size deliver considerable antibacterial activities, and the activity depends on the concentration and surface area; the larger surface area and higher concentration deliver better antibacterial activity [118]. However, the particle shape and crystalline structure have a little effect on the antibacterial activity [119]. Zhang *et al.* [120] investigated the antibacterial behaviour of suspensions of ZnO NPs against *Escherichia coli* bacterial strain. Several researchers explored the antimicrobial properties of several metals, pure and doped

metal oxides NPs such as Ag [121], Au [122], Al_2O_3 [123], ZnO [124], Fe_3O_4 [125], and α-Fe_2O_3 [126].

2.5.4.2 Removal of inorganic pollutants

The removal of inorganic pollutants, especially As^{3+}, As^{5+}, Cr^{3+}, and Pb^{2+} is essential to safeguard the living organisms from their harmful effects. Some ferrites ($MnFe_2O_4$ and $CoFe_2O_4$) have adsorptive capacities for As^{3+} and As^{5+}, while $MgFe_2O_4$ is effective for the adsorption of SO_2 [127]. Ferrites can be used as photocatalysts and adsorbents, which qualify them as potentially effective in water treatments. $ZnFe_2O_4$ has been studied as a photocatalyst in the photodehydrogenation of H_2S, which produces eco-friendly H_2 and reduces potent greenhouse gas. In addition, $CaFe_2O_4$ is effective in the reduction of CO_2 to form methanol as the major product. Ferrites alone or in composite form have been explored as adsorbents and photocatalysts [58].

2.5.4.3 Removal of organic pollutants

Water resources are greatly polluted with organic pollutants in many industrial and domestic applications. Textile, leather, paper and pharmaceutical industries consume and pollute water in large amounts. Ferrites are also effective in the degradation of certain organic dyes, pigments and other potential organic compounds. For example, $BaFe_2O_4/TiO_2$ and $ZnFe_2O_4$ have been explored in the oxidative degradation of phenol. In addition, acetaldehyde, methanol, styrene, oxalic acid, ethanol, isopropanol, butenes, toluene, and trimethylamine have been effectively degraded using ferrites [58]. Several organic dyes such as methyl orange, methylene blue, rhodamine b, congo red, and reactive red 127 are usually applied to investigate the photocatalytic efficiency of ferrites.

Methyl orange (MO) dye belongs to the group of azo-dyes [115]. Two benzene rings in MO dye (Figure 4) are connected by an azo group and having dimethyl amine and a sulfonic acid group attached to the benzene rings. Ferrites have been explored to degrade MO dye to determine photocatalytic activity in UV- or visible-light-induced irradiation [58].

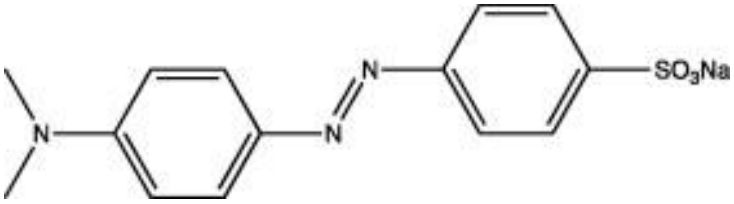

Figure 4. Methyl orange chemical structure

Methylene blue (MB) is another model compound for organic contaminants, used as a redox indicator in chemistry and as a stain in biology. In photocatalysis using ferrites, MB dye undergoes faster degradation. However, the combination of ferrites with other photocatalysts has synergistic effects of photo-reactions. Therefore, many researchers reported application of several ferrites alone or in combinations such as $Ag_3VO_4/CaFe_2O_4$, $TiO_2/CoFe_2O_4$, $ZnO/CaFe_2O_4$, TiO_2/Ni-Cu-Zn ferrite, $MgFe_2O_4$, $CaFe_2O_4$, $ZnFe_2O_4$, $MnFe_2O_4$, $ZnFe_2O_4$/MWCNTs, $ZnFe_2O_4$/MWCNTs + H_2O_2, Fe_3O_4 + H_2O_2, and $Fe_{2.46}Ni_{0.54}O_4$ + H_2O_2 for MB degradation [58]. Recently, Luciano *et al.* [128] investigated the fabrication of manganese ferrite dispersed over graphene sand composite for methylene blue photocatalytic degradation.

Rhodamine B (RhB) is a xanthene dye that has frequently been considered to investigate the degradation potential of ferrites. RhB is potentially toxic and carcinogenic, and therefore has been banned from use in foods and cosmetics but still used in some textile industries in underdeveloped countries [129]. Photocatalysis or adsorption techniques are applied in removing RhB dye, showing high degradation up to 100% in several cases. Ferrites including $ZnFe_2O_4$, $ZnFe_2O_4$/Ag, $CoFe_2O_4$, $TiO_2/ZnFe_2O_4$, $Ag/Fe_3O_4/SiO_2$, $AgI/Fe_3O_4/SiO_2$, $Ag–AgI/Fe_3O_4/SiO_2$, $BaFe_2O_4/SiO_2/TiO_2$ are explored in RhB degradation [58].

2.5.5 Methods for synthesizing ferrites NPs

Several methods for the synthesis of ferrites have been reported in the literature. Few well-known among them are co-precipitation, sol-gel and citrate methods, thermal methods, solid-state reactions, and microemulsion. Each method will be briefly discussed in the coming section.

2.5.5.1 Co-precipitation methods

Co-precipitation is a very facile and convenient way to synthesize iron oxide nanoparticles in a short time with the possibility of large scale production for industrial applications [130, 131]. Generally, co-precipitation and thermal methods for the fabrication of ferrites are similar to some extent. In this method, Fe^{3+} and other metal salts are dissolved in water along with or without a surfactant, under stirring and gentle heating in some cases. The chemical reaction for the synthesis of Fe_3O_4 (Equation (4)) by this technique is as follows [132]:

$$Fe^{2+} + 2\,Fe^{3+} + 8\,HO^{-} \longrightarrow Fe_3O_4 + 4\,H_2O \quad (4)$$

The pH of the reaction mixture is increased to achieve precipitated ferrite NPs. Subsequently, the solid ferrite NPs are filtered and washed with double distilled water and/or ethanol. The purified NPs are dried at 80 –100°C, powdered by using mortar and pestle, and then calcined at various temperatures [127, 133-135].

Singh *et al.* [108] synthesized nickel-doped cobalt ferrite nanoparticles by using microemulsion method leading to the precipitation of corresponding solid metal hydroxides. In this method, two stable microemulsion systems were prepared with identical weight ratios of the four basic constitutive components: sodium dodecyl sulphate, 1-butanol, n-hexane and water (3.03 : 5.57 : 1.64 : 89.82). Metal salts (in stoichiometric amounts), i.e., ferric chloride, nickel chloride, and cobalt chloride, were added to the first microemulsion, and sonicated for 30 min at room temperature. The second microemulsion was composed of 20 mL 5 M NaOH, which served as a precipitating agent. The two microemulsion systems were mixed dropwise and stirred for 60 min in air at room temperature. The as-synthesized solid hydroxide precursor was filtered after washing several times with absolute ethanol. The filtered product was dried in an oven at 110 °C and subsequently annealed at 400 °C for 5 hours.

In this study [99], a similar technique was followed with few modifications. Water was used for making both solutions (I and II) instead of the four basic constitutive components: sodium dodecyl sulphate, 1-butanol, n-hexane and water. The sonication and mixing conditions of both solutions were kept the same as suggested by Singh *et al.* [108]. However, the filtration of the synthesized material was performed by using centrifugation

and a re-dispersion process with absolute ethanol (twice) and water (twice). The purified material was calcined at 400 °C for 4 hours.

2.5.5.2 Thermal methods

Thermal methods of ferrite synthesis are subdivided as solvothermal [136-138], mechanothermal [139], hydrothermal [140], microwave [141] and seed-hydrothermal [142]. In these methods, $Fe(NO_3)_3 \cdot 9H_2O$ or $FeCl_3 \cdot 6H_2O$ salts and metal salt M-SO_4, M-$(NO_3)_2$, or M-Cl_2 are dissolved in water or another solvent under stirring, and the pH is adjusted to 7-12. Then, the mixture is heated in an autoclave for 12–24 h, and subsequently cooled to room temperature. Finally, the solid material is separated from the mixture by centrifugation or filtration, washed with water or ethanol, dried at around 85 °C overnight. However, in the case of mechanothermal methods, the precursor compounds are ground together in a ball-mill, using the same basic method. In the seed-hydrothermal methods, metal oxide (M_2O_3) seeds are used with the Fe^{3+} salt. Both compounds are heated in an autoclave, and the subsequent steps are the same as mentioned above. These thermal methods are convenient but still face some limitations, such as larger particle sizes and impurities in the final products [143].

2.5.5.3 Sol-gel and citrate methods

In sol-gel and citrate methods, the metal and iron precursor materials are added together along with citric acid, and a gel is formed. In general, the precursor materials are dissolved in solvents (water/ethanol) under vigorous stirring at pH ~9 (by the addition of NH_4OH as catalyst) until the formation of a gel-like material [144]. The basic chemistry of the sol-gel process is composed of two steps; hydrolysis (Equations (5) and (6)) and condensation (Equation (7)) [144, 145]. The hydrolysis completes (replacing all OR groups by OH (Equation (5)) or stops, while the metal (M) is partially hydrolyzed ($M(OR)_{4-x}$–$(OH)_x$). Two such molecules may link together via condensation reaction, producing larger metal-containing molecules through the process of polymerization. As a result of polymerization, several hundreds or thousands of monomers make bonds with each other to form a gel-like material.

$$M(OR)_4 + H_2O \longrightarrow HO\text{–}M(OR)_3 + ROH \quad (5)$$

$$M(OR)_4 + 4\,H_2O \longrightarrow M(OH)_4 + 4\,ROH \quad (6)$$

$$M(OR)_3–OH + HO–M(OR)_3 \longrightarrow (OR)_3M–O–M(OR)_3 + H_2O \quad (7)$$

The basis function of citric acid is the assistance in the uniform distribution of the metal ions into mixture. Finally, the gel-like material is dried and then sintered/calcined at variable temperatures and time. To achieve optimum photocatalytic activity, the sintering time and/or temperature is varied [146-149]. The major drawbacks of the sol-gel method are high precursor costs, environmental problems (due to organic by-products), complexity in terms of phase control, and time consuming processes (gelation, drying and heating) [150].

2.5.5.4 Solid-state reaction methods

In solid-state reaction methods, the powder metal and iron salts are heat treated to achieve the desired product [151]. For example, to prepare $CaFe_2O_4$ NPs, iron oxide (Fe_2O_3) and metal salt ($CaCO_3$) powders are evenly mixed and subsequently heated to 1100 °C for 2 h. The synthesis of calcium ferrites takes place through the following reactions (Equations (8) and (9)) [58]:

$$CaCO_3 \longrightarrow CaO + CO_2 \quad (8)$$

$$CaO + Fe_2O_3 \longrightarrow CaFe_2O_4 \quad (9)$$

The solid-state reaction methods for the synthesis of nanoparticles are a novel approach, which owns several pros including simplicity, cost-effectiveness, low contamination, no solvent consumption, high productivity, and selectivity. The major limitations of this technique are large particle size, high temperature requirements, and the production of fine powder needs milling process, which causes contamination. In the synthesis of Ni–Zn ferrite, the volatilization of zinc at high temperatures results in the formation of Fe^{2+} ions [150]. To date, metal oxide and ferrites NPs have been fabricated via this technique. Ceylan *et al.* [152] reported the synthesis of $NiFe_2O_4$ NPs with core/shell structures via a solid-state reaction method. Recently, using this technique, Huang *et al.* [153] also synthesized magnesium and titanium co-substituted M-type barium calcium hexaferrites $Ba_{0.5}Ca_{0.5}Fe_{12-2x}Mg_xTi_xO_{19}$ ($0.0 \leq x \leq 0.5$).

2.5.5.5 Microemulsion methods

The microemulsion method involves the occurrence of co-precipitation in the form of tiny water droplets surrounded by surfactant species which are distributed in organic phase. The surfactant was selected on the basis of the natures of the organic or water phase. The pools of water act as micro-reactors for the synthesis of particles. In addition, the particle size of the final product is controlled by the pool size. The major advantages of the microemulsion technique are control over particle surface morphology, designing the structure, properties and application of the final products, one-step synthesis and stabilization of the particles, low degree of particle agglomeration [154]. Beside these advantages, there are several limitations of this method, such as large amount solvent consumption and also difficulties in scaling up the process [150]. Das *et al.* [154] synthesized pure nanosized $BiFeO_3$ powders by sonochemical and microemulsion methods. Abraime *et al.* [155] reported the development of cobalt ferrite nanopowders by using four techniques such as co-precipitation, sol-gel, sol-gel autocombustion and microemulsion.

After investigating most of the techniques for ferrites synthesis, co-precipitation method was used in this research. This method is facile and more convenient for large-scale production in industrial applications.

2.6 Photocatalytic reactors

Designing an effective photocatalytic reactor is the most challenging task in photocatalysis. The first step is the activation of the semiconductor material to initiate the reaction, which mainly depends on the radiation power of the energy source. A well illuminated reactor is the one with uniform distribution of light, good flow channeling to reduce the dead volume and high mixing. In this study, a photocatalytic reactor (laboratory scale) was designed, where the catalyst was in the suspended form, which provides higher photocatalytic activity. However, designing a reactor for large-scale industrial applications is a difficult task. The type of semiconductor catalyst, geometry of the reactor, energy source and the operating conditions are key points to design a photocatalytic reactor [156-158].

2.6.1 Structure of photocatalytic reactors in water remediation

A photocatalytic reactor designed for water treatment applications must have the following features [159]:

- Provide the possibility to use appropriate UV/Vis or solar radiation as energy source to excite the photocatalyst applied.
- The light source can be distributed evenly inside the reactor or applied externally to the system [160].
- The semiconductor catalyst can be either in suspended or immobilized form [161].
- Provide good flow channeling to minimize the dead volume.
- Deliver high mixing in order to minimize mass transfer resistance of pollutant to reach the activated catalyst surface.

2.6.2 Suspended and immobilized photocatalytic systems

A suspended photocatalytic reactor is the one where a catalyst is in the suspended form in the system, which provides larger photocatalytic activity, while in the immobilized reactor the catalyst is stationary.

In literature, several reactors patented are suspended (slurry) reactors type and classical annular form [158]. Hence, majority of the kinetic studies are focused on the experimental data generated in suspended type photoreactors. The major pros of suspended type photoreactors are uniform catalyst distribution with low pressure drop, a high photocatalytic surface area to reactor volume and low mass transfer limitation. Though, the need for post process treatment (i.e. the removal of solid catalyst from the solution) and assessing of the light scattering in the suspended medium are the crucial drawbacks of such a system [159].

In the immobilized photocatalytic systems, the overall performance of a photo-reactor is reduced due the mass transfer limitations and less catalyst irradiated area. Nevertheless, the major pros of the system are, provision of a continuous process, eliminating the need for catalyst separation and post treatment. Some suitable support materials such as fiberglass sheets can significantly improve mass transfer limitation of the system due to its higher surface area. Glass fibers are used to prepare fiberglass sheets. In

general, glass fiber is formed from melts and manufactured in various compositions by changing the amount of raw materials like sand for silica, clay for alumina, calcite for calcium oxide, and colemanite for boron oxide. The glass fibers can be molded into different kind of fiberglass plates, sheets, and strands [161].

Recently, the researchers explored the efficiency of reactors utilizing solar radiation as energy source. Still, majority of photocatalytic reactors systems using solar irradiations are suspended (slurry) type [162].

2.6.3 Key operational parameters of a suspended photocatalytic reactor

The degradation rates of the organic contaminants and the overall efficiency of the photocatalytic system highly depend upon several key operational parameters, which rule the kinetics of light induced mineralization and disinfection. This section will briefly discuss these operational parameters.

2.6.3.1 Catalyst dosage

In a true heterogeneous catalytic regime, the catalyst concentration in the photocatalytic wastewater treatment system greatly affects the overall efficiency of the photocatalytic process, where the amount of catalyst is directly proportional to the overall photocatalytic reaction rate [163]. However, this linear dependency is true until certain limit, beyond which the reaction rate starts to become independent of the catalyst concentration. Above the saturation level, the increase in the catalyst concentration leads to a high turbidity state, decreasing the absorption coefficient of light photon [164, 165]. Turbidity is the optical characteristic of water and is a measurement of the amount of light that is scattered by colloidal or particulate materials in the water; the higher the intensity of scattered light, the higher the turbidity. Most of the related research works reported the catalyst dosage in the range of 0.1 to 1.0 g/L [166, 167]. The excess catalyst particles can act as light screens, thus reduce the surface area of particles exposed to light and finally the photocatalytic performance is significantly decreased. Hence, a photoreactor should be operated below the saturation level of photocatalyst to ensure efficient absorption of the photons which induce the photocatalytic reactions [48].

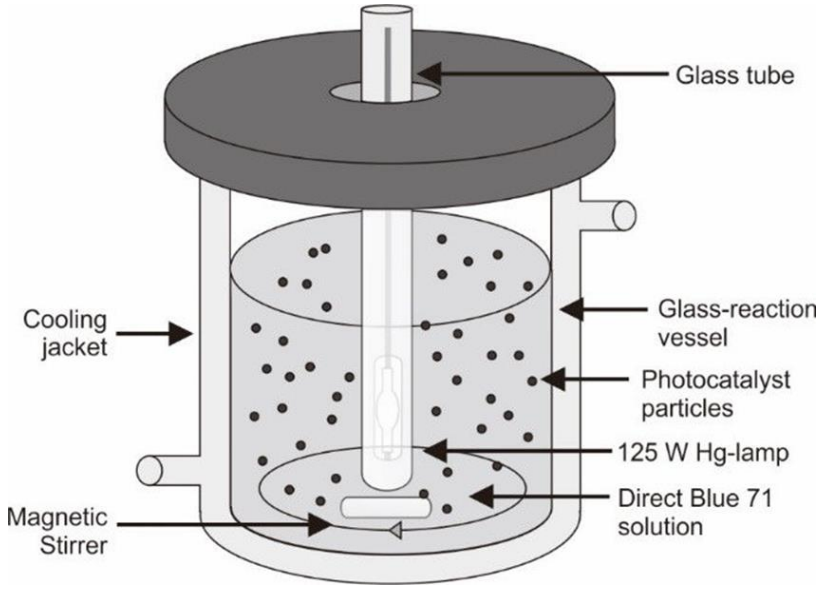

Figure 5. Design of a suspended (slurry) type photocatalytic reactor [168]

2.6.3.2 Temperature

Literature reported several studies focused on the relationship between the efficiency of a photocatalytic reaction and the reaction temperature [169, 170]. Some studies reported that an increase in reaction temperature (>80 °C) during photocatalysis promoted the recombination of charge carriers and also disfavored, the adsorption of organics onto the catalyst surface [163]. The dissolved oxygen in a reaction mixture is highly affected by the temperature. An increase in the temperature decreases the dissolved oxygen, and ultimately inhibits the photocatalytic activity (by reducing the number of reactive oxygen species) [163]. Malato *et al.* [171] reported that the optimum reaction temperature for photo-mineralization should be in the range of 20–80 °C.

2.6.3.3 pH

The interpretation of pH effects on the efficiency of the dye photodegradation process is a very difficult task [172]. The charge on the catalyst surface, the degree of aggregation in the dye and the positions of the conduction and valence bands are highly influenced by the pH. In the case of TiO_2, a change in the operating pH alter the surface charge of the catalyst [48, 173]. The better adsorption capacity of ferrite NPs for both anions and cations makes them an important candidate in the fabrication of photocatalytic materials. When the pH of the solution is below their (ferrites) pH of point zero charge

(pH_{pzc}), they are positively charged and adsorb anions. However, when the solution pH > pH_{pzc}, the catalyst is negatively charged and favors cation adsorption. Some well-known ferrites, such as nickel ferrite, cobalt ferrite, copper ferrite, and manganese ferrite, revealed pH_{pzc} of 7.7, 6.6, 6.7 and 6.8, respectively [174]. It was reported that bismuth ferrite $BiFeO_3$ (BFO) had a strong photocatalytic activity for methylene blue at alkaline pH 11 to 12, while in acidic medium the activity was negligible [175]. On the other hand, Soltani and Entizari [176] reported the photocatalytic degradation of RhB by using bismuth ferrite nanoparticles and revealed that the surface charge of catalyst changes with pH alterations. If the solution pH > pH_{pzc} (pH_{pzc} = 7) of bismuth ferrite, the excess hydroxyl groups (OH^-) compete with COO^- of the RhB dye in binding with $-N^+$ group. This phenomenon decreases the aggregation of RhB molecules. At basic conditions, the solid catalyst is negatively charged and repels the negatively charged COO^- groups on the dye. Hence, a decreasing trend in the photocatalytic activity was observed. Similar effect of pH on the photo-Fenton degradation of RhB was observed in our study. But we witnessed an abrupt increase in the photocatalytic activity at pH > 11 due to the potential deprotonation of hydrogen peroxide (pKa = 11.75). On the other hand, pH effects can also be related to the dye specifications. The protonation or deprotonation of the dye can change its adsorption characteristics and redox activity [177]. Thus, in the photocatalytic wastewater treatment process, appropriate pH control schemes in a wide pH range should be implemented, which effectively promotes the photocatalytic reaction.

2.6.3.4 Dissolved oxygen (DO)

The formation of reactive oxygen species (ROS), the stabilization of radical intermediates, and their mineralization are some roles attributed to dissolved oxygen. Shirayama *et al.* [178] reported the negative effect of DO on the photocatalysis reaction and they found a higher degradation rate of chlorinated hydrocarbons in the absence of DO. Also, in the photocatalytic system, the dissolved oxygen did not significantly affect the adsorption on the surface of catalyst but played a key role in the photocatalytic reaction to assure enough electron scavengers present to trap the excited conduction-band electron from recombination [173]. Wang and Hong (2000) [179] established that the presence of DO could also help to induce the cleavage mechanism for aromatic rings in organic pollutants. Thus, DO plays a very important role in certain photocatalytic systems.

2.6.3.5 Concentration of contaminants

The photocatalytic reaction rate directly depends on the concentration of water contaminant present in the reactor [180]. Under similar circumstances, an increase in the initial concentration of the contaminants demands longer irradiation time needed to reach complete mineralization or disinfection. Saquib and Muneer [181] reported that extremely high concentration of organic contaminants could saturate the surface of TiO_2 catalyst and decreased the photonic efficiency finally resulted in photocatalyst deactivation. Higher concentration of contaminants in the medium decreases the number of available active sites on the catalyst surface, which is highly covered by contaminant ions. Niyaz [182] reported that an increase in initial dye (Reactive Red 198 and Reactive Red 120) concentration in the range of 100 – 250 mg/L inhibited the degradation process using manganese ferrite and zinc ferrite [183]. This phenomenon may be attributed to the formation of intermediates during the photodegradation, which interferes with the parental contaminant molecules. A recent study focused on the application of aluminum doped cobalt ferrites [184] revealed a decrease in MB degradation percentage as a consequence of increase in dye concentration.

2.6.3.6 Wavelength of energy source and its intensity

The potential photochemical effects of the wavelength of energy sources can influence the photocatalytic reaction rate, depending on the photocatalysts type, band-gap energy, crystalline phase and state of doping. Several photocatalysts that are usually used have wide band gaps (>3.1 eV) and utilize a small portion of solar light. The amount of solar energy that reaches the Earth's surface as ultraviolet (UV), visible, and infrared (IR) irradiation are 5%, 46%, and 49%,respectively (Figure 6) [185]. Due to the wide band gap of TiO_2 (3.03 eV in rutile and 3.18 eV in anatase phase), it can absorb only a small portion of solar spectrum [186]. However, doping of TiO_2 reduces the band-gap energy, which helps effectively absorb visible light. Unlike TiO_2, ferrites can effectively utilize visible light due to their lower band-gap energies. Beside wavelength, the light intensity is also very crucial to proceed an efficient photocatalytic reaction. In general, high intensity light is required for getting higher-rate reactions [48]. This effect was confirmed by using visible light bulbs (100 and 200 W) in the photocatalytic degradation of MB, using aluminum doped cobalt ferrites [184]. Several studies reported an enhancement of the rate of degradation of dyes as the light intensity was increased.

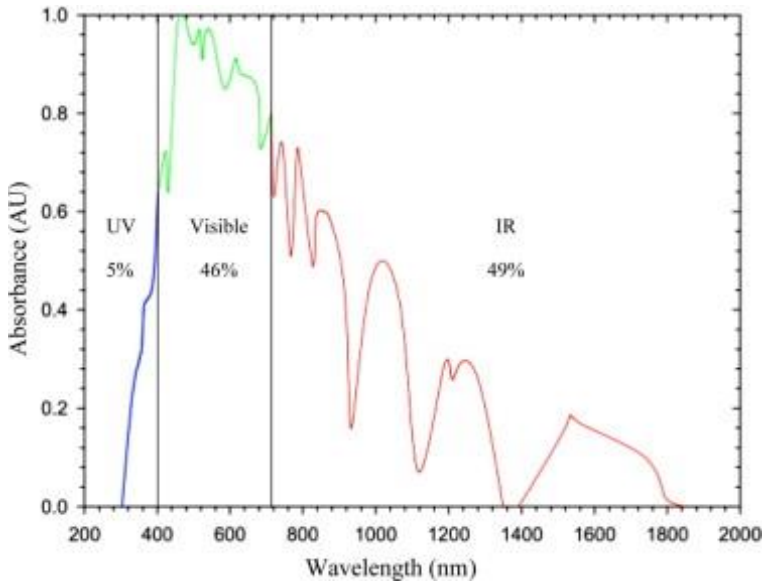

Figure 6. Solar spectrum representing the proportion of UV, visible and IR radiations [187]

2.7 Research objective

Literature reported over 10,000 dye species commercially available for textile, food, and leather industries. Wastes from these industries contain extremely colored species, which are toxic to humans and marine ecosystems. Methylene blue (methylthioninium chloride), a cationic dye in nature, first synthesized in 1876 for its application in clinical medicine. Furthermore, it exhibits numerous uses in the field of textile dyeing/printing, biology and chemistry; and a long-term contact can cause hypertension, vomiting, nausea and anemia [188]. Albert *et al.* [189] reported potential life-threatening toxicity of methylene blue in premature infants. There are hundreds of other organic hazardous compounds, such as congo red, rhodamine b, and several azo dyes, which are used in various textile industries. The removal of these organic compounds is crucial for the safety of living organisms.

In the Research Group of Environmental and Inorganic Photochemistry, at the University of Pannonia, several methods, such as doping, composite making, and immobilization, were explored to enhance the photocatalytic activity of various semiconductor photocatalysts. During my research work, I aimed to develop iron(II) doped copper ferrites as novel heterogeneous photocatalysts by using simple precipitation and calcination technique, to examine their structural and morphological properties, and to investigate their applicability in a lab scale photocatalytic reactor for the treatment of

recalcitrant organic compounds in a heterogeneous photo-Fenton system. Methylene blue (MB) and Rhodamine B (RhB) were applied as model organic compounds (Figure 7).

The effect of change in the composition of $Cu^{II}_{(x)}Fe^{II}_{(1-x)}Fe^{III}_2O_4$ (where x = 0.0, 0.2, 0.4, 0.6, 0.8, and 1.0) on the structural, morphological, optical, photocatalytic, and antibacterial properties were established. For the purpose of comparison of structural and photocatalytic results, simple metal oxides ($Fe^{II}O$, $Fe^{III}_2O_3$, $Cu^{II}O$) of the individual metal salts ($Fe^{2+,}$ Fe^{3+} and Cu^{2+}) were also prepared using similar experimental conditions.

The theoretical and experimental composition of catalysts were studied and compared. Also, the potential leaching of metal ions from the catalyst surface to the aqueous medium were studied by ICP measurements and spectrophotometry. The particle size, surface morphology, specific surface area, and band-gap energy of the catalysts were determined by DLS, SEM, BET, and DRS measurements, respectively. XRD, Raman, EDS, and ICP techniques were also applied in the characterization of the synthesized catalysts.

Preliminary photocatalytic experiments were performed and the individual effects of visible light, the oxidant, and the catalyst in the system were determined. The potential adsorption of dyes on the catalyst surface were also investigated. The reaction conditions, such as catalyst dosage, oxidant concentration, and pH, were optimized using both model dyes. The reaction kinetic models were determined during the degradation processes. The degradation efficiencies of doped copper ferrites and simple metal oxides were compared. In addition, the photocatalytic performances of these metal oxides were checked in composite form ($Cu^{II}O/Fe^{II}O/Fe^{III}_2O_3$), too.

The reusabilities of doped ferrites and simple metal oxide composite were also explored during five experimental cycles. The stability of the catalysts in the aqueous medium was investigated by ICP measurements.

Finally, the antibacterial properties of the metal oxides and doped ferrites were checked against gram negative bacteria *Vibrio fischeri* in the bioluminescence inhibition assay.

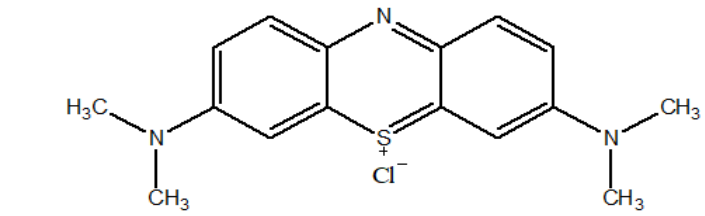

Methylene blue

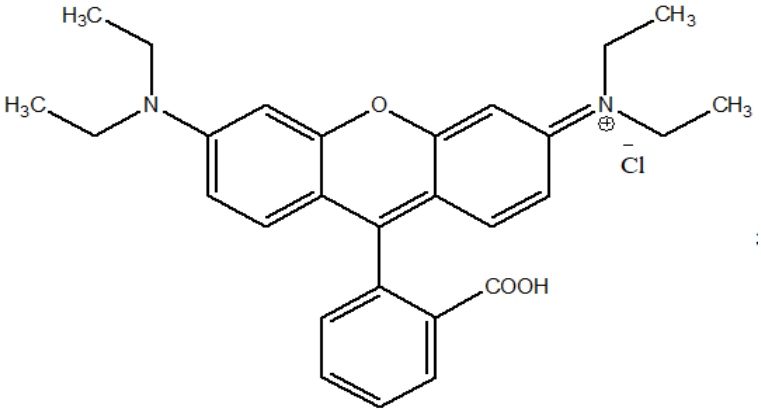

Rhodamine B

Figure 7. Chemical structure of model dyes

3. Materials and Methods

3.1 Materials

The major precursor materials used for synthesis of ferrite NPs were metal salts such as, ferric chloride hexahydrate (98%), ammonium iron(II) sulfate hexahydrate (>95%), and anhydrous copper(II) sulfate (>95%). Sodium hydroxide (99%) was used as precipitating agent during the synthesis of NPs. The NPs were purified by using ethanol (absolute, 99.8%) and double distilled water. The model organic compounds applied for the evaluation of photocatalytic efficiency of NPs were methlyene blue (>95%) and rhodamine b (>95%). Hydrogen peroxide (30% w/w) was added as a Fenton reagent to the heterogeneous photocatalytic system. Sodium hydroxide (99%) or hydrochloric acid (>95%) were used for the adjustment of pH during photocatalysis. All reagents were obtained from Sigma-Aldrich (Budapest, Hungary) and used without further purification.

3.2 Fabrication of simple metal oxide and ferrite NPs

First of all, simple metal oxide NPs were prepared in the composition shown in Table 2. Then iron(II)-doped copper ferrite $Cu^{II}_{(x)}Fe^{II}_{(1-x)}Fe^{III}_2O_4$ NPs (where x = 0.0, 0.2, 0.4, 0.6, 0.8, 1.0) were synthesized. A simple co-precipitation technique (Figure 8) was applied for the fabrication of NPs as recommended by Singh *et al.* [108]. In this technique, solution I was prepared by adding precursor metal salts ($Fe(NH_4)_2(SO_4)_2{\cdot}6H_2O$, $FeCl_3{\cdot}6H_2O$, and $CuSO_4$)) in the composition given in Table 2 to 20 mL distilled water and sonicated for 30 min at room temperature. 5 M NaOH was applied as solution II (20 mL). Both solutions (I and II) were mixed together dropwise under continuous stirring for 60 min. The theoretical stoichiometric compositions of all the catalysts fabricated are indicated in Table 2.

After the formation of dark precipitates, the mixture was centrifuged to separate the precipitates. Next, the obtained precipitates were purified by using absolute ethanol (twice) and double distilled water (twice). Centrifugal filtration method was applied for the purification of precipitates, which is principally a centrifugation (at 5500 rpm for 10 min under ambient conditions) and re-dispersion process (for 3 min). The purified solid hydroxides, as precursors, were dried in an oven at 110 °C for 60 min, and powdered by using mortar and pestle. The dried powdered form of NPs were calcined at 400 °C for 4 h.

The calcined form of NPs (Figure 9) were studied for structural elucidation and photocatalytic applications in heterogeneous photo-Fenton systems. All doped copper ferrites and simple metal oxides were also prepared in similar ways (Figure 8).

The synthesis process of metal oxides and doped ferrites can be explained as follows:

In the first step, hydroxides, such as $Cu(OH)_2$ (Equation (10)), $Fe(OH)_3$ (Equation (12)), and $Fe(OH)_2$ (Equation (14)), are formed and precipitated, which are subsequently heated to form $Cu^{II}O$ (Equation (11)), $Fe^{III}{}_2O_3$ (Equation (13)), and $Fe^{II}O$ (Equation (15)). After drying and calcination, the final oxides are formed. Similarly, iron(II)-doped copper ferrites in the series were prepared by the systematic alteration of $Cu^{II}O$ and $Fe^{II}O$ as shown in Equation (16).

$$CuSO_4 + 2\ NaOH \leftrightarrow Cu(OH)_2 + Na_2SO_4 \quad (10)$$

$$Cu(OH)_2 \leftrightarrow Cu^{II}O + H_2O\uparrow \quad (11)$$

$$FeCl_3 + 3\ NaOH \leftrightarrow Fe(OH)_3 + 3\ NaCl \quad (12)$$

$$Fe(OH)_3 \leftrightarrow Fe^{III}{}_2O_3 + 3\ H_2O\uparrow \quad (13)$$

$$Fe^{II}(NH_4)_2(SO_4)_2 + 4\ NaOH \leftrightarrow Fe(OH)_2 + 2\ NH_4OH + 2\ Na_2SO_4 \quad (14)$$

$$Fe(OH)_2 \leftrightarrow Fe^{II}O + H_2O\uparrow \quad (15)$$

$$Cu^{II}{}_{(x)}Fe^{II}{}_{(1-x)}Fe^{III}{}_2O_4 = xCu^{II}O.(1-x)Fe^{II}O.1Fe^{III}{}_2O_3 \quad (16)$$

Table 2. Theoretical stoichiometric compositions of the solutions used in the synthesis of oxide and iron(II) doped copper ferrite NPs

Type of NPs	**Solution I**			**Solution II**
	$CuSO_4$ (g)	**$Fe(NH_4)_2(SO_4)_2.6H_2O$ (g)**	**$FeCl_3.6H_2O$ (g)**	
$Cu^{II}O$	0.798	-	-	
$Fe^{II}O$	-	1.961	-	
$Fe^{III}{}_2O_3$	-	-	2.703	
NP-1	-	1.961	2.703	

NP-2	0.160	1.569	2.703	5M NaOH
NP-3	0.319	1.176	2.703	
NP-4	0.479	0.784	2.703	
NP-5	0.479	0.392	2.703	
NP-6	0.798	-	2.703	

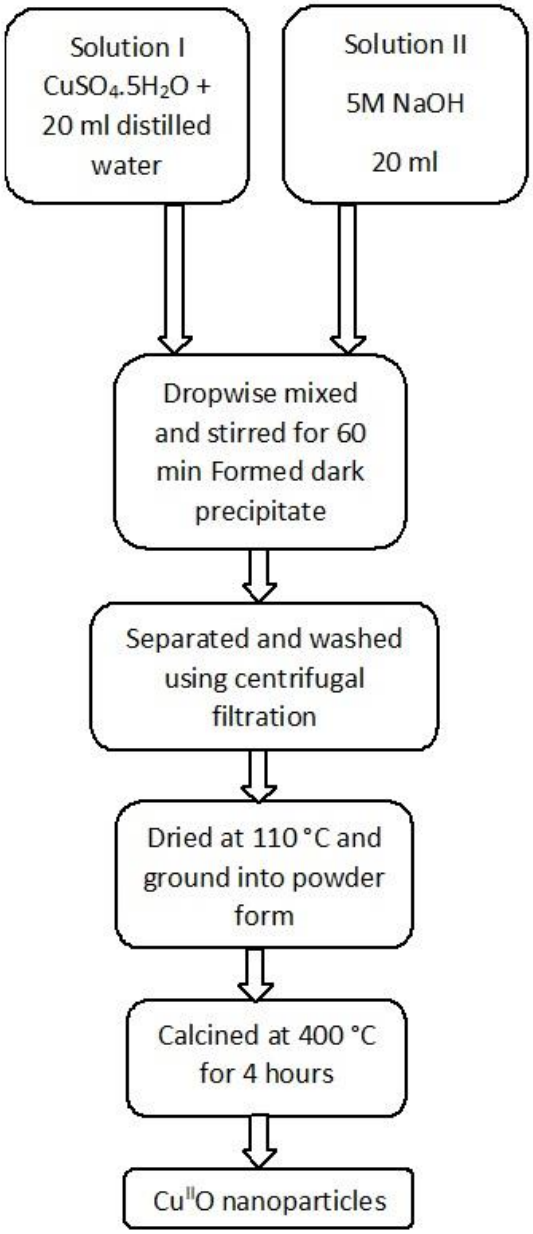

Figure 8. Flow chart representing the steps of $Cu^{II}O$ NPs synthesis using a simple co-precipitation technique

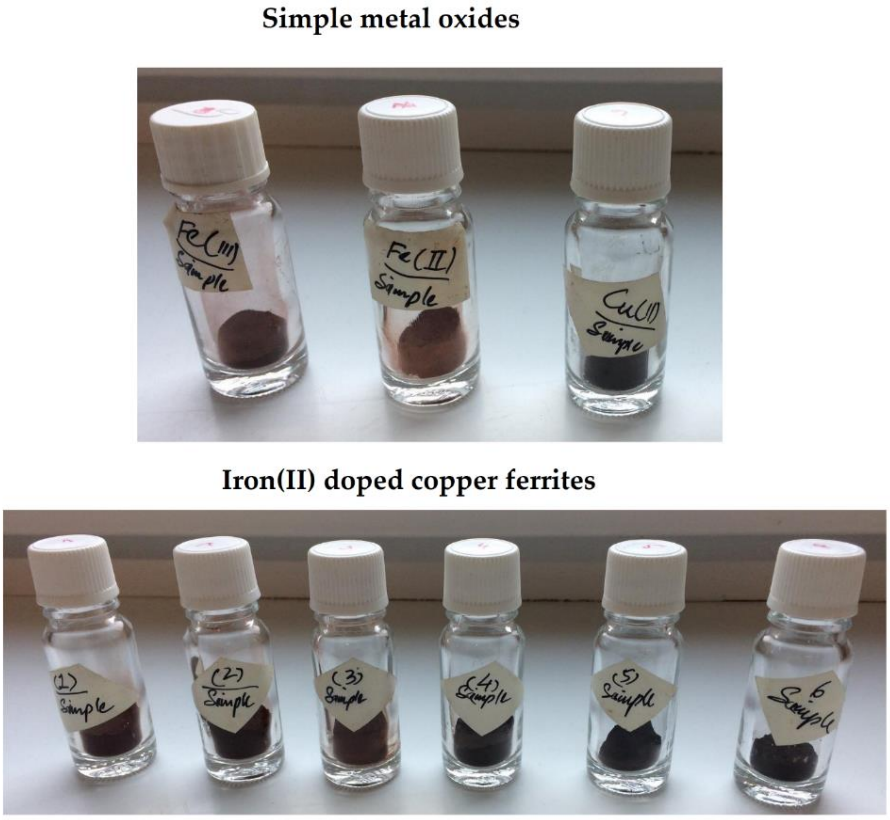

Figure 9. Dark powdered catalysts obtained after calcination process as results of co-precipitation and calcination process

Calcination temperature plays a key role in the surface morphology and catalytic properties of the catalysts. In order to reveal the effect of calcination temperature, we have synthesized NP-3 at different calcination temperatures (150, 200, 250, 300, 350, 400, 450, 500, 550 °C).

3.3 Experimental composition of NPs

The calcined forms of NPs from the series of doped copper ferrites were checked to confirm the complete precipitation of metal ions during the synthesis. The total amounts of the metal ions weighed in were successfully precipitated in NaOH excess during the synthesis process. The above claim was confirmed by the very low values of the solubility product constants (K_{sp}) regarding the corresponding hydroxides [190]:

$Fe(OH)_2$ 8.00×10^{-16} M^3

$Fe(OH)_3$ 2.79×10^{-39} M^4

$Cu(OH)_2$ $2.20x10^{-20}$ M^3

On the basis of these K_{sp} values, the theoretical concentrations in the solution phase were,

$Fe(OH)_2$ $3.20x10^{-17}$ M

$Fe(OH)_3$ $2.23x10^{-41}$ M

$Cu(OH)_2$ $8.80x10^{-22}$ M

Besides, no formation of hydroxo complexes occur in these systems.

3.4 Characterization of NPs

3.4.1 Inductively coupled plasma (ICP) measurements

A Perkin Elmer Optima 2000 DV equipment (Perkin Elmer Inc., Waltham, MA, USA) was applied to determine the experimental Cu/Fe ratios of the prepared catalysts (after calcination). Inductively coupled optical emission spectrometry (ICP-OES) were used to analyze the concentration of metal ions in the samples. The standard solutions (1 g/L) were prepared for each metal according to Merck standard solutions, and diluted soon before use. The solid catalysts were dissolved in a 10-mL flask containing the mixture of conc. HCl (1.72 mL) and conc. HNO_3 (0.46 mL). Then double distilled water was added to get a total 10-mL solution in the flask. Calibration curves were constructed using the linear regression method. Copper (Cu) and iron (Fe) were monitored at the wavelengths 327.393 and 238.204 nm, respectively.

3.4.2 X-ray diffraction (XRD) measurements

A Philips PW 3710 type powder diffractometer (Philips Analytical B.V., Almelo, Netherlands) with a graphite diffracted-beam monochromator and CuK_α radiation (λ = 0.1541 nm) generated at 50 kV and 40 mA was used to measure the X-ray diffraction (XRD) patterns of the simple metal oxide and $Cu^{II}_{(x)}Fe^{II}_{(1-x)}Fe^{III}_2O_4$ NPs. Continuous scan mode with 0.02°/sec scanning rate was followed in the measurement of all the samples. The data collections and evaluations were carried out with an X'Pert Data Collector (v.: 2.0e) and an X'Pert High Score Plus software. (v.: 2.2e (2.2.5), PAN analytical B.V., Almelo, Netherlands).

Debye-Scherrer equation (Equation (17)) was used to calculate the average crystallite size of simple oxide and ferrite NPs.

$$D = \frac{0.9\,\lambda}{\beta cos\theta} \tag{17}$$

where D represents the crystallite size, λ is the wavelength (0.1541 nm) of the X-ray source, and β can be obtained from the experimental peak width (FWHM) of the average of three most intense peaks, and θ is the XRD peak position.

3.4.3 Determination of specific surface areas

The Brunauer-Emmett-Teller (BET) method was applied to determine the specific surface area of the catalyst. In this method, a Micromeritics ASAP 2000 type instrument (Micromeritics Instrument Corporation, Norcross, GA, USA) was used to measure N_2 adsorption/desorption isotherms, from which the specific surface areas could be determined. In each case, 1 g sample was previously outgassed in vacuum at 160 °C.

3.4.4 Raman spectroscopic measurements

A Bruker RFS 100/S FT – Raman spectrometer (Bruker Corporation, Billerica, MA, USA) equipped with a liquid N_2 cooled Ge-diode detector and a Nd:YAG laser (1064 nm, operated at 150 mW) was used for the Raman spectroscopic measurements of metal oxides and ferrites. Raman spectra of the samples were obtained by the co-addition of 512 scans with a resolution of 2 cm^{-1}.

3.4.5 Scanning electron microscopy (SEM)

The surface morphology of the sample was recorded by using a Thermo Scientific™ scanning electron microscope (Thermo Fisher Scientific Inc., Waltham, MA, USA). The sample was ground manually in an agate mortar. The obtained fine-ground sample was fixed to a well-known cylindrical aluminum sample holder with an electrically conductive double-sided adhesive tape. The excess particles were removed from the surface of the sample holder with compressed air. The equipment (an APREO S model) was used with beam current in the range 0.80–1.60 mA, accelerating voltage of 20 kV and a low vacuum secondary electron detector.

3.4.6 Energy dispersive X-ray spectroscopy (EDS)

An EDAX AMETEK (Mahwah, NJ, USA) spectrometer equipped with an octane detector using TEAM™ software (v. 4.5, EDAX AMETEK Inc., Mahwah, NJ, USA) was used for recording the spectra and for the subsequent EDX spectral analysis of the uncoated samples. Generally conductive taps or films are used for coating material before EDX analysis. These taps or films may give rise to different inconveniences, such as sample alteration and absorption of soft X-rays emitted by the sample, generation of undesired characteristic photons within the conducting material and attenuation and deviation of primary electrons. That's why uncoated samples were used in this study for EDX investigations.

3.4.7 Measurement of particle size distribution (PSD)

For the measurement of particle size distribution (PSD), a dynamic light scattering equipment, Zetasizer NanoZS (Malvern Instruments Ltd, Malvern, Worcestershire, U.K.) was employed.

3.4.8 Diffuse reflectance spectroscopy (DRS)

A Perkin Elmer LS50 B spectrofluorometer (PerkinElmer Inc., Waltham, USA) was applied to record the scattering spectra of the samples in a solid phase at a wavelength range of 250-600 nm. The obtained spectra were used to determine the band-gap energy of the samples. In this DRS equipment, barium sulfate was used as the reference (I_0) to measure the reflectance (R) (Equation (18)). After the calculation of reflectance (R), the values are inserted in the Kubelka-Munk function (Equation (19)) [191]. Finally, the values must be presented depending on the excitation energy (in eV = electron volt), the cross-section point of the extrapolated linear portion of the curve on to *X*-axis will give the band-gap energy (eV) for the powder sample.

$$R = \frac{I}{I_0} \tag{18}$$

$$f(R) = \frac{(1-R)^2}{2R} \tag{19}$$

3.5 Assessment of Photocatalytic Activity

3.5.1 Energy source and photo-reactor configuration

The energy source and photo-reactor configuration are key components of a photocatalytic system. An Optonica SP1275 LED lamp (GU10, 7 W, 400 Lm, 6000 K, Optonica LED, Sofia, Bulgaria) was applied as the potential energy source for the visible-light induced photocatalytic reactions. All reactions were performed in a 1-cm pathlength quartz cuvette fitted directly inside an S600 diode-array spectrophotometer (Figure 10A) at room temperature (25±2 °C). In all cases, the total volume of the reaction mixture in the quartz cuvette was 3 ml.

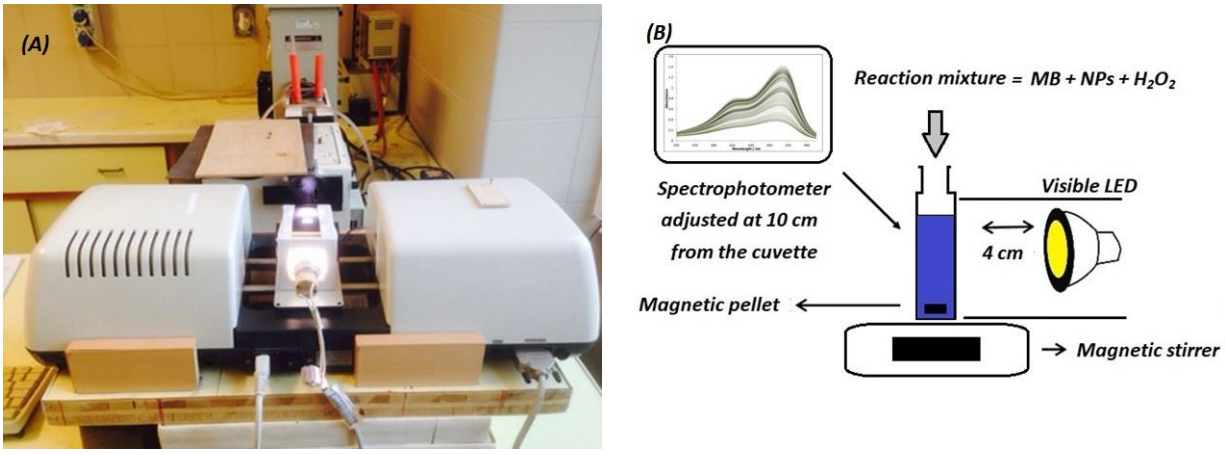

Figure 10. Configuration of the photocatalytic reactor fitted directly inside an S600 spectrophotometer (A), schematic representation of the photocatalytic reaction showing the stirring mechanism and visible light irradiation (B).

3.5.2 Photocatalytic experiments using methylene blue as model compound

In all photocatalytic experiments, some conditions were kept constant such as MB concentration (1.5×10^{-5} mol/L), reaction time (140 min), and reaction temperature (25±2 °C). In the first step, control experiments were designed to check the possible self-degradation of MB in dark and in visible-light induced degradation. The stability of MB in dark and its photosensitivity to visible light was confirmed from the previously published reports [159, 192]. Keeping these reports in mind, we investigated the reaction rate of visible-light induced self-degradation of MB. Next, the reaction rate of the photo-Fenton reaction was measured, where hydrogen peroxide (H_2O_2) was added to the reaction mixture in the concentration (0.01 M) recommended in related photo-Fenton studies [108].

In the subsequent step, a heterogeneous photo-Fenton system was developed applying $Cu^{II}_{0.4}Fe^{II}_{0.6}Fe^{III}_{2}O_4$ (abbreviated as NP-3) in the concentration of 22.73 mg/L for MB degradation. To achieve adsorption/desorption equilibrium, the catalyst and MB mixture was stirred by using a magnetic stirrer in a dark place for 30 min. Then, 3 ml of the mixture was put into the quartz cuvette and the initial pH was checked before the addition of oxidant (H_2O_2 as Fenton reagent). The cuvette containing the reaction mixture was adjusted in the sample holder of the S600 spectrophotometer and stirred continuously. A magnetic stirrer was fixed below the photoreactor (cuvette) and a small magnetic pellet was added to the reaction mixture inside the cuvette to carry out stirring (Figure 10B). Commercial H_2O_2 in the above mentioned concentration was added and the window for visible light was opened to initiate the photo-Fenton reaction.

During photocatalysis, the absorption spectra were recorded continuously throughout the experiment (140 min). The reaction rates, using simple metal oxides and iron(II)-doped copper ferrites, were investigated. Furthermore, the effects of NPs dosage, H_2O_2 concentration, and pH on the MB degradation were also explored. Finally, the stability and reusability of NPs in this heterogeneous photo-Fenton system were studied.

Beer-Lambert law was followed in the calculation of the absorbance at specific time interval for each photocatalytic experiment (Equation (20)).

$$A_{\lambda,t} = \varepsilon_\lambda c_t \ell \tag{20}$$

In Equation (20), the absorbance as the function of wavelength (λ) and time (t), is represented by the symbol A, the molar absorbance of dye as the function of wavelength is symbolized as ε (M^{-1} cm^{-1}), the dye concentration (M) as the function of time during the photolysis in the solution is represented as c, and the pathlength of the quartz cuvette as ℓ (cm). The unit of wavelength (λ) is nm and time (t) is s.

From the changes in the absorbance, dA/dt (1/s), observed at all intervals during the allocated experiment time (140 min), the reaction rate (dc/dt) was calculated. The dA/dt (1/s), can be calculated from the slope (m) of the degradation absorption curve (A vs. t, Equation (21)).

$$\frac{dc}{dt} = \frac{\frac{dA}{dt}}{\varepsilon\, \ell} \tag{21}$$

It can also be declared on the basis of spectral changes observed after the complete photo-Fenton degradation of MB (see later in Section 4.3.5) that the intermediates and end-products have no major absorption peaks in the UV and visible range. Therefore, the decrease of absorbances at maximum wavelength λ_{max} (665 nm for MB) could be used for the determination of reaction rate. The molar absorbance (ε) of MB, measured in this study, was 89171 M^{-1} cm^{-1}, which is close to the value (95000 M^{-1} cm^{-1}) [193] reported in the literature. However, baseline problems in the recorded spectra were observed as a result of scattering caused by addition of solid catalysts into the reaction mixture. These baseline problems were eradicated by applying linear baseline corrections during the determination of the reaction rate.

3.5.3 Photocatalytic experiments using rhodamine b as model compound

The reactor configuration for RhB was the same as applied in MB photocatalytic reactions. The concentration of RhB (1.75×10^{-5} mol/L), reaction time (140 min), and reaction temperature (25±2 °C) were kept constant throughout RhB photocatalysis.

In the case of RhB, too, control experiments were performed prior to addition of the NPs to system. In the first step, the potential self-degradation of RhB in dark and photo-induced degradation was investigated, and the reaction rates were determined. In the next step, a photo-Fenton system was compiled, where H_2O_2 was added in the concentration (0.176 M). The catalyst $Cu^{II}_{(0.4)}Fe^{II}_{(0.6)}Fe^{III}_2O_4$ (abbreviated as NP-3) in the concentration of 400 mg/L was added to the mixture and stirred for 30 min to ensure a good dispersion of NP-3 and to eliminate the effect of surface adsorption of RhB on the catalyst during the photo-degradation. The reaction rates in each case were determined and compared.

Furthermore, the process variables investigated were the catalyst dosage (80 to 800 mg/L), hydrogen peroxide concentration (2.19×10^{-2} mol/L to 3.04×10^{-1} mol/L), and pH (2 to 12). Meanwhile, the original pH of the total aqueous solution was in the range of 7.5 to 8.0. The pH was adjusted by adding HCl or NaOH before starting the photocatalytic experiment.

The total degradation of RhB was confirmed (see later in Section 4.4.5) on the basis of UV/visible spectra obtained after photocatalysis. The intermediates and end-products of the RhB photo-Fenton degradation exhibit no significant bands in the UV and visible ranges of the spectrum. Thus, the reaction rate of RhB degradation can be determined from the main absorption peak λ_{max} (554 nm for RhB). The molar absorbance (ε) of RhB, measured in this study, was 91866 M^{-1} cm^{-1}, which is close to the value (88000 M^{-1} cm^{-1}) [194] published in the literature. The baseline problems occurred in the recorded spectra as a consequence of NPs addition to system was solved by using linear baseline corrections during the determination of the reaction rate.

3.6 Investigating the stability of catalysts

In a heterogeneous catalytic system, the leaching of metal ions from the catalyst surface into the reaction mixture is a crucial point to consider. Here too, ICP measurements and spectrophotometry were applied to investigate the possible leaching of metal ions during the irradiation. In the MB photodegradation using NP-3 catalyst, under optimum reaction conditions, suitable ligands (such as SCN^- for Fe^{3+} or phenanthroline for Fe^{2+} and Cu^{2+}) were applied for the spectrophotometric analysis. Their detection limits were 4.8 × 10^{-7} M, 9.0 × 10^{-7} M, and 3.3 × 10^{-7} M, taken 0.01 as minimum detectable absorbance. After the removal of the dispersed catalyst from the solution, the total release of metal ions was observed much below 1%.

This phenomenon was confirmed by ICP measurements, too. Applying 400 mg/L catalyst, the concentrations of the dissolved iron and copper were 672.5 ± 28.4 µg/L and 175 ± 9.8 µg/L respectively. These values correspond to 0.272 ± 0.011% and 0.404 ± 0.023% respectively.

3.7 Investigating the reusability of catalysts

After the synthesis of a stable catalyst, scientists discover its reusability for few cycles in heterogeneous Fenton system. At the optimum reaction conditions, a five-step experiment was designed to investigate the reusability of NP-3 (doped copper ferrite) and simple oxide composite ($Fe^{II}O/Cu^{II}O/Fe^{III}{}_2O_3$). When in the first cycle, the MB in the cuvette was completely degraded, the photo-reactor system was placed in dark for 12 hours to achieve the total decay of residual hydrogen peroxide. In the second cycle, the same

amount of fresh MB and H_2O_2 were added to the cuvette containing catalyst, and the reaction was started again for the same period of time. Similar procedure was repeated for five cycles. The reaction rate (apparent kinetic constant) was recorded for each cycle and compared.

3.8 Total organic carbon (TOC) measurements

Total organic carbon is considered as a key technique to investigate the degradation performance of a system. The total organic carbon (TOC) of samples was determined by using a TOC analyzer (Shimadzu, model TOC-L). The instrument was operated at 680 °C furnace temperature and 20 mL sample injection.

In this research, TOC measurements were performed after photodegradation of MB at optimized conditions. However, TOC investigation was not practically performed parallel to the spectrophotometry due to the too small volume of solution (3 mL) used in the photoreactor (cuvette).

3.9 Antimicrobial assessments

Luminoskan Ascent luminometer (Thermo Scientific) was applied for the measurement of antibacterial property of simple metal oxide and doped NPs in the *Vibrio fischeri* bioluminescence inhibition assay. According to the manufacturer (Hach Lange Co., Germany) recommendations, a gram negative test specimen *Vibrio fischeri* (NRRL-B-11177) suspension was prepared. The life-span of the test specimen was 4 h after reconstitution. The same test protocol was followed as reported in literature [195].

During the evaluation, the results obtained from 2 parallel measurements were averaged and then the relative inhibition$_t$ (%) was calculated by using Equation (22):

$$Relative\ inhibition_t(\%) = \frac{I_{control(t)} - I_{sample(t)}}{I_{control(t)}} * 100 \quad (22)$$

where $I_{control(t)}$ is the emission intensity of the control samples and $I_{sample(t)}$ = the emission intensity of the test samples.

4. Results and discussions

4.1 Assessment of the experimental Cu/Fe ratios in the synthesized catalysts

Cu/Fe ratios in the final products (after calcination) determined by ICP measurements also confirmed the precipitation of metal salts. The details about theoretical and experimental Cu/Fe ratios and the deviation (%) are given in Table 3. It is obvious that the deviations (%) in all cases are within 5%.

Table 3. Comparison of theoretical and experimental Cu/Fe ratios of the catalysts prepared

$Cu^{II}_{(x)}Fe^{II}_{(1-x)}Fe^{III}_{2}O_4$	x = 0.2	x = 0.4	x = 0.6	x = 0.8	x = 1
Sample name	NP-2	NP-3	NP-4	NP-5	NP-6
Theoretical Cu/Fe ratio	0.071	0.154	0.250	0.364	0.500
Experimental Cu/Fe ratio*	0.068	0.148	0.244	0.353	0.479
Deviation (%)	4.22	3.90	2.40	3.02	4.20

**Determined by inductively coupled plasma (ICP) measurements*

4.2 Characterization of simple metal oxides and iron(II) doped copper ferrites NPs

4.2.1 Particle size distribution (PSD)

In the structural elucidation of catalysts, the particle size distribution was used to confirm that the NPs were under sub-micrometer size. NP-3 was investigated for the particle size analysis, being in the middle of the series of six doped ferrites. It is obvious from Figure 11 that our catalysts were primarily in the range of 70–200 nm. These nanometer-size particles were favorable for their photocatalytic applications as nanodispersions.

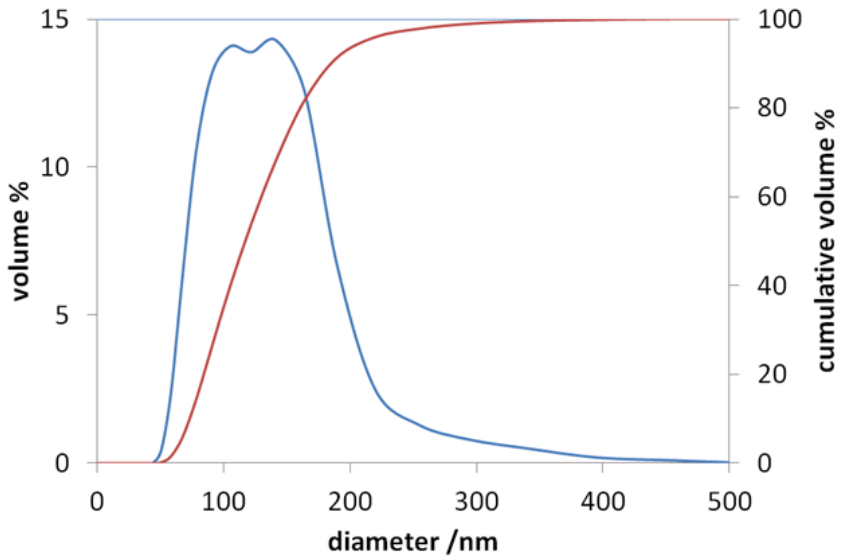

Figure 11. Particle size distribution of $Cu^{II}_{0.4}Fe^{II}_{0.6}Fe^{III}_{2}O_4$ (NP-3)

4.2.2 X-ray diffraction (XRD) measurements

The XRD patterns of the prepared metal oxides and iron(II)-doped copper ferrites are shown in Figure 12. The octahedral positions in this arrangement are occupied by the metal ions with +2 charge such as, Fe^{2+} or Cu^{2+}. However, the major part of the metal ions with +3 charge (Fe^{3+}) can be found in tetrahedral configuration [196]. Also, this arrangement remains consistent during the substitution of Cu^{2+} ions to Fe^{2+}in the iron(II) doped copper ferrites.

A very slight change was observed in the main peak at about 35 deg (2θ) in the XRD diffractograms (Figure 12): 35.6 deg in Fe_2O_3 (hematite) for the crystal plane with (110) Miller indices, 35.4 deg in Fe_3O_4 (magnetite, x = 0 NP-1) for (311) crystal plane, 35.9 in $CuFe_2O_4$ (copper ferrite, x = 1 NP-6) for (211) crystal plane, 35.5 deg in $Cu^{II}O$ (tenorite) for (002) crystal plane. The positions of few common peaks change slightly stronger (shift) at about 58 and 63 deg, owing to the small difference in the size of the metal ions: iron(II) ions have 77 pm ionic radius in tetrahedral, and 92 pm in octahedral coordination geometry, while copper(II) 71, and 87 pm, respectively [197]. Already in the diffractogram of magnetite, new peaks appeared compared to that of hematite, as the consequence of the presence of metal ions with +2 oxidation state in the ferrite structure: at 30 and 43 deg. These peaks can be observed and assigned in the diffractograms of all nanoparticles, mainly in those of NP-1, NP-5 and NP-6, but their intensities were low in

NPs 2-4, however, totally missed from $Fe^{III}_2O_3$ and $Cu^{II}O$. This phenomenon may confirm the significant structural changes in the composites compared to the simple metal oxides.

On the basis of the XRD evaluation, our $Fe^{II}O$ sample contained not only wüstite fraction, but maghemite, too, as the consequence of the potential partial oxidation of Fe^{2+} ions to Fe^{3+} during the calcination.

There are several peaks in Figure 12 (at 24, 33, 41, 49, 64 deg), which belong to hematite (red dashed line) without the possible assignment to the magnetite. This means that a partially separated hematite fraction is in NPs 1-4 with a decreasing ratio, together with the increase of the Cu^{2+} content. However, tenorite (blue dashed line) did not compose a distinct fraction in a significant measure, not even in NP-6. The main XRD peaks in doped copper ferrites, on the basis of miller indices and their respective positions, are in considerable agreement with the standard data (JCPDS card no: 34-0425) for inverse spinels [198]. In addition, the XRD peaks of $Cu^{II}O$, $Fe^{III}_2O_3$, and Fe_3O_4 were indexed with JCPDS card no: 41-0254 [199], JCPDS card no: 33-0664 [200], and JCPDS card no: 19-0629 [201], respectively.

In the diffractogram of $Fe^{III}_2O_3$ (Figure 12), small peaks (at 28.9, 31.6, 45.4 deg) were observed, which belong to NaCl impurity, according to JCPDS card no: 78-0751 [202]. However, these peaks were absent in the XRD patterns of other oxides and doped ferrites.

The average crystallite size of the $Cu^{II}O$ nanoparticle was found to be 18.85 nm (Figure 13). However, in the case of $Fe^{III}_2O_3$, the crystallite size was 36.84 nm and the main characteristic XRD peaks were in line with the characteristic XRD pattern of hematite with some traces of magnetite. The average crystallite size of $Fe^{II}O$ was 37.06 nm and, on the basis of the XRD evaluation, our $Fe^{II}O$ sample contained not only wüstite fraction as previously indicated. However, doped copper ferrites revealed slightly decreasing trend in the average crystallite size with the increase of the Cu^{2+} and decrease of the Fe^{2+}content.

The effect of calcination temperature on XRD patterns of NP-3 synthesized under different calcination temperature are shown in Figure 14. No significant changes in the peaks positions were observed with increase in calcination temperature. The inverse spinel

structure of ferrites remains throughout the series. Although, the intensity of the peaks increased with increase in calcination temperature, which indicates increase in the crystallinity of the material. The increase in the intensity of hematite peaks (at 24, 33, 41, 49, 64 deg) and tenorite peak (at 39 deg) represents the formation of separate phases at higher calcination temperature (Figure 14).

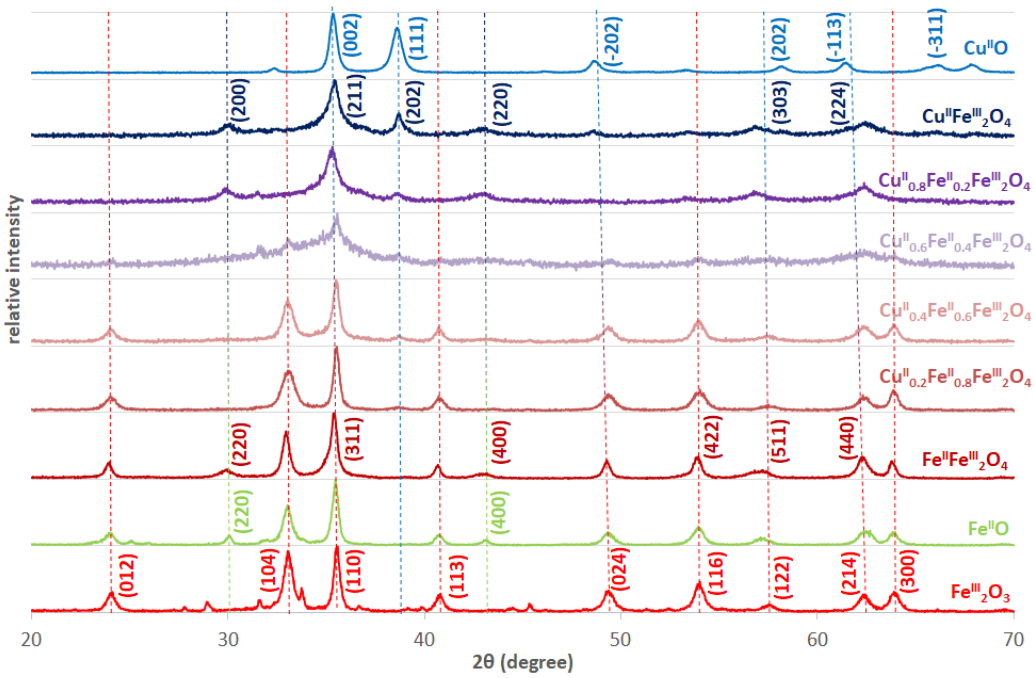

Figure 12. X-ray diffraction (XRD) diffractograms of iron(II) doped copper ferrites compared to those of the simple oxides of the given metal ions. The characteristic Miller indices indicated for the compounds the standards of which were earlier studied by XRD are taken from the International Centre for Diffraction Data.

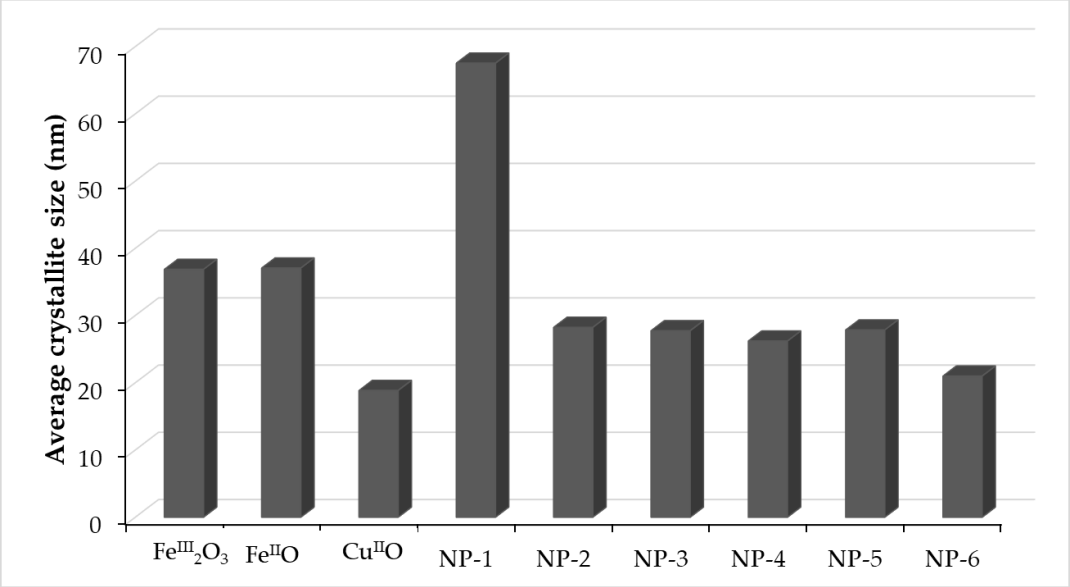

Figure 13. Comparison of the average crystallite size of simple metal oxides and copper doped ferrites

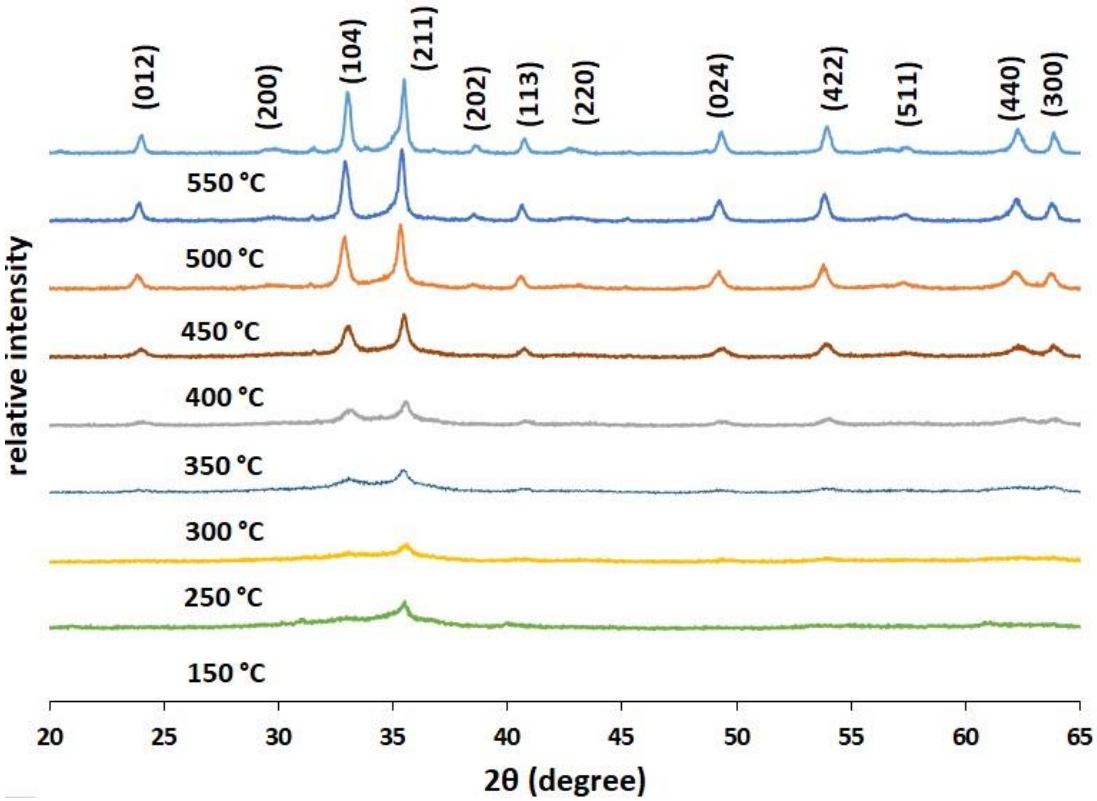

Figure 14. X-ray diffraction (XRD) diffractograms of NP-3, synthesized with increase in the calcination temperature. The characteristic Miller indices indicated of the standard compounds are taken from the International Centre for Diffraction Data.

4.2.3 Raman measurements

The Raman spectra of metal oxides and doped copper ferrites are given in Figure 15. The vibrations under 600 cm^{-1} correspond to the M–O bonds at the octahedral sphere [203]. Only one band belongs to the metal ions with tetrahedral coordination sphere: the symmetric stretching at 610 cm^{-1} (ν_s(M–O), E_g symmetry). The frequency (wavenumber) of this band slightly changes during the insertion of Cu^{2+} ion into the crystal structure as the consequence of the previously mentioned difference in the size of the metal ions. Similar spectral changes can be observed in the case of the antisymmetric bending (δ_{as}(M–O), A_{1g} symmetry) at 500 cm^{-1}, and the symmetric bendings (δ_s(M–O), E_g symmetry) at 410 and 295 cm^{-1} for metal ions with an octahedral coordination sphere [204]. However, the position of the band at 225 cm^{-1} does not change during the Cu^{2+} insertion, rather, its intensity decreases, then totally disappears up to NP-4 (x = 0.6), similar to several peaks in the XRD diffractograms (Figure 15). This antisymmetric bending belongs to the Fe^{III}–O bonds in the partly separated hematite fraction. The further peaks under 200 cm^{-1} are the signals of non-assigned external vibration modes. The intensities of these bands strongly increase together with the Cu^{2+} ratio. Also, the Raman spectra of NPs confirm the inverse spinel structure [198].

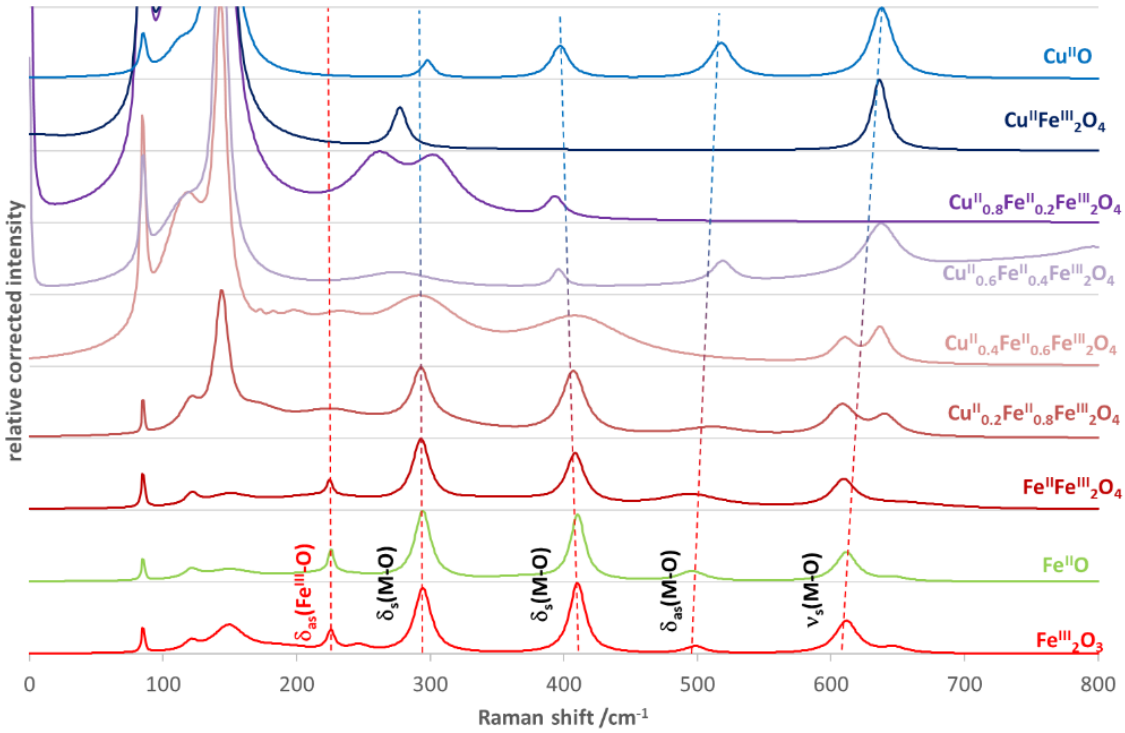

Figure 15. Raman spectra of iron(II) doped copper ferrites compared to those of the simple oxides of the given metal ions.

4.2.4 Scanning electron microscopy (SEM) measurements

The surface morphologies of simple metal oxides and NP-3 are shown in Figure 16A – D. Figure 16A revealed that Cu^{II}O exhibited bead-like uniform structure connected together in threads. Cu^{II}O in the form of nanowires, nano sheets, nano ribbons, nano leaves nano rods, and flower-like and grass-like nanoparticles have already been reported [205]. Bead-like Cu^{II}O prepared in this study showed a morphology totally different from those of these materials. Fe$^{III}_2$O$_3$ showed rod-like structure with some hexagonal crystals (Figure 16B). Fe$^{III}_2$O$_3$ in the form of nano husk, nano rods, nano cubes, and porous spheres were previously explored [206]. Fe^{II}O possessed pallet-like structure (Figure 16C). However, earlier researches reported Fe^{II}O in the form of nanowires and nanocubes. Though, NP-3 had needle-like units, embedded into clusters (Figure 16D), which is different from the already published spherical structure of copper ferrite [207]. From SEM investigations it is clear that Cu^{II}O and NP-3 had very uniform structures.

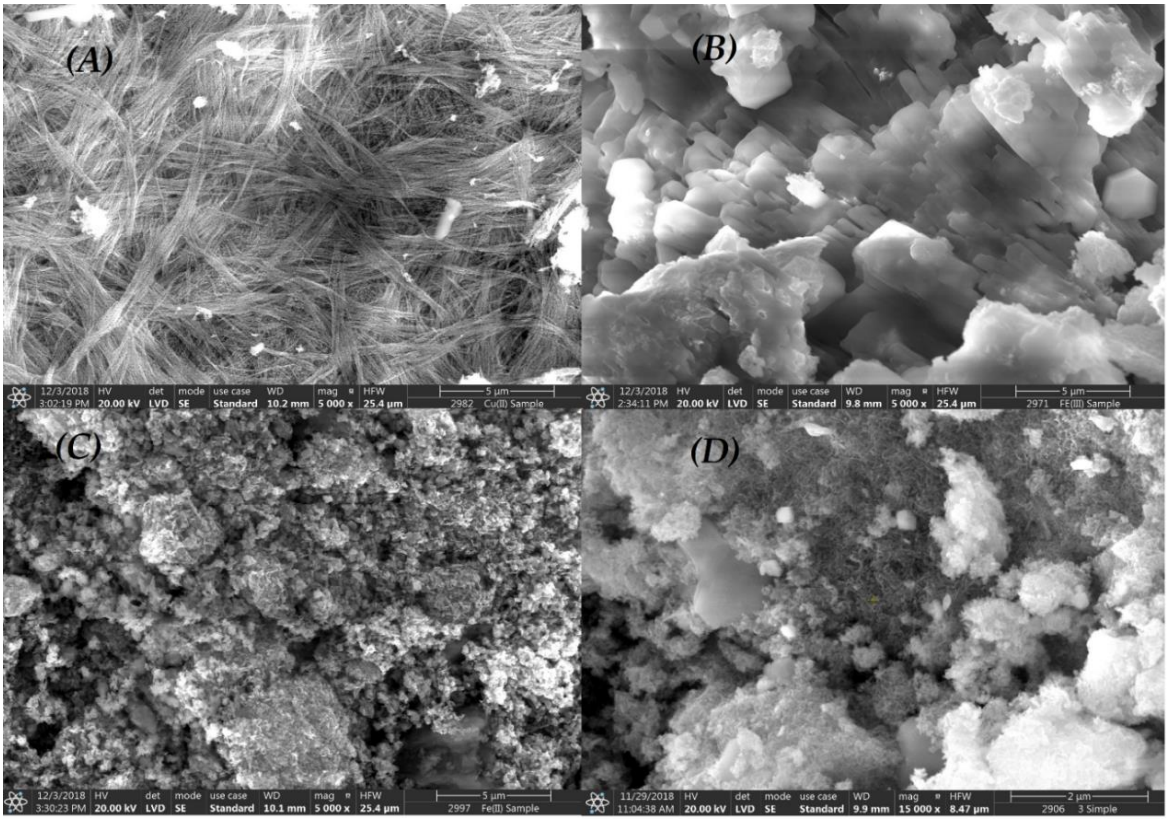

Figure 16. Scanning electron microscopy (SEM) images of synthesized catalysts: (A) $Cu^{II}O$, (B) $Fe^{III}_2O_3$, (C) $Fe^{II}O$ and (D) NP-3

SEM images of the synthesized catalysts ($Cu^{II}_{(x)}Fe^{II}_{(1-x)}Fe^{III}_2O_4$) NPs at various concentrations of metal salts (where x = 0.0, 0.2, 0.4, 0.6, 0.8, 1.0) are shown in Figure 17A–F. Figure 17A revealed about NP-1 (x = 0) small agglomerated nanostructures, which were totally different from the others in the series of the six NPs prepared. As a consequence of increasing Cu^{2+} ratio (x), the structure of NPs significantly changed from spherical to needle-like, embedded into clusters, in the case of NP-2 (x = 0.2, Figure 17B) and NP-3 (x = 0.4, Figure 17C). NP-4 (x = 0.6, Figure 17D) formed larger needles on the surface, while NP-5 (x = 0.8, Figure 17E) and NP-6 (x = 1, Figure 17F) in their deeper, hexagonal crystals originating from a secondary nucleation.

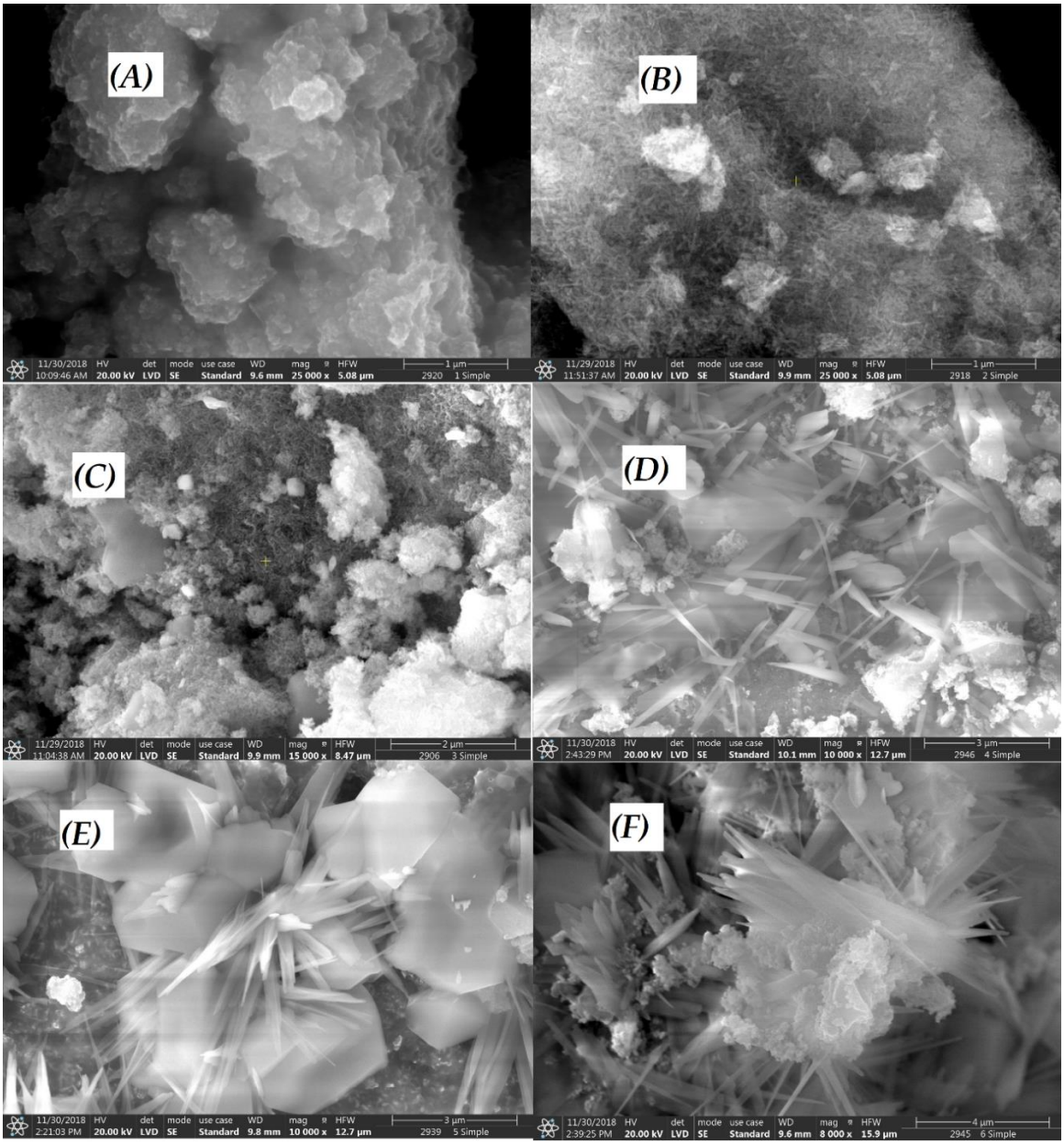

Figure 17. Scanning electron microscopy (SEM) images of $Cu^{II}_{(x)}Fe^{II}_{(1-x)}Fe^{III}_2O_4$: (A) x = 0 NP-1, (B) x = 0.2 NP-2, (C) x = 0.4 NP-3, (D) x = 0.6 NP-4, (E) x = 0.8 NP-5, (F) x = 1 NP-6 ferrites.

The effect of calcination temperature on the surface morphology of NP-3 was investigated as shown in Figure 18A-F. At lower calcination temperatures ranging from 150 to 300°C, the needle-like morphology of NP-3 was not clearly visible (Figure 18A & B). However, at around 450 °C (Figure 18C), this needle-like morphology occurred which can also be seen in catalysts synthesized at 550 °C (Figure 18D).

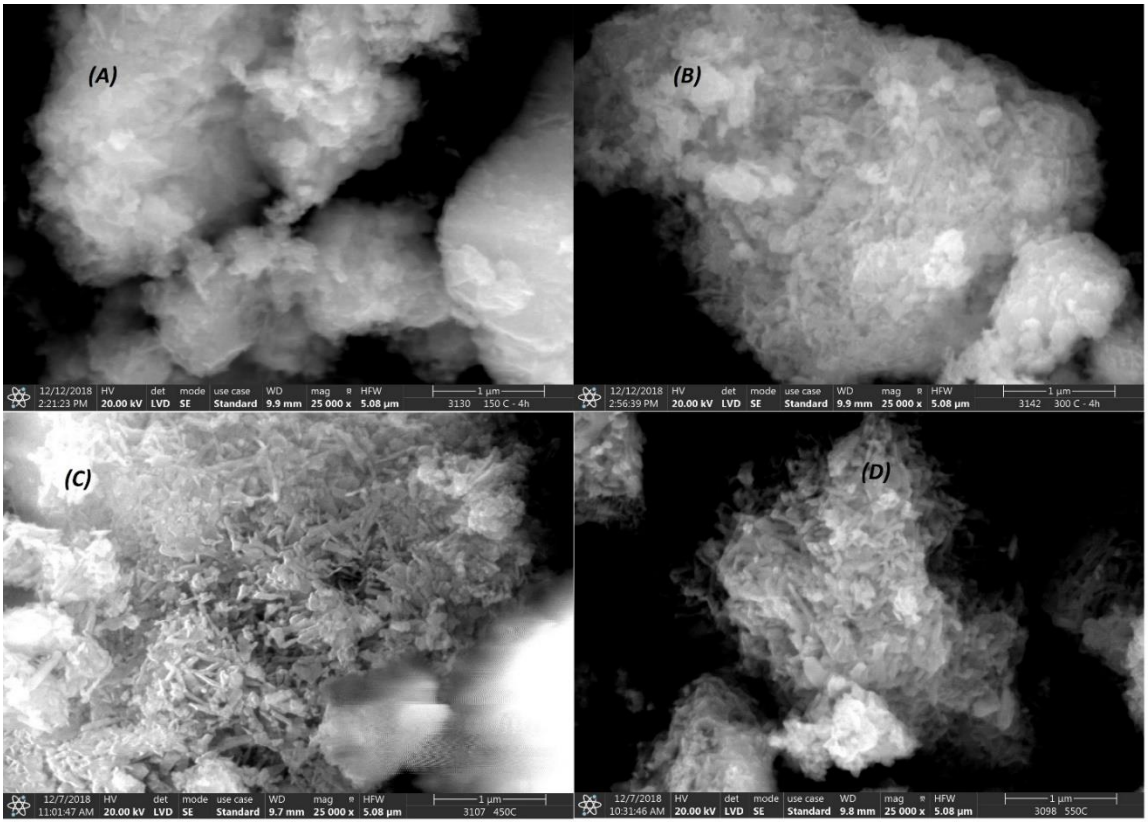

Figure 18. Scanning electron microscopy (SEM) images of NP-3 catalyst synthesized under different calcination temperatures: (A) 150 °C (B) 300 °C (C) 450 °C and (D) 550 °C.

4.2.5 Energy dispersive x-ray (EDX) spectroscopy measurements

The EDX analysis of simple metal oxide NPs was carried out along with SEM in scan mode (the area of measurement is 1.358 square millimeters and the duration is 120 s) giving average intensity values for the constituents. From Figure 19A, it was observed that $Cu^{II}O$ indicated characteristic peaks of Cu K_α, Cu K_β, Cu L_α, O, and C, and contained no significant impurities. $Fe^{III}{}_2O_3$ showed peaks of Fe K_α, Fe K_β, Fe L_α, O, and C. More significant Na and Cl peaks were observed in the EDS spectrum of $Fe^{III}{}_2O_3$ (Figure 19B). $Fe^{II}O$ indicated peaks of Fe K_α, Fe K_β, Fe L_α, C and O, also showing slightly lower peaks of Na and Cl (Figure 19C).

The EDX spectral analysis of $Cu^{II}{}_{(x)}Fe^{II}{}_{(1-x)}Fe^{III}{}_2O_4$ NPs was also carried out along with SEM in scan mode giving average intensity values for the constituents. NP-1 (x = 0, Figure 20A) showed the major characteristic peaks of Fe K_α, Fe K_β, Fe L_α and O, while smaller peaks of Na and Cl were also observed. NP-3 (x = 0.4, Figure 20B) displayed the same characteristic peaks as well as the characteristic bands of Cu: K_α, K_β, and L_α. More

significant Na and Cl peaks were observed in the EDX spectrum of NP-5 (x = 0.8, Figure 20C), the SEM image of which also revealed the presence of NaCl cubic crystals. The dominant impurities in the NPs were Na and Cl, originating from $FeCl_3$ and NaOH applied for all precipitation reactions, and some traces of sulfur (SO_4^{2-} anion of other metal salts), aluminum, silicon, and manganese (accompanying metal ions of iron salts) were also observed.

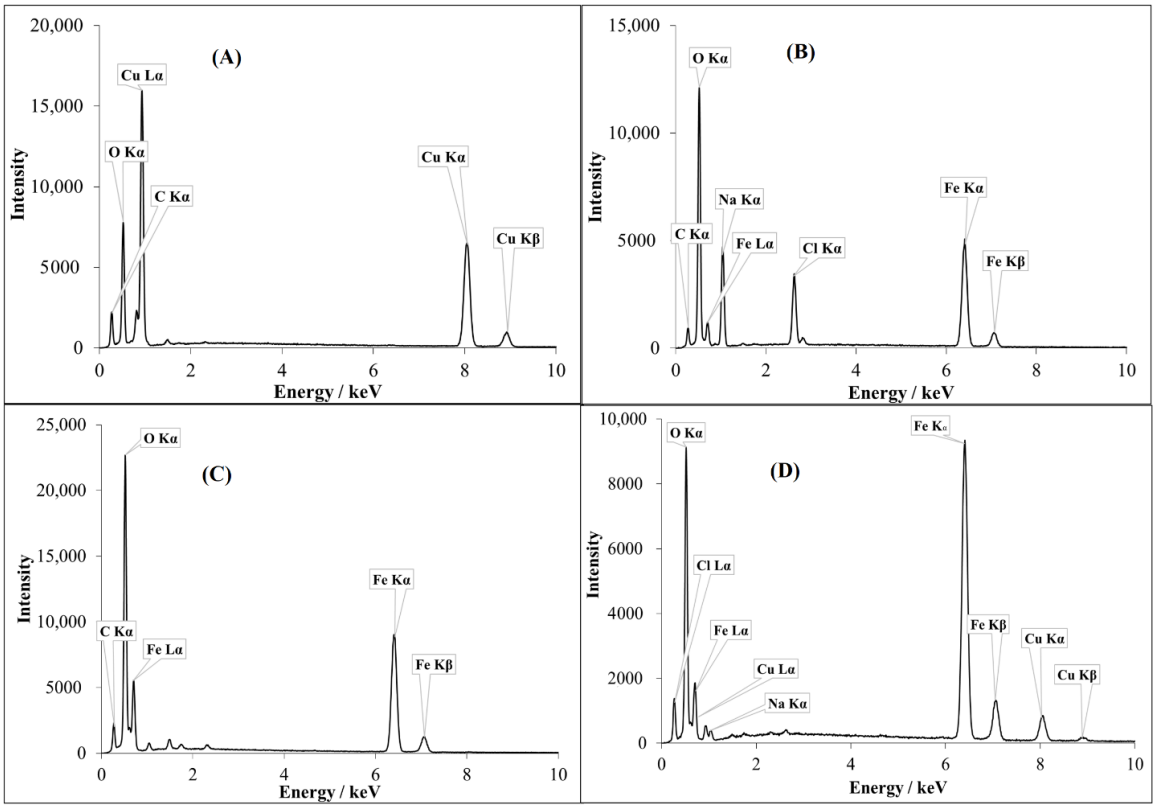

Figure 19. EDX spectra (recorded in scan mode) for simple metal oxide NPs (A) $Cu^{II}O$ (B) $Fe^{III}_2O_3$, (C) $Fe^{II}O$ and (D) NP-3

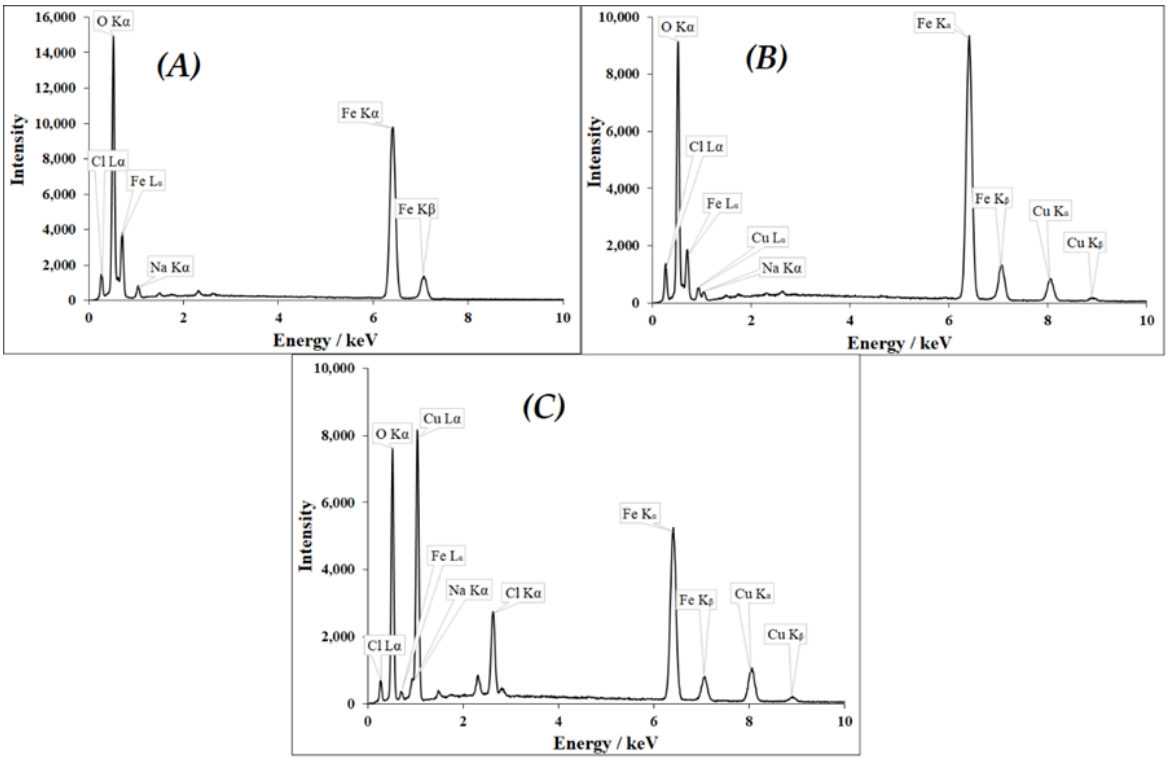

Figure 20. EDX spectra (recorded in scan mode) of doped ferrites ($Cu^{II}_{(x)}Fe^{II}_{(1-x)}Fe^{III}_2O_4$): (A) x = 0 NP-1 (B) x = 0.4 NP-3 and (C) x = 0.8 NP-5.

Additionally, we have made a comparison of the EDX spectral results in spot mode, regarding the NP-5 catalyst, the SEM image of which displayed distinct needle-like and cubic crystals (see Figure 17E). The EDX spectral results for the spot containing the cubic structure (Figure 21A) displayed more intense peaks characteristic of Cl, especially at about 2.6 keV, while for that containing mostly needle-like structure (Figure 21B) more intense characteristic peaks of Fe (see at 6.3 keV) and Cu (see at 8 keV) are shown. Compared these EDX spectra to that regarding NP-5 but taken in scan mode (Figure 20C), it is clearly seen that the latter is a mixture of the previous two, indicating that this catalyst, in accordance with its SEM image, involves both structures. The cubic crystal is mainly composed of NaCl, which can be seen from the intense peaks in Figure 21A, while Fe, Cu, O, S and Al peaks were also present. On the other hand, the needle-like crystals revealed Fe, Cu, O, Al, S and low intensity Na and Cl peaks.

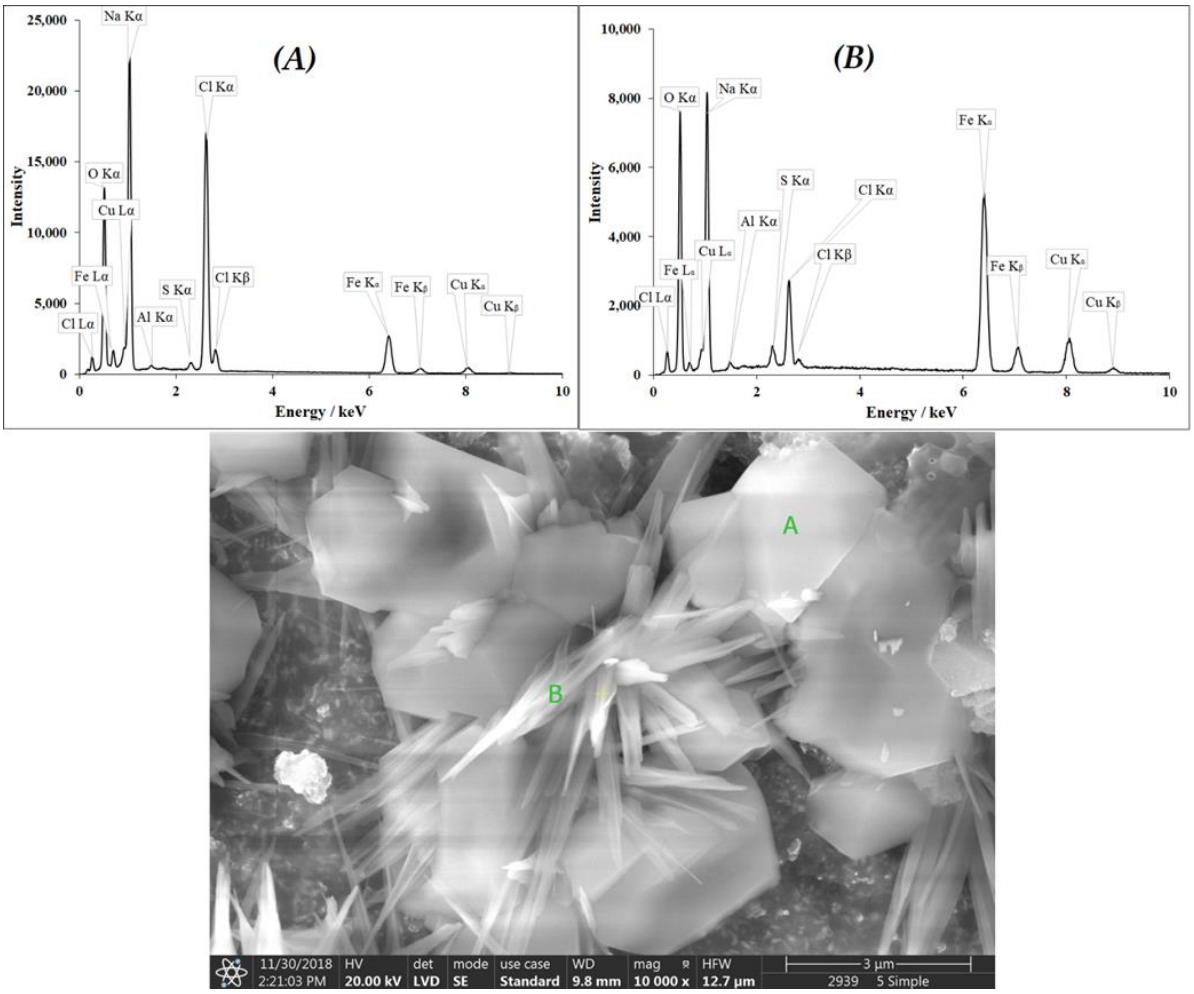

Figure 21. EDX spectra (recorded in spot mode) of the NP-5 catalyst ($Cu^{II}_{(x)}Fe^{II}_{(1-x)}Fe^{III}_2O_4$, x=0.8), regarding the spot on cubic (A) and needle-like (B) structure.

The effect of calcination temperature on the EDS spectra of NP-3 synthesized under different calcination temperature are shown in Figure 22A-D. The major characteristic peaks of Fe: Kα, Kβ, Lα, Cu: Kα, Kβ, Lα, and O Kα were observed with different intensities in all samples. Na, Cl, Al, S, Mn, Si and other accompanying metal ions were also observed in all samples prepared at different calcination temperatures. The increase in calcination temperature revealed an increase in the intensity of Fe, Cu, O and Cl peaks, which can be attributed to the increase in the formation of separate phases ($Cu^{II}O$, $Fe^{III}_2O_3$ and NaCl) in the structure of doped ferrites. This phenomenon was confirmed by XRD investigations, too.

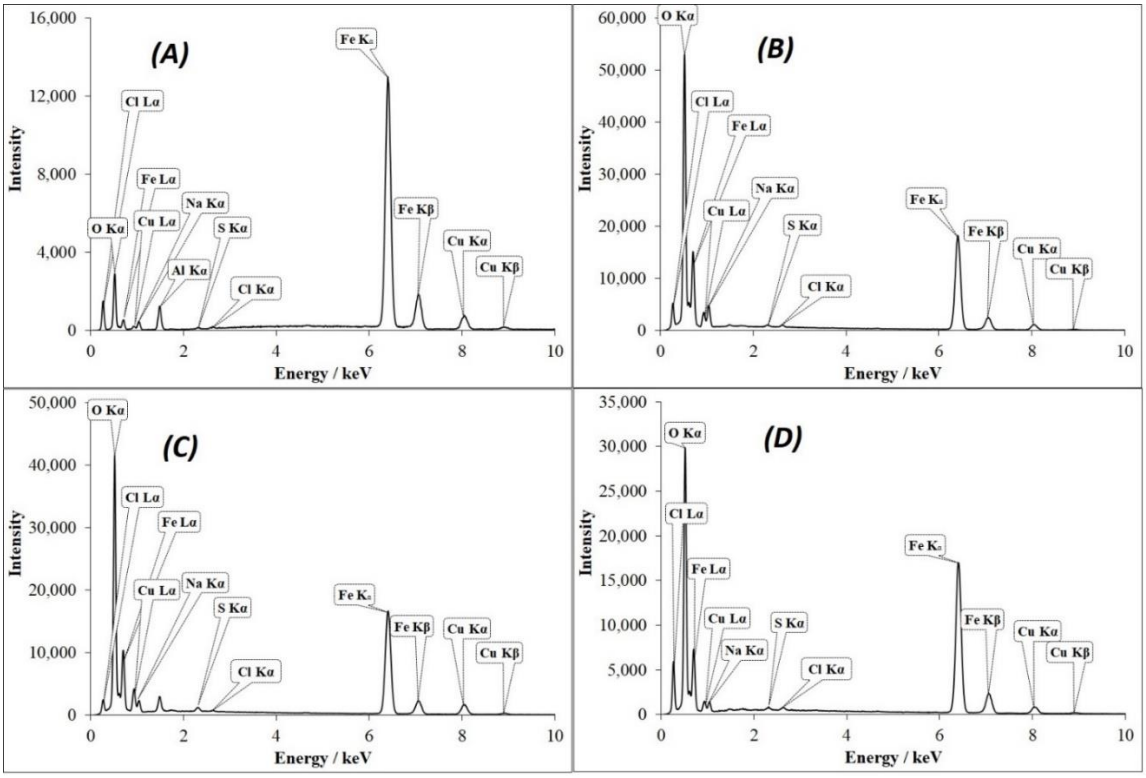

Figure 22. EDX spectra (recorded in scan mode) of doped ferrites NP-3 under different calcination temperatures: (A) 300 °C (B) 450 °C (C) 500 °C and (D) 550 °C.

4.2.6 Determination of specific surface areas

Since the activity of a heterogeneous (solid-phase) catalyst is frequently related to its specific surface area, this property of the prepared iron(II)-doped copper ferrites was also determined by the BET method from N_2 adsorption/desorption isotherms.

As the results indicate (Table 4), the specific surface areas of these catalysts are in a considerable correlation with their morphology. The catalysts consisting of mostly spherical and small needle-like structures (as NP1, NP-2, and NP-3) have significantly lower surface areas than those characterized by larger needles (NP-4, NP-5, and NP-6).

Table 4. Specific surface areas (BET) of the catalysts prepared.

$Cu^{II}_{(x)}Fe^{II}_{(1-x)}Fe^{III}_2O_4$	x = 0 (NP-1)	x = 0.2 (NP-2)	x = 0.4 (NP-3)	x = 0.6 (NP-4)	x = 0.8 (NP-5)	x = 1 (NP-6)
Specific surface area (BET) / $m^2\ g^{-1}$	11.1	20.8	26.0	62.7	64.1	59.3

4.2.7 Diffuse reflectance spectroscopy (DRS) measurements

The whole series of six NPs and simple metal oxides were analyzed for the band-gap energy (E_{bg}) by utilization of the Kubelka-Munk function derived from the DRS spectrum. Figure 23 presents the determination of E_{bg} of NP-3. As shown in Figure 24, an increase in the Cu^{2+}: Fe^{2+} ratio resulted in lower band-gap energies. NP-1 (x = 0) showed higher E_{bg} of 2.02 eV (613 nm), while NP-6 (x = 1) lower E_{bg} of 1.25 eV (995nm).

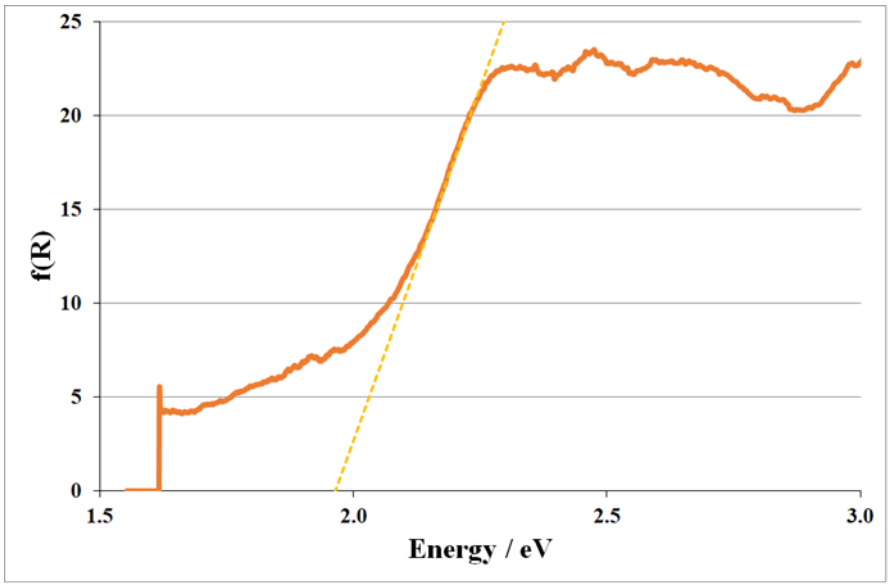

Figure 23. Kulbelka-Munk function for determination of the band-gap energy (E_{bg}) of NP-3.

It means that copper ferrites may be able to harvest the energy of near infrared light in a photocatalytic system, too. The E_{bg} values of the simple metal oxides are in good accordance with those of the doped samples. Comparing our values to those published earlier, in the cases of both simple oxides (such as Fe_2O_3, 2.0 eV [208] and $Cu^{II}O$, 1.2 eV [209]) and copper ferrites (2.12 to 1.90 eV for 0 to 8% Cu content [204]), the corresponding band-gap energies were also in agreement.

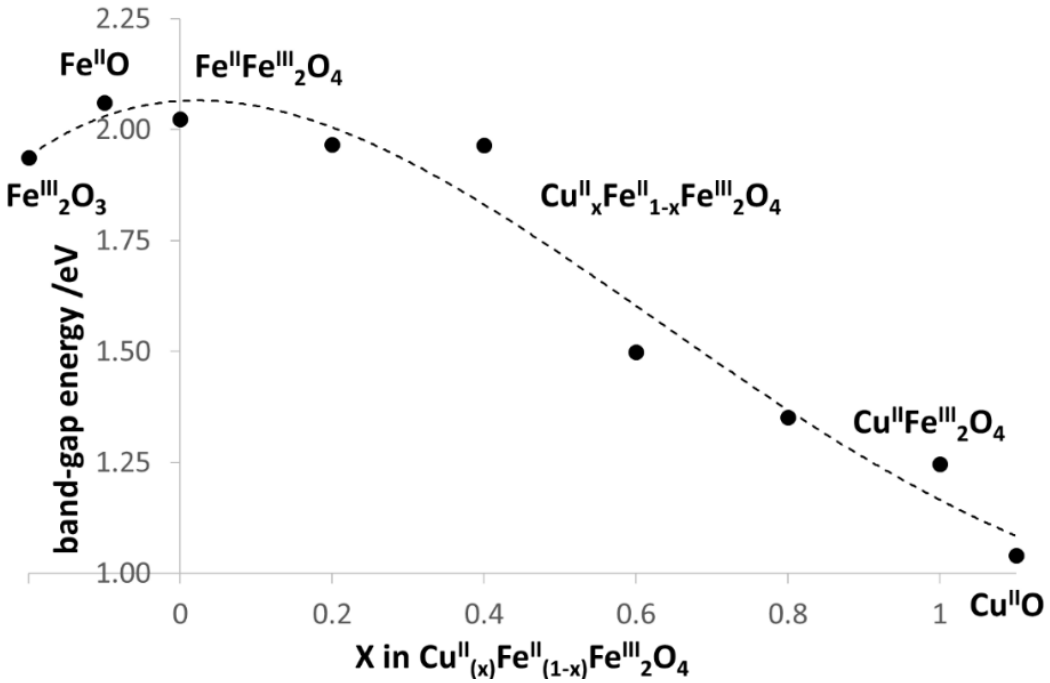

Figure 24. Band-gap energies (E_{bg}) of iron (II) doped copper ferrite NPs as the function of Cu^{2+}content for comparison to those of the simple metal oxides. The E_{bg} results of simple metal oxide NPs ($Cu^{II}O$, $Fe^{II}O$, and $Fe^{III}_2O_3$) are also added for comparison.

4.3 Evaluation of photocatalytic activity of $Cu^{II}_{(x)}Fe^{II}_{(1-x)}Fe^{III}_2O_4$ NPs for MB degradation

First of all, the potential self-degradation of MB with and without light (in dark) was checked (Table 5). In accordance with our results, earlier observations in the literature [159, 192] also confirmed that MB is stable in the dark, but photosensitive to visible light. The reaction rate for this photo-induced self-degradation of MB was determined in our work, compared to that of the photocatalytic reaction, in which H_2O_2 was used as an oxidant with the concentration of (0.01 M) suggested in similar experiments published in the literature [108]. The self-degradation of MB was ignored in subsequent studies. The presence of NP-3 significantly improved the reaction rate of MB degradation presented in terms of relative efficiency (Table 5), which is much higher as compared to control experiment (MB + H_2O_2 + Light). These reactions conditions were applied in similar studies.

Table 5. Control experiments for MB degradation. Concentrations: MB = 1.5×10^{-5} mol/L, NP-3 = 22.73 mg/L, H_2O_2 = 1.01×10^{-2} mol/L, temperature = 25±2 °C and irradiation time = 140 min.

Experiment	Reaction rate (M/s)	Relative degradation efficiency (%)
MB + NPs + Light	1.24×10^{-10}	41.8
MB + Light	1.13×10^{-10}	38.3
MB + H_2O_2	2.58×10^{-11}	8.7
MB + NPs + H_2O_2	4.37×10^{-11}	14.8
MB + H_2O_2 + Light	**2.95×10^{-10}**	**100 (control experiment used as basis for comparison)**
MB + NPs + H_2O_2 + Light	3.96×10^{-10}	133.9

Figure 25 shows the spectra change during the irradiation for the system containing NP-3 (x = 0.4). The decay at λ_{max}=665 nm (inset of Figure 25) suggests a pseudo-first-order kinetics. The logarithmic version of this plot (Figure 26) seems to confirm this expectation. However, its slight deviation from the linear function indicates the complex character of this heterogeneous process. Hence, the initial rates were used for the determination of the apparent rate constants.

Figure 27 reveals that in the range x = 0.2–0.8 the doped ferrite NPs showed higher rate constants as compared to the control experiment; while x = 0 (NP-1 magnetite), and x = 1 (NP-6 undoped copper ferrite) showed no remarkable change with respect to the control. The same trend was also reported in the literature for nickel doped cobalt ferrites NPs [108].

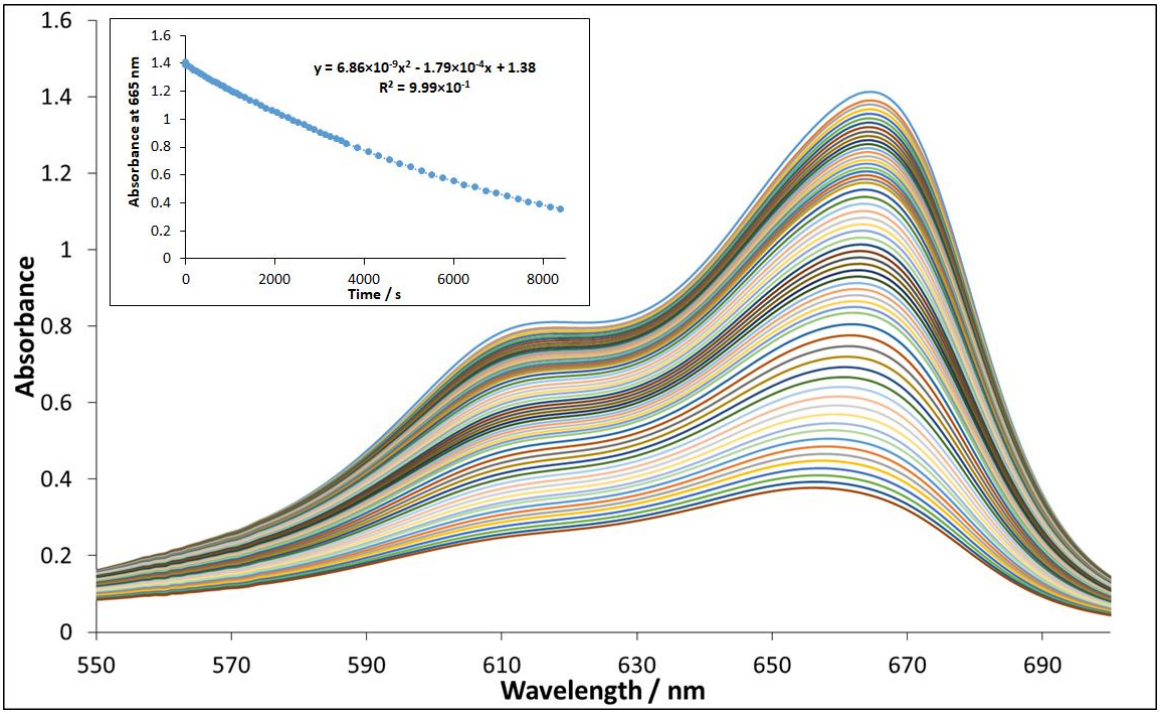

Figure 25. Spectral change during Methylene Blue degradation in photocatalytic system containing NP-3 (x = 0.4). The inset shows the absorbance vs. time plot at 665 nm. Concentrations: MB = 1.5 × 10^{-5} mol/L, NP-3 = 22.73 mg/L, initial pH = 7.5, H_2O_2 = 1.01 × 10^{-2} mol/L, temperature = 25±2 °C and irradiation time = 140 min.

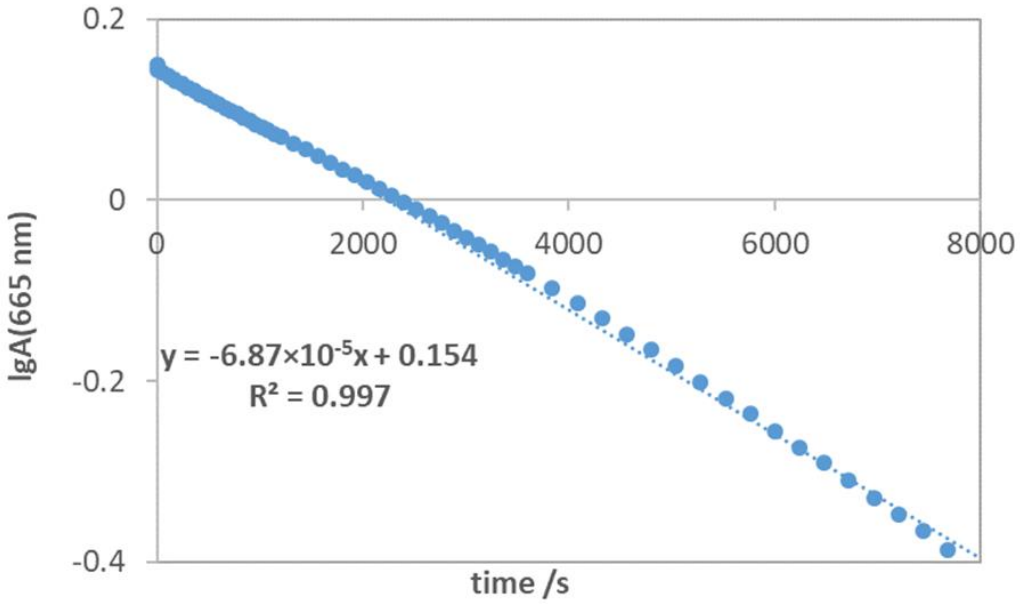

Figure 26. The logarithm of the absorbance at λ_{max}=665 nm vs. time plot for the degradation of MB (see the inset of Fig. 25).

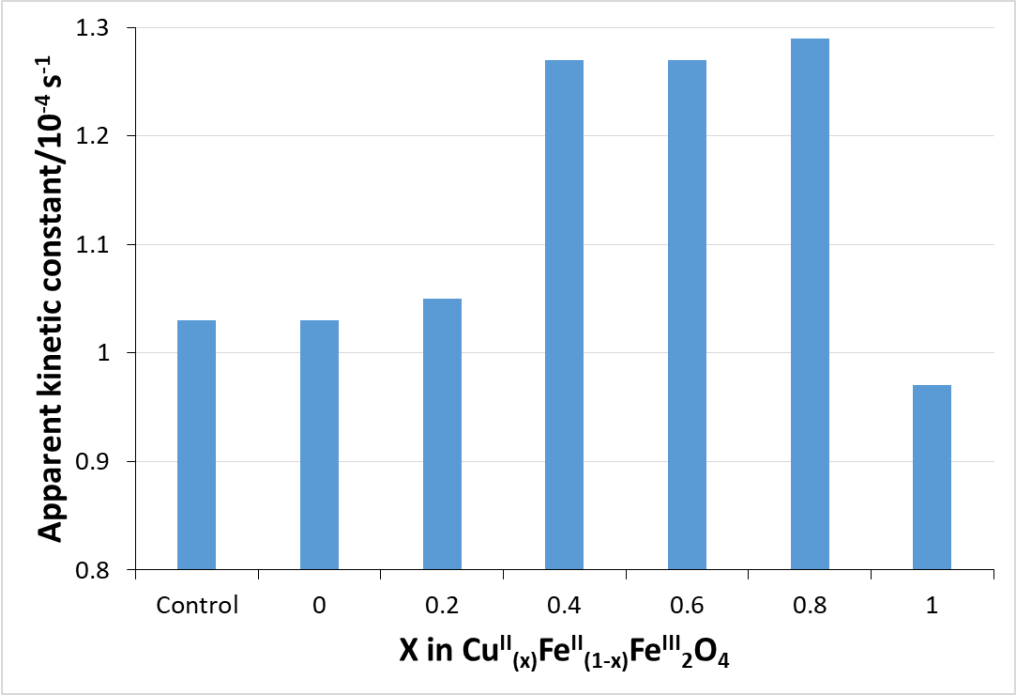

Figure 27. Photocatalytic efficiency in terms of apparent kinetic constant (compared to the control experiment) depending on the Cu^{2+}:Fe^{2+} ratio in $Cu^{II}_{(x)}Fe^{II}_{(1-x)}Fe^{III}_2O_4$. Concentrations were suggested by Singh *et al.* [108]: MB = 1.5×10^{-5} mol/L, NPs = 22.73 mg/L, initial pH = 7.5, H_2O_2 = 1.01×10^{-2} mol/L, temperature = 25±2 °C and irradiation time = 140 min.

This phenomenon may originate from the fruitful combination of the structures and catalytic features of the two separated metal ferrites at given ratios. The increase of Cu^{2+} and decrease of Fe^{2+} concentrations were observed to be useful to achieve higher photocatalytic performance. SEM images revealed that x = 0.2 (NP-2) and x = 0.4 (NP-3) had small needle-like crystals. A special crystalline structure may be a determining factors of higher catalytic efficiency. Based upon this first experimental series and SEM-EDS analysis, NP-3 was selected for the further investigation of three important parameters of our heterogeneous photo-Fenton system. Notably, the specific surface area of NP-3 is significantly lower than those of the catalysts consisting of larger needle-like crystals, indicating that this property is not crucial in the respect of their activity. Such an observation is not unusual regarding heterogeneous photocatalyst, in the case of which other (e.g., electronic or special morphologic) features are more determining.

4.3.1 Effect of $Cu^{II}_{0.4}Fe^{II}_{0.6}Fe^{III}_{2}O_4$ dosage on MB degradation

The NPs dosage was varied in the range of 0–800 mg/L as shown in Figure 28. It was observed that the increase in the NP-3 dosage from 0–400 mg/L showed a significant improvement in the reaction rate constant of MB degradation. This enhancement can be attributed to the higher number of active sites available for heterogeneous Fenton reactions and more photons absorbed by the catalyst particles [210]. Above 400 mg/L NPs concentration, the rate constants of degradation leveled off, due to the limited generation of hydroxyl radicals as a consequence of the increased turbidity of the reaction mixture, which could obstruct visible light irradiation [164]. Hence, the optimum dosage of 400 mg/L NPs was used for the further photocatalytic experiments [210].

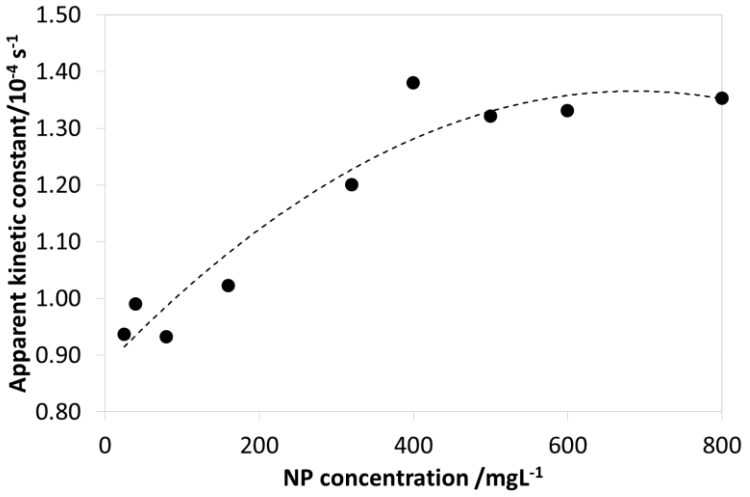

Figure 28. Effect of NP-3 (x = 0.4) concentration on the reaction rate constant of degradation. Concentrations: MB = 1.5 × 10^{-5} mol/L, conc. of H_2O_2 = 1.01 × 10^{-2} mol/L, initial pH = 7.5, temperature = 25±2 °C and irradiation time = 140 min.

4.3.2 Effect of H_2O_2 concentration on MB degradation

The effect of H_2O_2 on the photocatalytic degradation of MB without NPs is shown in Figure 29. The values of this initial rate vs. hydrogen peroxide concentration plot were taken as references for comparison with the corresponding values obtained in the presence of catalysts. As shown in Figure 30, the rate constant of degradation gradually increased upon enhancing the H_2O_2 concentration in the range of 0.01–0.18 M.

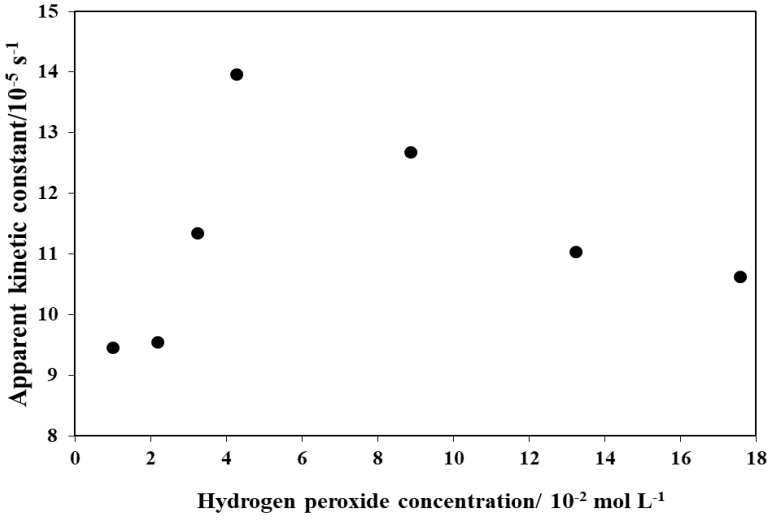

Figure 29. Effect of H_2O_2 concentration on the reaction rate constant of MB degradation in the absence of NP. Concentrations: MB = 1.5×10^{-5} mol/L, temperature = 25±2 °C and irradiation time = 140 min.

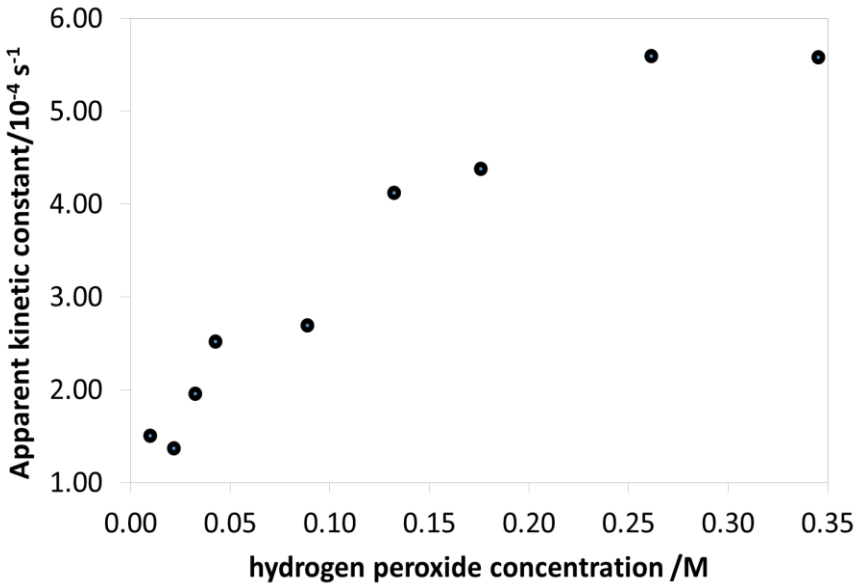

Figure 30. Effect of H_2O_2 concentration on the reaction rate constant of MB degradation. Concentrations: NP-3 = 400 mg/L, MB = 1.5×10^{-5} mol/L, initial pH = 7.5, temperature = 25±2 °C and irradiation time = 140 min.

It can be attributed to the production of higher amount of hydroxyl radicals at higher concentration of H_2O_2. The value of 0.2 mol/L used to be the upper limit for the concentration of H_2O_2 in the industrial applications because further increase resulted in scavenging effect on hydroxyl radicals [211]. Notably, our experiments in an extended concentration range indicated a maximum efficiency at 0.26 M. Nevertheless, 0.176 M H_2O_2 was used for the further experiments, not to exceed the 0.2 M limit.

4.3.3 Effect of pH on MB degradation

Interestingly, this heterogeneous photo-Fenton system was found to be more efficient at neutral and alkaline pH as compared to conventional Fenton systems, which used to work better at lower pH. The rate constants of extensively studied experiments were summarized in Figure 31. At pH < 3, the protonation of MB may cause the decrease of the reaction rate. Above pH 9, deprotonation of hydrogen peroxide takes place (pK_a = 11.75), resulting in the formation of the more reactive HO_2^- species. At much higher pHs, neither the irradiation (photo-Fenton), nor the presence of metal ions (Fenton) are necessary for the effective formation of $^{\bullet}OH$ radicals.

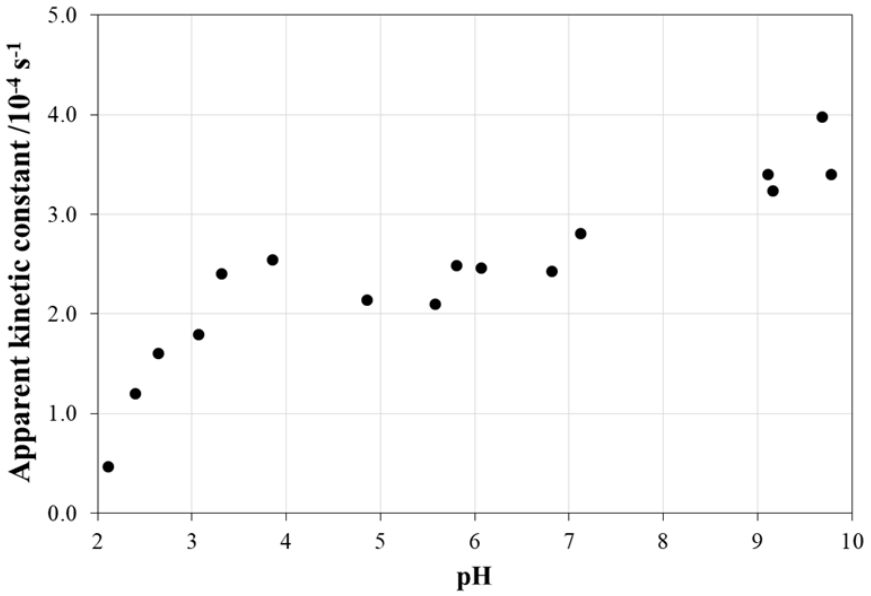

Figure 31. Effect of pH on the rate constant of MB degradation. Concentrations: NP-3 = 400 mg/L, conc. of MB = 1.5×10^{-5} mol/L, conc. of H_2O_2 = 1.76×10^{-1} mol/L, temperature = 25±2 °C and irradiation time = 140 min.

4.3.4 Summarizing the optimized photocatalytic conditions for MB

For the initial conditions of our experiments (Figures 25 and 27), we used the already published data in the literature, suggested by Singh *et al.* [108]. Then the potential effects of the reactants' concentration were revealed on the reaction rate of the photocatalytic degradation of methylene blue (Figures 28, 30 – 31). These optimized conditions differed from the initially used ones, therefore the quality of our NPs, that is, the Cu^{2+} ratio in $Cu^{II}_xFe^{II}_{1-x}Fe^{III}_2O_4$ was investigated again at these optimized concentrations (Figure 32) and compared with the control. The efficiencies in Figure 32 are much higher than those in Figure 27. Hence, our whole series of doped NPs are active photocatalysts for MB degradation and our optimized concentrations are more effective. At these new conditions, NP-2 (x = 0.2) and NP-3 (x = 0.4) proved to be the best photocatalysts under heterogeneous photo-Fenton system (Figure 32).

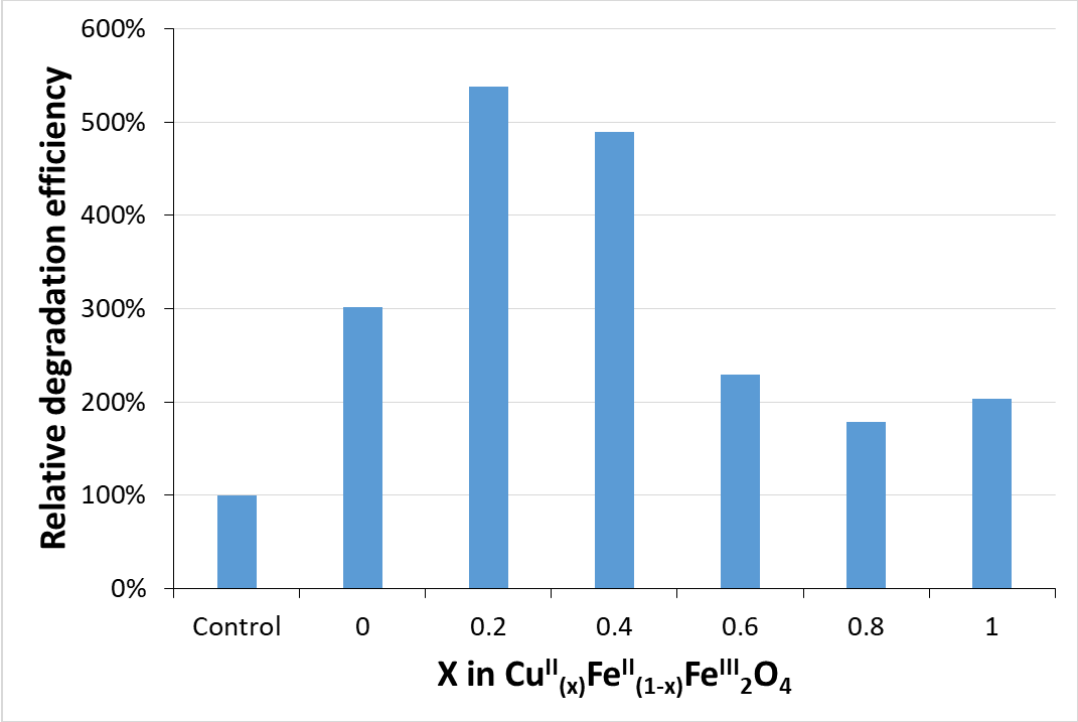

Figure 32. Relative degradation efficiency (compared to the photodegradation of MB without catalysts (control)) depending on the ratio Cu^{2+}:Fe^{2+} in $Cu^{II}_{(x)}Fe^{II}_{(1-x)}Fe^{III}_{2}O_4$ at the optimized concentrations: MB = 1.5×10^{-5} mol/L, NPs = 400 mg/L, initial pH = 7.5, H_2O_2 = 1.76×10^{-1} mol/L, temperature = 25±2 °C and irradiation time = 140 min.

Although, according to the literature, 400 °C was used as the calcination temperature in the syntheses of the several catalysts, after determination of the optimized application conditions for NP-3, a preliminary series of experiments regarding the effect of the calcination temperature on the activity of NP-3 was also carried out. The results indicated that above 250 °C (Figure 33) the activity just slightly depends on the calcination temperature, and the maximum is about 300 °C.

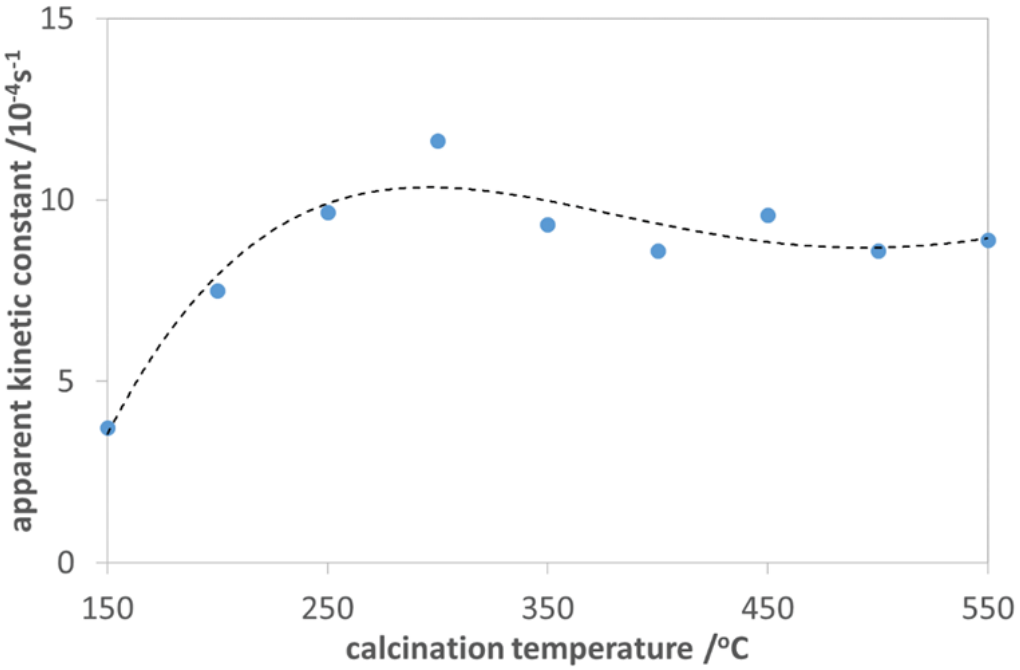

Figure 33. Effect of the calcination temperature of the NP-3 (x=0.4) catalyst on the apparent kinetic constant of MB degradation. Concentrations: NP-3 = 400 mg/L, MB = 1.5×10^{-5} mol/L, conc. of H_2O_2 = 1.76×10^{-1} mol/L, and irradiation time = 140 min.

4.3.5 MB degradation mechanism

The possible mechanism for the formation of the reactive oxygen species in the presence of $Cu^{II}_{(x)}Fe^{II}_{(1-x)}Fe^{III}_2O_4$ NPs can be expressed as given below (Equations (23)–(28)). When a photon having energy *(hv)* equal to or higher than the band gap of the semiconductor photocatalyst is absorbed, an electron is promoted from the filled valence band of the semiconductor material into the vacant conduction band, creating a hole (h^+) in the valence band. This production of electron hole pair (e^--h^+) promotes further reactions in the photocatalytic system.

$$Fe(II) + H_2O_2 \rightarrow Fe(III) + {}^{\bullet}OH + OH^- \quad (23)$$

$$Fe(III) + H_2O_2 \rightarrow Fe(II) + {}^{\bullet}OOH + H^+ \quad (24)$$

$$H_2O_2 + e^- \rightarrow {}^{\bullet}OH + OH^- \quad (25)$$

$$H_2O + h^+ \rightarrow H^+ + {}^{\bullet}OH. \quad (26)$$

Ionization of water under photocatalytic system:

$$H_2O \rightarrow OH^- + H^+ \quad (27)$$

$$OH^- + h^+ \rightarrow {}^{\bullet}OH. \quad (28)$$

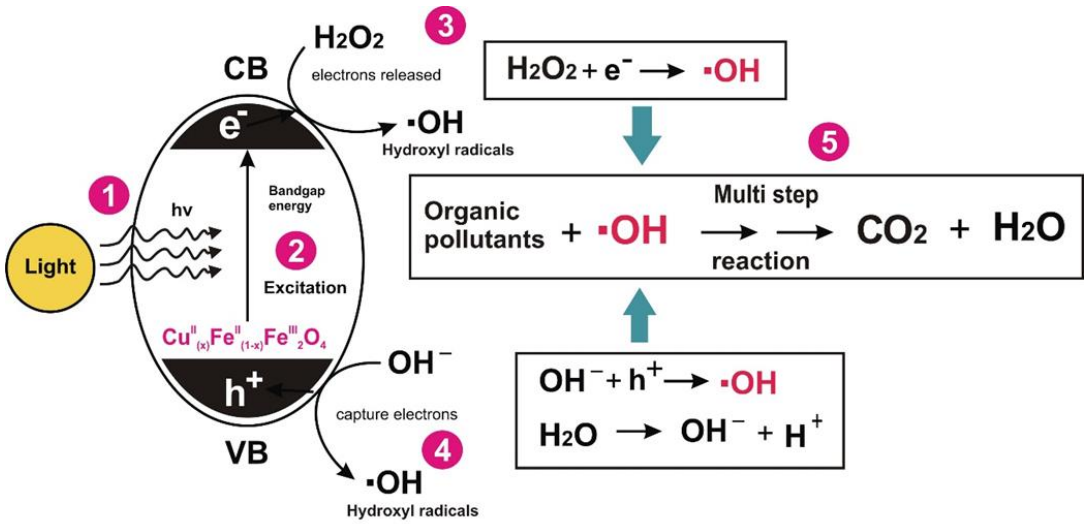

Figure 34. Schematic diagram for the degradation mechanism of organic pollutants in heterogeneous photo-Fenton system.

The possible mechanism of the degradation of organic pollutants in $Cu^{II}_{(x)}Fe^{II}_{(1-x)}Fe^{III}_2O_4$ based pollutants in heterogeneous photo-Fenton system is shown in Figure 34.

The above claim was further confirmed by the UV-visible spectra of MB obtained before and after photo-Fenton degradation of MB at optimized conditions (Figure 35). MB contains three characteristic peaks at 665, 612 and 292 nm as shown in UV-visible spectrum. In some cases MB can be reduced to leuco-methylene blue (λ_{max} = 256, 322 nm) [175] and MBH_2^+ (λ_{max} = 232 nm) [175, 212] which are colourless and stable in aqueous medium. Thus, in this photocatalytic system using NP-3 (doped copper ferrite) as catalyst, we observed that MB was totally degraded during the 140 min irradiation, showing no peaks in ultraviolet and visible range. The photo-reactor images obtained before (Figure 36A) and after (Figure 36B) photocatalysis also confirmed the complete removal of MB resulting in clear solution after the removal of solid catalysts (Figure 36C).

For further confirmation, TOC measurements were performed during MB photodegradation at optimized conditions. It was observed that during first hour of MB photocatalysis around 60% of TOC was removed (Figure 37). However, no further

decrease in TOC values was observed with increase in photocatalysis time. Hence, it was concluded that MB has been degraded to smaller weight products having no peaks in UV and visible region of spectrum.

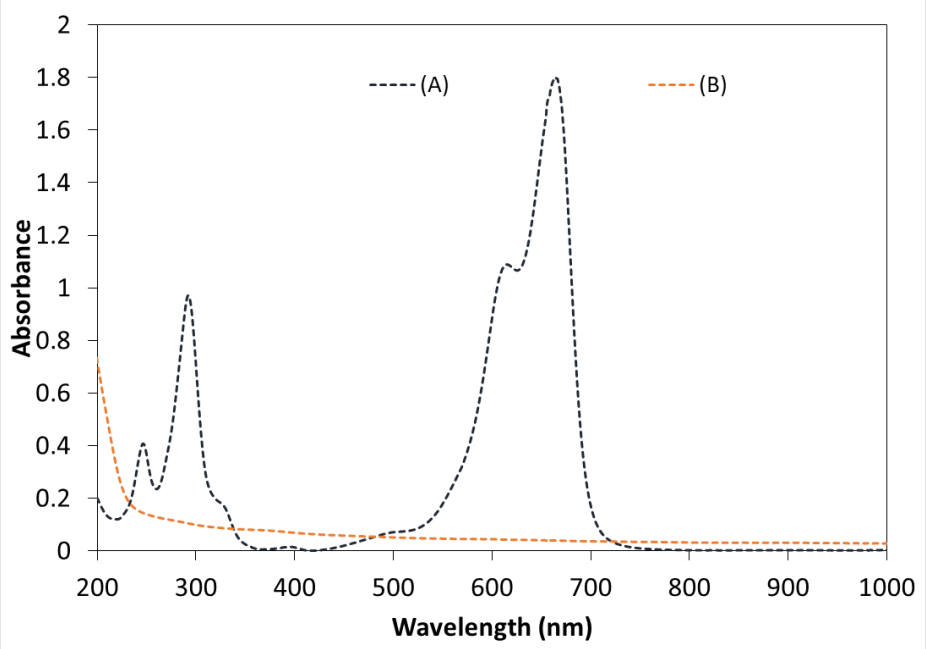

Figure 35. (A) Methylene blue spectrum, (B) UV/visible spectrum obtained after MB degradation using NP-3 ($Cu^{II}_{0.4}Fe^{II}_{0.6}Fe^{III}_{2}O_4$), Concentrations: MB = 1.5×10^{-5} mol/L, NPs = 400 mg/L, initial pH = 7.5, H_2O_2 = 1.76×10^{-1} mol/L, temperature = 25±2 °C, and time = 140 min.

Figure 36. Visual representation of MB before and after photo-Fenton degradation in the photo-reactor (cuvette). (A) Mixture of MB + NP-3 before photocatalysis, (B) MB + NP-3 after photocatalysis and (C) clear solution obtained after separation of solid catalyst from (B).

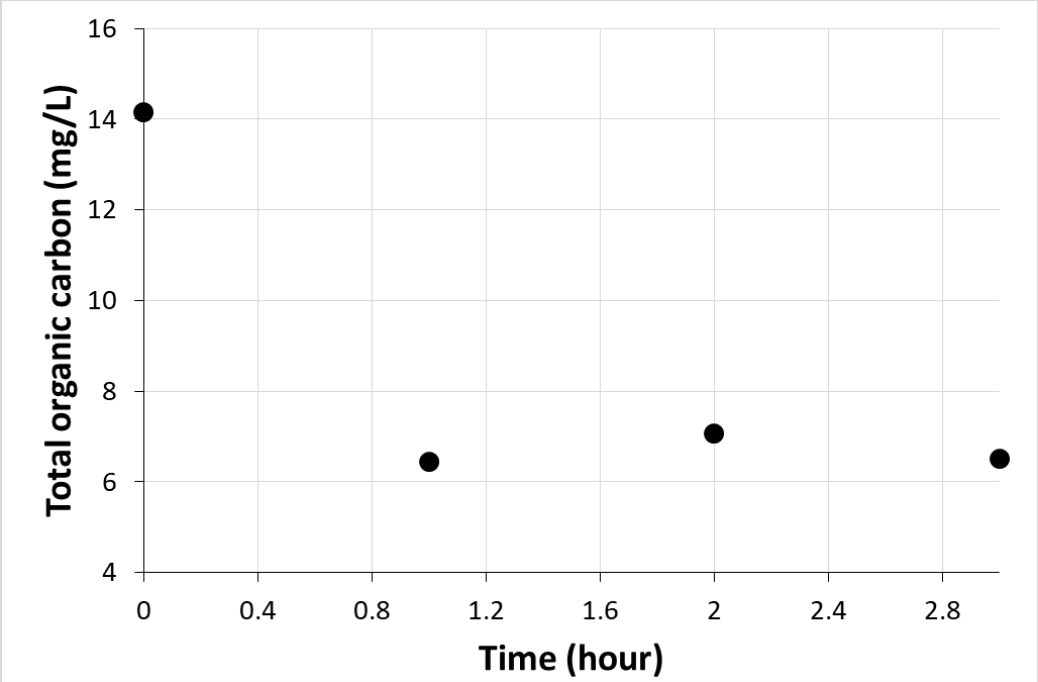

Figure 37. Measurements of total organic carbon (TOC) during MB photocatalysis at optimized conditions

4.4 Evaluation of Photocatalytic Activity of $Cu^{II}_{(x)}Fe^{II}_{(1-x)}Fe^{III}_2O_4$ NPs for RhB degradation

In step I, the potential self-degradation of RhB in light was checked (Table 6). In the next experiment for RhB degradation, we used H_2O_2 as oxidant reagent (step II) in the concentration (0.176 M) optimized in our MB experiments (see Section 4.3.4). Subsequently, the combined effect of RhB + NP-3 + H_2O_2 (step III) were studied. Then RhB degradation was checked in the presence of light and H_2O_2 and this experiment was used as base for comparing results (step IV). After that the effect of presence of nanoparticles (e.g. NP-3) was checked, as heterogeneous photocatalyst. It was observed that NPs in the reaction (RhB + NPs + H_2O_2 + Light) have significantly improved the reaction rate of RhB degradation which can be seen from the higher relative degradation efficiency (346%) in comparison to other control experiments (step V).

Table 6. Control experiments for RhB degradation. Concentrations: RhB = 1.75×10^{-5} mol/L, NP-3 = 400 mg/L, H_2O_2 = 1.76×10^{-1} mol/L, pH = 7.5, temperature = 25±2 ℃, and irradiation time = 140 min.

Step No	Experiment	Reaction rate (M/sec)	Relative degradation efficiency (%)
I	RhB + Light	9.77×10^{-11}	41
II	RhB + H_2O_2	1.70×10^{-10}	69
III	RhB + H_2O_2 + NPs	1.90×10^{-10}	55
IV	**RhB + H_2O_2 + Light**	**3.26×10^{-10}**	**100 (control experiment used as a basis for comparison)**
V	RhB + NPs + H_2O_2 + Light	6.06×10^{-9}	346

After the control experiments, the efficiency of six doped ferrites nanoparticles were investigated. Figure 38 shows the detailed spectra obtained during photocatalytic degradation experiment and the decrease in the absorbance of RhB at λ_{max}=554 nm (inset of Figure 38) using NP-3. The experimental data are well fitted to the regression line which can be observed from R^2 value 0.998 (inset Figure 38). The decay at 554 nm (inset of Figure 38) suggests a pseudo-first-order kinetics, which was confirmed by the logarithmic version of this plot (Figure 39).

Figure 40 revealed that all doped ferrite NPs in the series $Cu^{II}_{(x)}Fe^{II}_{(1-x)}Fe^{III}_2O_4$ (x = 0.0-1.0) delivered higher apparent kinetic constant values in the RhB degradation as compared to the control experiment; while NP-2 and NP-3 showed outstanding photocatalytic performance in this heterogeneous photo-Fenton type system. The increase in Cu^{2+} and decrease in Fe^{2+} concentrations was observed to be useful in getting higher photocatalytic performance. In addition, all types of doped copper ferrites $Cu^{II}_{(x)}Fe^{II}_{(1-x)}Fe^{III}_2O_4$ in the range of x=0.0-1.0 are effective catalysts in the case of RhB. The higher apparent kinetic constant values obtained using NP-2 and NP-3 may be attributed to the small needle like crystalline structure together with larger specific surface area. On the basis of this first experimental series, NP-3 (x=0.4) was selected for the further investigation of three important determinants such as catalyst dosage, hydrogen peroxide concentration and pH of heterogeneous photo-Fenton system.

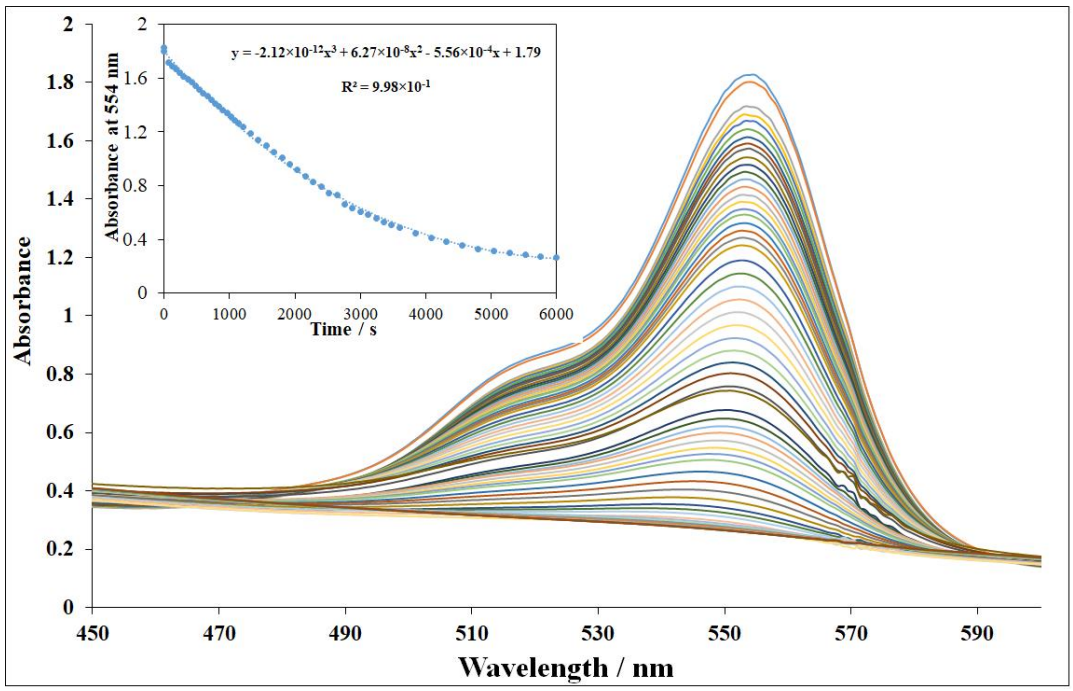

Figure 38. Spectral change during Rhodamine B degradation in photocatalytic system containing NP-3 (x = 0.4). The inset shows the absorbance vs. time plot at λ_{max}=554 nm. Concentrations: RhB = 1.75×10^{-5} mol/L, NP-3 = 400 mg/L, initial pH = 7.5, H_2O_2 = 1.76×10^{-1} mol/L, temperature = 25±2 °C and irradiation time =140 min.

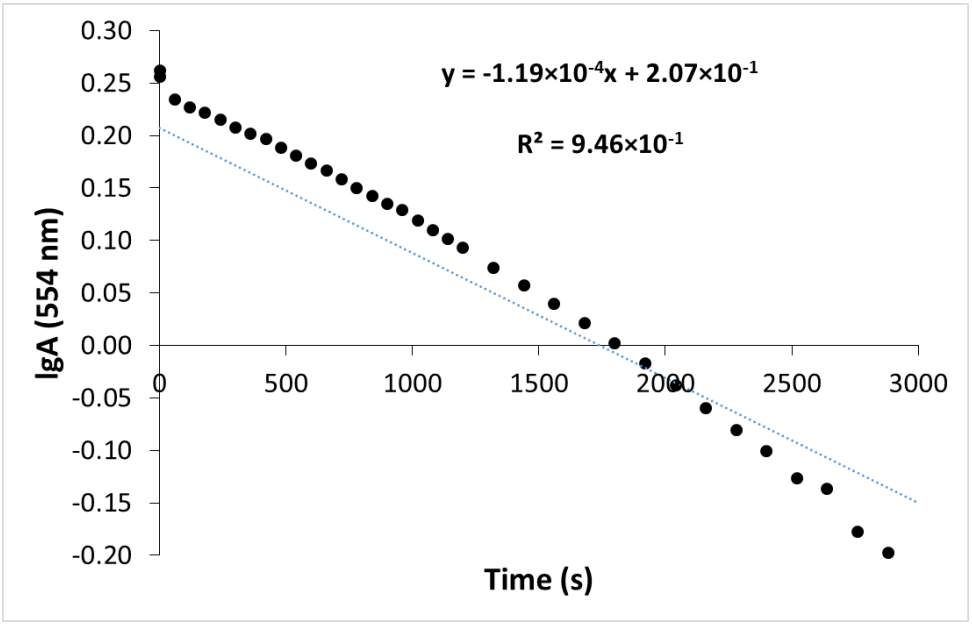

Figure 39. The logarithm of the absorbance at λ_{max}=554 nm vs. time plot for the degradation of RhB (see the inset of Fig. 38).

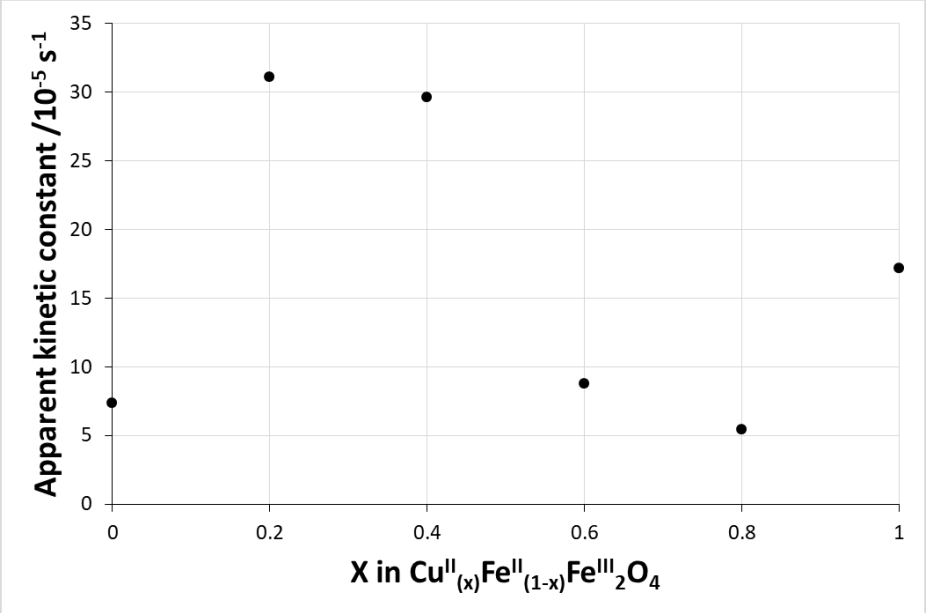

Figure 40. Photocatalytic efficiency depending on the ratio Cu^{2+}:Fe^{2+} in $Cu^{II}_{(x)}Fe^{II}_{(1-x)}Fe^{III}_2O_4$. Concentrations: RhB = 1.75×10^{-5} mol/L, NPs = 400 mg/L, initial pH = 7.5, temperature = 25±2 °C, irradiation time = 140 min, and H_2O_2 = 1.76×10^{-1} mol/L

4.4.1 Effect of catalyst dosage

The NPs dosage was varied in the range of 0–800 mg/L as shown in Figure 41. It was observed that an increase in the NP-3 dosage from 0–500 mg/L showed significant improvement in the rate constant of degradation of RhB. This enhancement in the degradation efficiency can be attributed to the higher number of available active sites for heterogeneous photo-Fenton system [213]. However, increasing the NPs dosage above 500 mg/L delivered slight decrease in the rate constant of degradation, similarly to the degradation of MB. As I described in the subchapter 4.3.1. Effect of $Cu^{II}_{0.4}Fe^{II}_{0.6}Fe^{III}_2O_4$ dosage on MB degradation, this decrease may be attributed to the limited generation of hydroxyl radicals at higher NPs concentration. Also, higher NPs concentration can increase the reaction turbidity which would obstruct visible light irradiation [214]. Hence, the optimum dosage of 500 mg/L NPs was used for the further photocatalytic reactions of RhB.

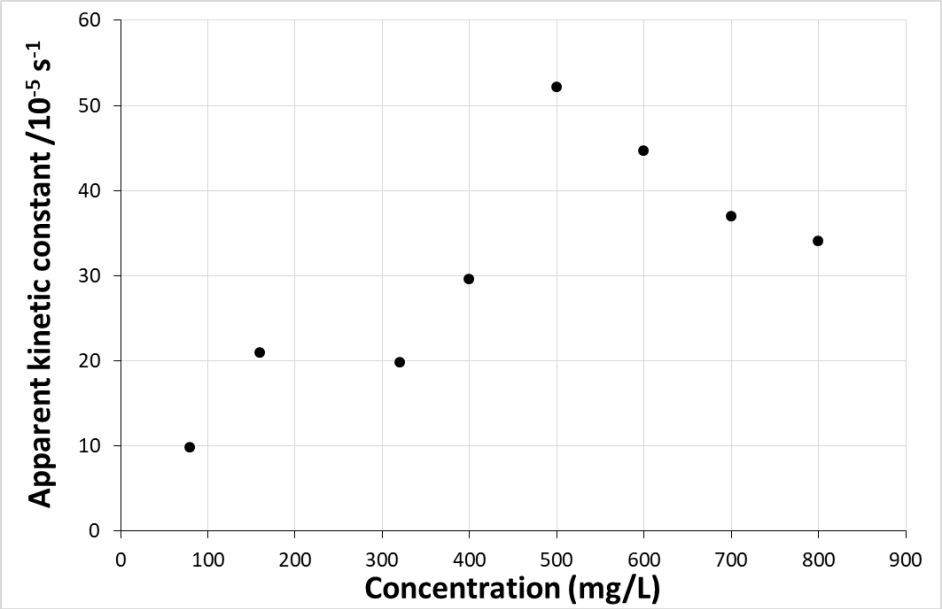

Figure 41. Effect of NP-3 ($Cu^{II}_{(0.4)}Fe^{II}_{(0.6)}Fe^{III}_2O_4$) concentration on the RhB degradation. Concentrations: RhB = 1.75×10^{-5} mol/L, conc. of H_2O_2 = 1.76×10^{-1} mol/L, irradiation time = 140 min, temperature = 25±2 °C, and initial pH = 7.5.

4.4.2 Effect of hydrogen peroxide concentration

At first, the effect of H_2O_2 concentration on the photocatalytic degradation of RhB without NPs was investigated as shown in Figure 42. The concentration of H_2O_2 was increased from 4.46×10^{-2} mol/L to 6.67×10^{-1} mol/L. The apparent kinetic constant values indicate that the reaction rate was enhanced by increasing H_2O_2 up to 3.45×10^{-1} mol/L. However, after this point a slight decrease in the apparent kinetic constant was observed. The excess amount of H_2O_2 could act as $^{\bullet}OH$ scavenger producing less reactive $HO_2^{\bullet}$ instead of $^{\bullet}OH$ [213-215].

The second experimental series was focused on checking the effect of increase in H_2O_2 concentration from 2.19×10^{-2} to 3.04×10^{-1} mol/L in the presence of NPs (Figure 43). A significant improvement in the reaction apparent constant and relative rate of degradation was observed with increase in the H_2O_2 concentration up to 8.88×10^{-2} mol/L. Further increase in H_2O_2 was not helpful in enhancing the reaction rate significantly, and the same phenomenon was reported earlier [215, 216]. Thus, H_2O_2 concentration 8.88×10^{-2} mol/L was used as optimum in further photocatalytic experiments of RhB for better results and cost-effectiveness. In addition, it was confirmed that NPs have significantly enhanced the reaction rate in terms of apparent kinetic constant.

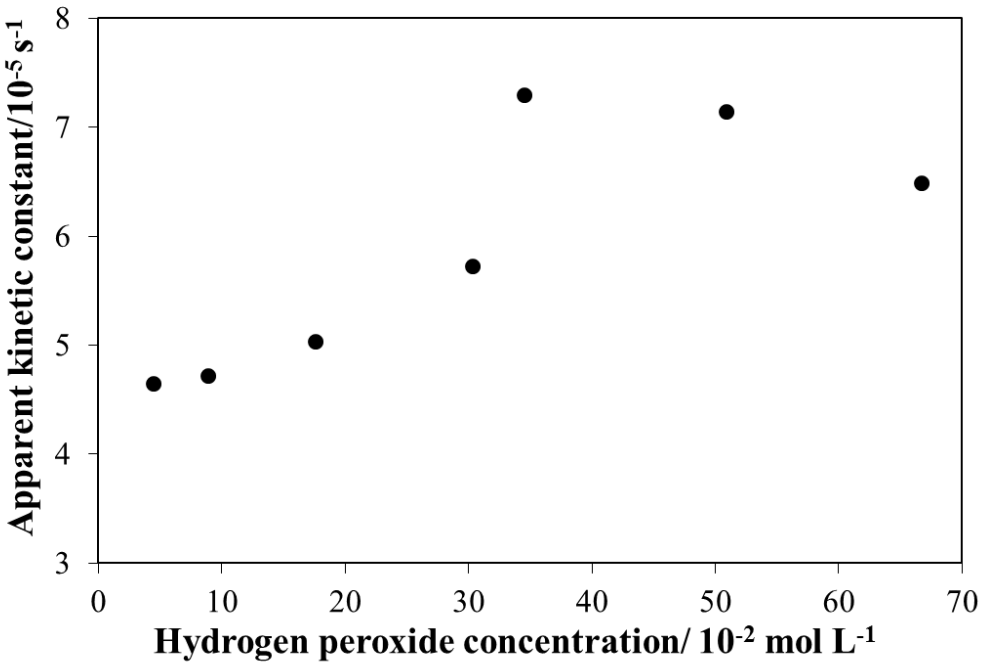

Figure 42. Effect of H_2O_2 concentration on the RhB degradation in the absence of NPs. Concentrations: RhB = 1.75×10^{-5} mol/L, irradiation time = 140 min, temperature = 25±2 °C, and initial pH = 7.5.

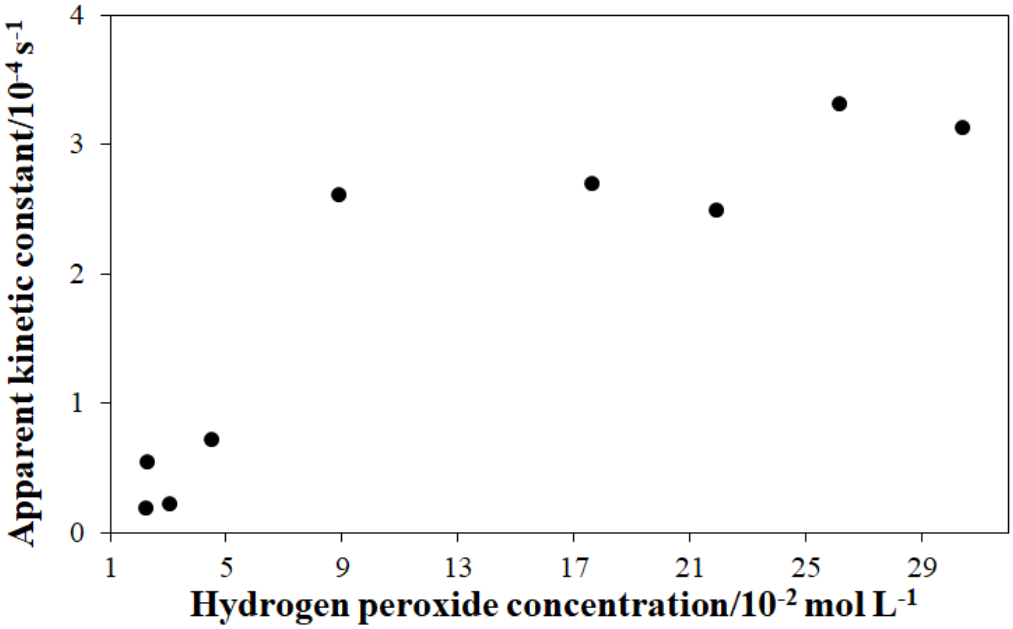

Figure 43. Effect of H_2O_2 concentration on the RhB degradation in the presence of NPs. Concentrations: RhB = 1.75×10^{-5} mol/L, NP-3 = 500 mg/L, irradiation time = 140 min, temperature = 25±2 °C, and initial pH = 7.5.

4.4.3 Effect of pH

The surface-charge-properties of the photocatalyst and the ionic species present in the photocatalytic reactor are greatly influenced by the pH. Also, the photodegradation efficiency of the dye is affected by the ionic species and the surface-charges of photocatalyst in the solution. For this purpose, two experimental series were designed to study the effect of pH on visible-light induced degradation of RhB. In the first series, pH was varied from 3.8 – 12.1 using constant concentrations of RhB and H_2O_2 in the absence of NPs developing a homogeneous system. Remarkably, neutral and alkaline pHs were found to be more effective in this system for RhB degradation (Figure 44).

In addition, the presence and absence of H_2O_2 were also investigated at higher pH values (around pH 12), which can be seen from the last two points in Figure 44. It was observed that hydrogen peroxide was able to produce more reactive species (HO_2^-) at higher pH value (pK_a = 11.75) due to deprotonating effect, promoting faster RhB degradation.

On the basis of Figure 44, we have determined the individual (apparent) kinetic constants (at these conditions) for the differently protonated forms of peroxide: 1.9×10^{-5} s^{-1} for H_2O_2 and 6.2×10^{-4} s^{-1} for HO_2^-. Deprotonation results in a 32-times increase of the degradation effect.

Moreover, the effect of pH in the presence of NPs (Figure 45) revealed that neutral or near alkaline pH could be applied as optimum during this type of reactions. The best apparent kinetic constant was observed at pH 7.8. However, further increase in pH resulted in a slight decrease of the reaction rate. Soltani *et al.* [176] reported that in the bismuth ferrites photocatalysis the pH can alter the charge state of RhB in reaction mixture. Also, at high pH values, RhB aggregates as a result of the excessive concentration of OH^- ions, which can compete with COO^- in binding with $–N^+$. Besides, the surface of the solid bismuth ferrite catalyst is negatively charged, which repels the RhB due to presence of ionic COO^- groups in basic conditions. Thus, the degradation efficiency is decreased on the surface of photocatalyst [176]. Similar phenomenon was observed in our case, using doped copper ferrites. On the basis of Figures 44 and 45, we were able to identify the partly hydroxylated forms of metal ions ($[Fe^{III}(OH)_2]^+$, $[Cu^{II}(OH)]^+$) for this local maximum of

Figure 45 at about pH=7.8. This means that the partly hydroxylated metal ions can react with H_2O_2, resulting in the ~14-times increase of the apparent kinetic constant (2.7×10^{-4} s^{-1} compared to 1.9×10^{-5} s^{-1} for H_2O_2 without NPs).

In addition, the effect of light, hydrogen peroxide, NPs at approximately constant pH is illustrated in Table 7. Photo-induced RhB degradation at pH 12.1, in the absence of hydrogen peroxide and NP-3 revealed a very low reaction rate (step 1). In step 2, hydrogen peroxide was added in the absence of light and NP-3 at pH 11.9 delivered a faster reaction rate. Step 3 representing a heterogeneous Fenton system resulted in a much faster reaction rate. A photo-induced heterogeneous Fenton system shown in step 4, revealed the best reaction rate for RhB.

It was confirmed that the catalyst $Cu^{II}_{(0.4)}Fe^{II}_{(0.6)}Fe^{III}_2O_4$ can overcome the disadvantage of a narrow pH range of conventional photo-Fenton process. Based on these experimental series, the $Cu^{II}_{(0.4)}Fe^{II}_{(0.6)}Fe^{III}_2O_4$ catalyst can be applied as a promising candidate for the degradation of various recalcitrant dyes under a wide pH range.

Table 7. Comparison of reaction rate during RhB degradation at pH around 12 under different experimental conditions

Step No	**Light**	**Hydrogen peroxide (mol/L)**	**NP-3 (mg/L)**	**pH initial (adding 15 µL 1M NaOH)**	**pH final**	**Apparent kinetic constant (1/s)**	**Comparison with basis reaction (%)**
1	visible	0	0	12.1	11.7	2.64×10^{-6}	12
2	no	8.88×10^{-2}	0	11.9	11.0	1.62×10^{-4}	749
3	no	8.88×10^{-2}	500	11.9	11.3	2.72×10^{-4}	1256
4	visible	8.88×10^{-2}	500	11.9	11.2	3.55×10^{-4}	1642

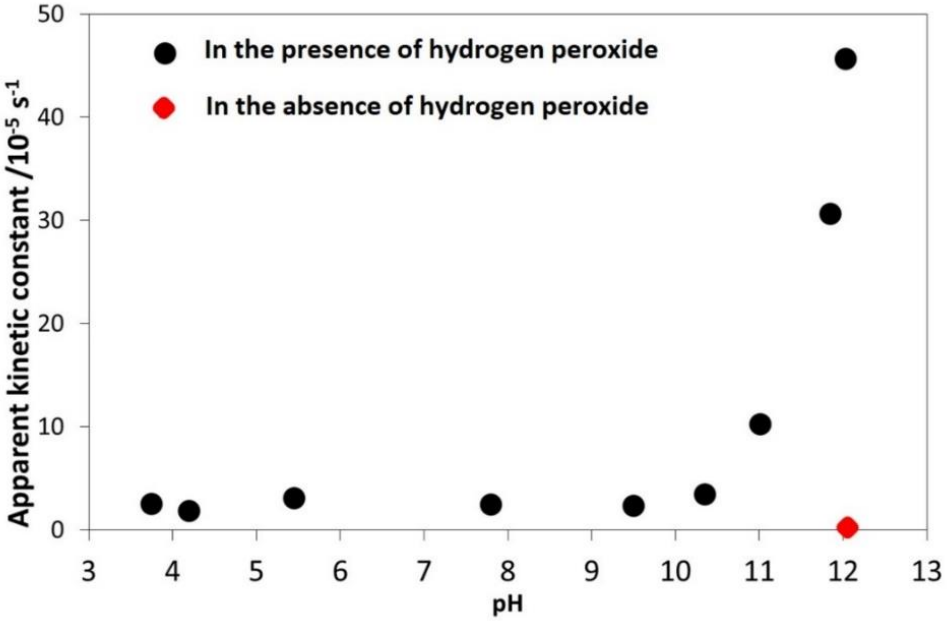

Figure 44. Effect of initial pH on the apparent kinetic constant of RhB degradation in the absence of NPs. Concentrations: conc. of RhB = 1.75×10^{-5} mol/L, irradiation time = 140 min, and conc. of H_2O_2 = 8.88×10^{-2} mol/L

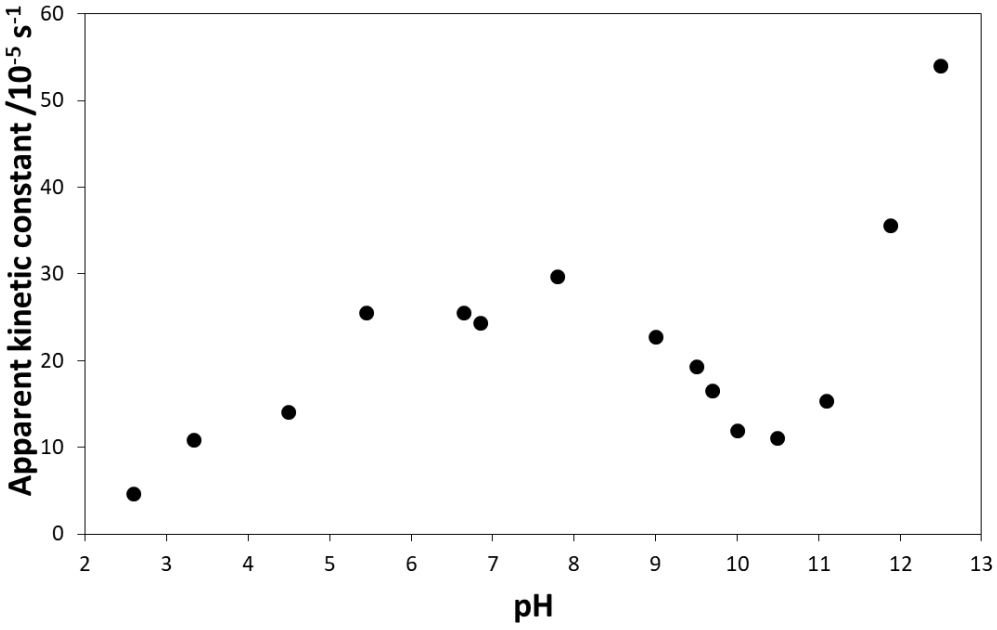

Figure 45. Effect of pH on the apparent kinetic constant of RhB degradation in the presence of NPs. Concentrations: NP-3 = 500 mg/L, conc. of RhB = 1.75×10^{-5} mol/L, temperature = 25±2 °C, irradiation time = 140 min, and conc. of H_2O_2 = 8.88×10^{-2} mol/L

4.4.4 Summarizing the optimized conditions for RhB degradation

Finally, the photocatalytic performance of all six iron (II) doped copper ferrites NPs (NP-1 to NP-6) were investigated at optimized conditions (Figure 46) and compared with control. It was observed that all NPs were active photocatalysts and NP-3 among them delivered the highest relative degradation efficiency (1331%) followed by NP-2 (950%). Thus, all NPs in the series can be potentially applied in environmental remediation of organic compounds.

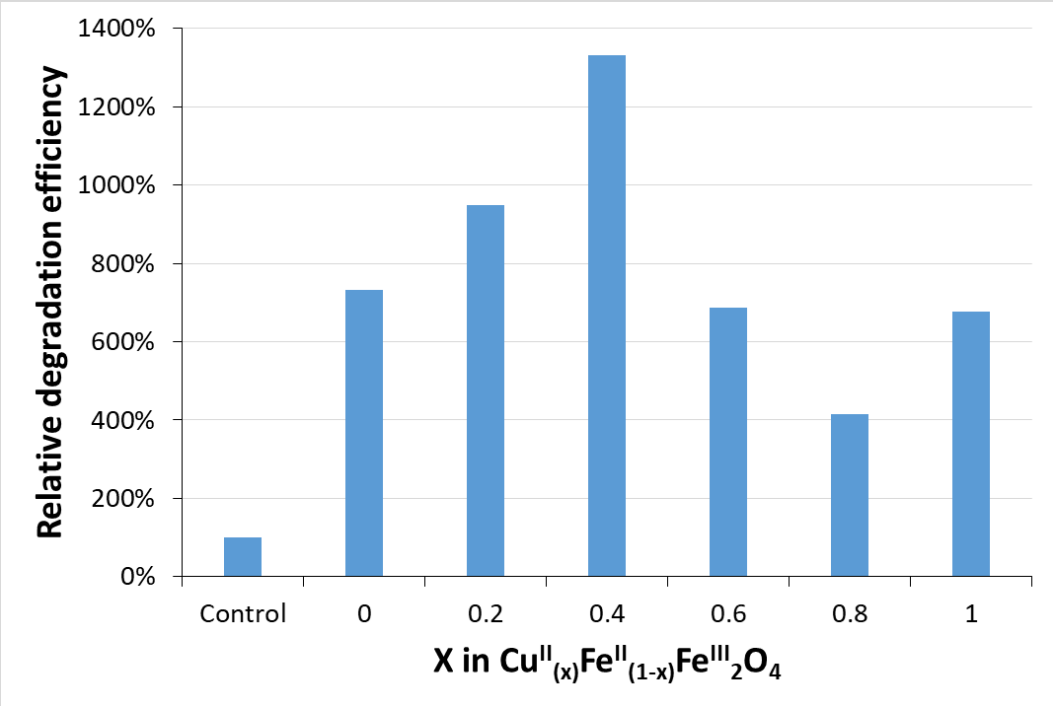

Figure 46. Relative degradation efficiency (compared to the photodegradation of RhB without catalysts (control)), depending on the ratio Cu^{2+}:Fe^{2+} in $Cu^{II}_{(x)}Fe^{II}_{(1-x)}Fe^{III}_{2}O_4$ at the optimized conditions; concentrations: RhB = 1.75×10^{-5} mol/L, NPs = 500 mg/L, initial pH = 7.5, irradiation time = 140 min, temperature = 25±2 °C, and $H_2O_2 = 8.88\times10^{-2}$ mol/L.

4.4.5 Degradation mechanism for RhB

A very simple schematic mechanism is proposed for RhB degradation which can be explained with reference to the fact that the production of reactive species during photolysis, namely, $^{\bullet}OH$, h^+, and $^{\bullet}O_2^-$, oxidize RhB molecules to intermediates having lower molecular weight. In general, the active species attack the central carbon atom in RhB chemical structure. Then the active species attack the intermediates produced in the previous step, producing smaller open ring compounds. Subsequently, the smaller ring

compounds are mineralized to water and carbon dioxide [175] (Figure 47). It can be observed from UV/visible spectra (Figure 48A) that RhB have prominent peaks at 554, 262 and 358 nm. After photocatalysis (Figure 48B) no significant peaks were observed either in visible or in UV region which confirmed the complete mineralization of RhB. The photo-reactor images obtained before (Figure 49A) and after (Figure 49B) photocatalysis also confirmed the complete removal of RhB resulting in clear solution after the removal of solid catalysts (Figure 49C) by using centrifugal filtration technique.

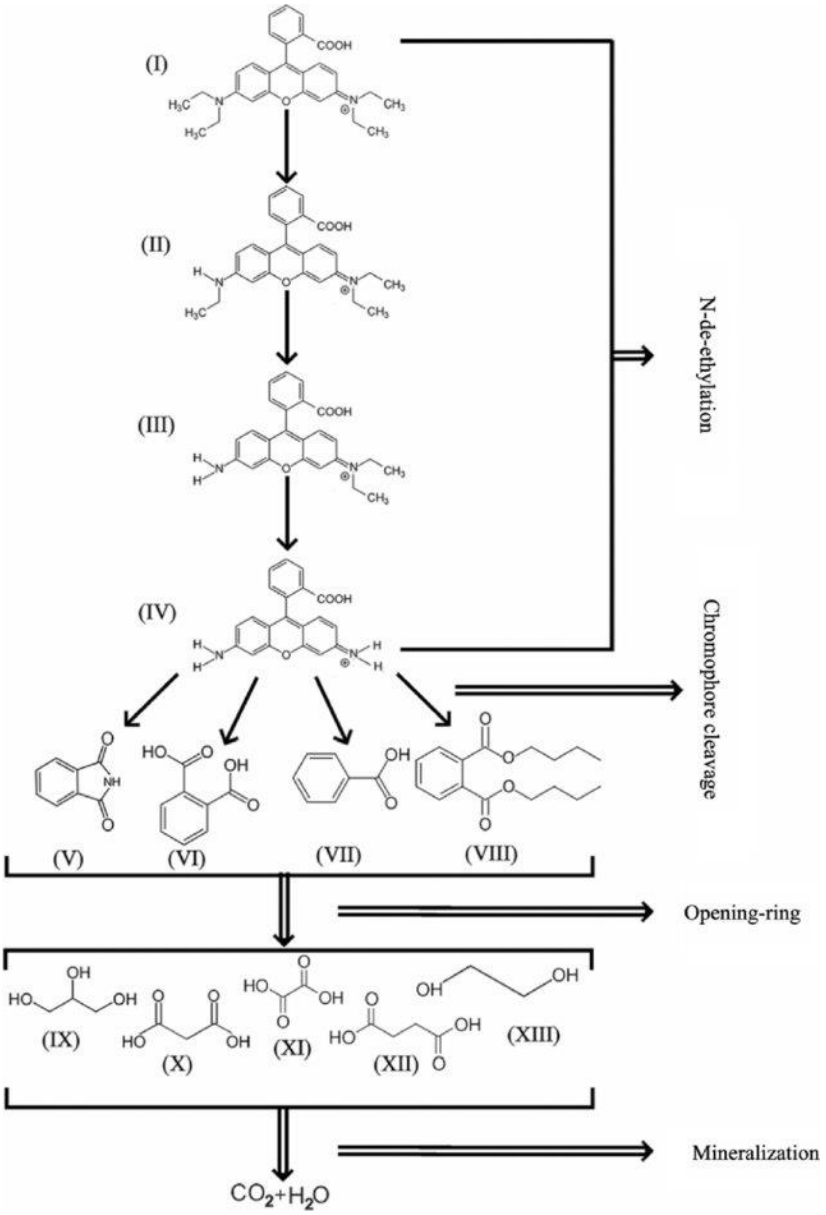

Figure 47. Rhodamine B degradation reaction proposed pathways, using iron (II) doped copper ferrites under visible light irradiation [217].

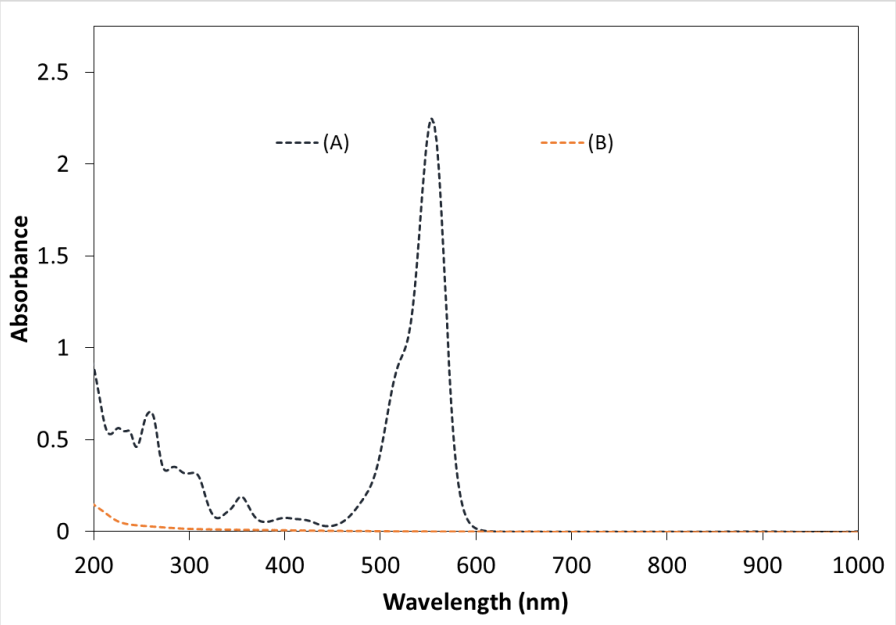

Figure 48. (A) Rhodamine B spectrum, (B) UV/visible spectrum obtained after RhB degradation using NP-3 ($Cu^{II}_{0.4}Fe^{II}_{0.6}Fe^{III}_2O_4$), Concentrations: NPs = 500 mg/L, H_2O_2 = 8.88×10^{-2} mol/L, RhB = 1.75×10^{-5} mol/L, initial pH = 7.5, temperature = 25±2 °C, and irradiation time = 140 min.

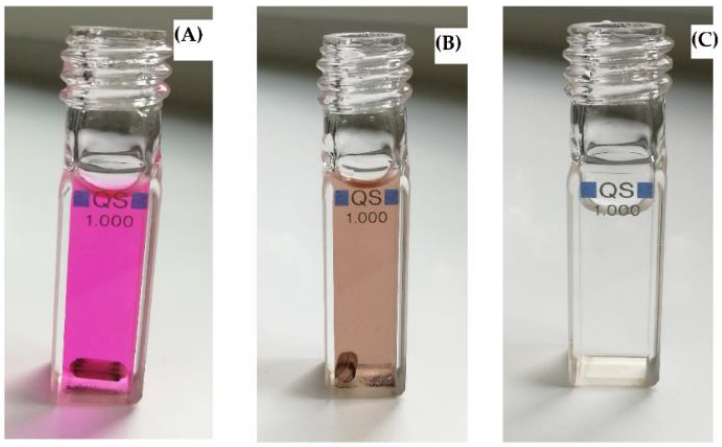

Figure 49. Visual representation of RhB before and after photo-Fenton degradation in the photo-reactor (cuvette). (A) Mixture of RhB + NP-3 before photocatalysis, (B) RhB + NP-3 after photocatalysis and (C) clear solution obtained after separation of solid catalyst from (B).

4.5 Comparison of the photocatalytic performance of simple metal oxides, doped (NP-3) and metal oxides composite

In this experimental series, the photocatalytic performance of synthesized metal oxides, iron(II) doped copper ferrite (NP-3) and the composite of simple metal oxides (in the same ratio $Cu^{II}O/Fe^{II}O/Fe^{III}_2O_3$) were compared by using MB (Figure 50). NP-3

exhibited the highest degradation efficiency, followed by metal oxides composite. The best degradation efficiency of NP-3 using MB; may originate from the fruitful combination of the structures and catalytic features of the two metal ferrites at given ratios. A special crystalline structure may be a determining factors of higher catalytic efficiency. The higher reaction rate in the case of $Cu^{II}O$ can be attributed to the smaller crystallite size, lower band-gap energy, and highly crystalline structure. Both $Fe^{III}_2O_3$ and $Fe^{II}O$ NPs rendered lower degradation efficiencies in comparison to $Cu^{II}O$, NP-3, and metal oxides composite ($Cu^{II}O/Fe^{II}O/Fe^{III}_2O_3$), which may be attributed to a high degree of agglomeration and comparatively larger crystallite sizes.

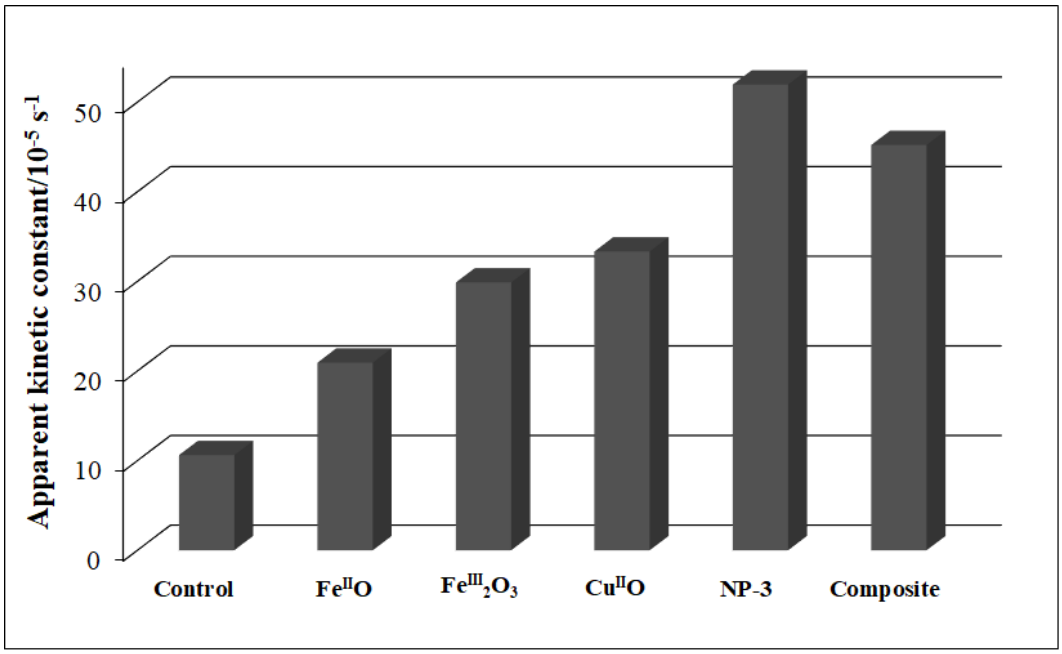

Figure 50. Comparison of apparent kinetic constants of $Fe^{II}O$, $Fe^{III}_2O_3$, $Cu^{II}O$, NP-3 ($Cu^{II}_{0.4}Fe^{II}_{0.6}Fe^{III}_2O_4$), and ($Cu^{II}O/Fe^{II}O/ Fe^{III}_2O_3$) composite. Concentrations: MB = 1.5×10^{-5} mol/L, NPs = 400 mg/L, irradiation time = 140 min, temperature = 25±2 °C, and $H_2O_2 = 1.76\times10^{-1}$ mol/L

Next, the heterogeneous photo-Fenton degradation of RhB was investigated by using metal oxides, doped ferrite (NP-3) and metal oxide composite ($Cu^{II}O/Fe^{II}O/Fe^{III}_2O_3$) NPs. Figure 51 revealed that almost 100% of RhB was degraded by using $Cu^{II}O$ within half of the applied experimental time. $Cu^{II}O$ revealed the best photocatalytic performance followed by metal oxide composite ($Cu^{II}O/Fe^{II}O/Fe^{III}_2O_3$), and NP-3, as the consequence of smaller crystallite size, band gap energies and low degree of agglomeration. The same photodegradation trend was observed in the case of MB. However, the use of $Cu^{II}O$ in

photo-Fenton degradation of RhB was the most effective, what can suggest that, in this case, the low band-gap energy may be the determining factor in the efficiency.

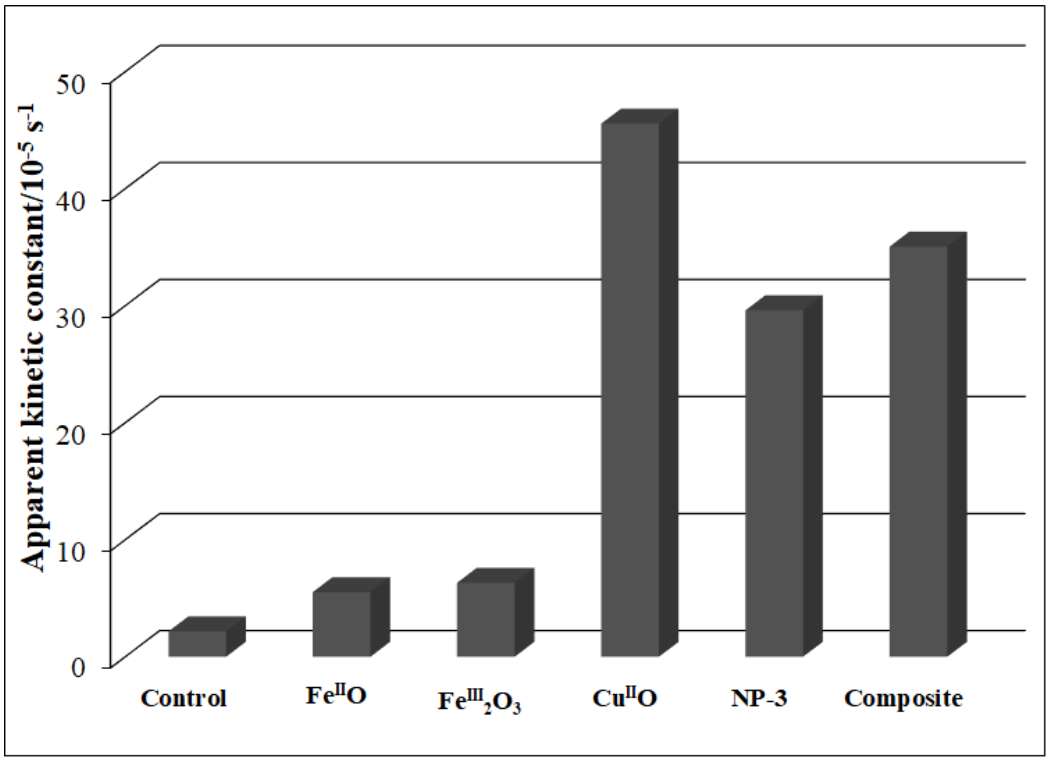

Figure 51. Comparison of apparent kinetic constants of $Fe^{II}O$, $Fe^{III}_2O_3$, $Cu^{II}O$, NP-3 ($Cu^{II}_{0.4}Fe^{II}_{0.6}Fe^{III}_2O_4$), and ($Cu^{II}O/Fe^{II}O/Fe^{III}_2O_3$) composite in the photodegradation of RhB. Concentrations: RhB = 1.75×10^{-5} mol/L, NPs = 400 mg/L, irradiation time = 140 min, temperature = 25±2 °C, and H_2O_2 = 1.76×10^{-1} mol/L

4.6 Reusability of NPs

The reusability of doped ferrite (NP-3) and metal oxide composite ($Cu^{II}O/Fe^{II}O/Fe^{III}_2O_3$) was investigated for 5 cycles under the similar experimental conditions. It was observed that the degradation efficiency (i.e., the rate constant) increased until the third cycle in the case of NP-3 (Figure 52) which can be assessed from increased in apparent kinetic constant values. Its value did not change in the fourth cycle, while indicated some decrease in the fifth one. Most of the researchers reported a small decrease in the reaction rate after each cycle, but this heterogeneous Fenton system behaved quite differently, with a significant increase of the efficiency up to the fourth cycle. This phenomenon suggests that the use of the catalyst increases the accessibility of the active sites on the particle surface.

In the case of metal oxide composite ($Cu^{II}O/Fe^{II}O/Fe^{III}_2O_3$) almost the same trend (Figure 53) was observed as NP-3, which proved that this composite too, is applicable for several cycles in a heterogeneous system.

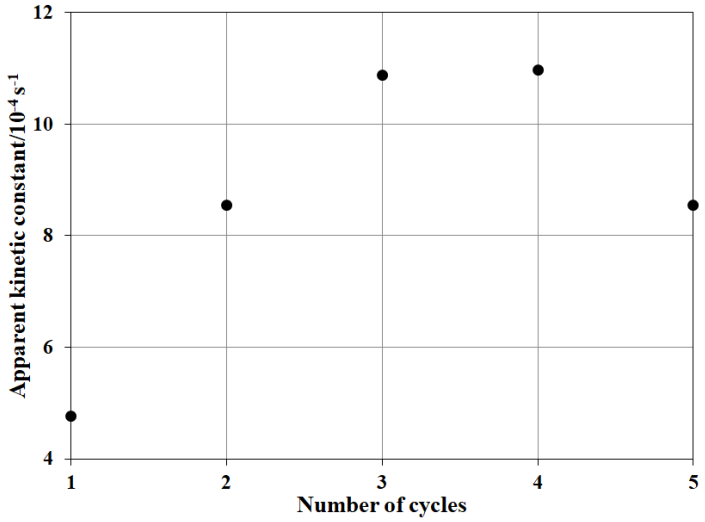

Figure 52. The effect of the reuse of the NP-3 catalyst on the relative efficiency the MB degradation. Concentrations: NP-3 = 400 mg/L, conc. of MB = 1.5×10^{-5} mol/L, pH = 7.5, time = 140 min, temperature = 25±2 °C, and conc. of H_2O_2 = 1.76×10^{-1} mol/L.

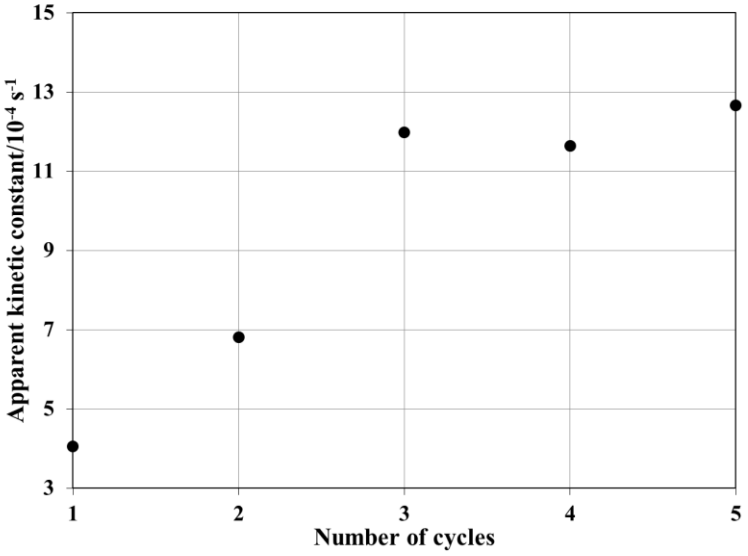

Figure 53. The effect of the reuse of ($Cu^{II}O/Fe^{II}O/Fe^{III}_2O_3$) composite catalyst on the relative efficiency the MB degradation. Conc. of composite = 400 mg/L, conc. of MB = 1.5×10^{-5} mol/L, temperature = 25±2 °C, time = 140 min, and conc. of H_2O_2 = 1.76×10^{-1} mol/L.

4.7 Antimicrobial results

The bacterial inhibition (%) of doped copper ferrites against gram negative *Vibrio fischeri* in the bioluminescence assay are illustrated in Figure 54. The inhibition (%) of bacteria in the presence of doped nanoparticles with various copper (Cu^{II}) and iron (Fe^{II}) concentrations revealed that all doped copper ferrites showed sufficient antibacterial activity. In our research, higher Cu^{II} content proved to be useful in achieving improved antibacterial activity. The same trend in bacterial inhibition against Gram-negative *Escherichia coli* was observed with copper-substituted cobalt ferrite nanoparticles synthesized by co-precipitation method [116].

In general, Cu^{II} possesses the ability to interrupt cell function in several ways. Hence, the ability of microorganisms to develop resistance against Cu^{II} is remarkably reduced. The attachment of Cu^{II} ions to the microorganism surface plays key role in antibacterial activity [218]. The ions from the surface of doped copper ferrites, especially Cu^{II}, are absorbed onto the cell wall of bacteria, causing damage its cell membrane in two possible ways i.e. altering enzyme functions or solidifying protein structures. Thus, the presence of copper ferrites in the bacterial growth medium causes bacteria to become immobilized and inactivated which inhibits further bacterial replication processes ultimately causing cell death [219].

In our study, a mechanism is proposed, according to which doped copper ferrites are attached (Figure 55) to the cell wall of *Vibrio fischeri*, and causing damage to the bacterial replication process. The bacterial inhibition in all cases is around 60%, which confirms the potential application of doped copper ferrites in antibacterial developments. However, in the literature, copper-silver ferrite nanoparticles revealed very similar antibacterial activity against gram negative and gram positive bacteria [220].

Simple metal oxides revealed almost the same effects to bacteria in bioluminescence inhibition assay (Figure 56). Thus, simple metal oxides and doped copper ferrites have the potential to inhibit the growth of bacteria.

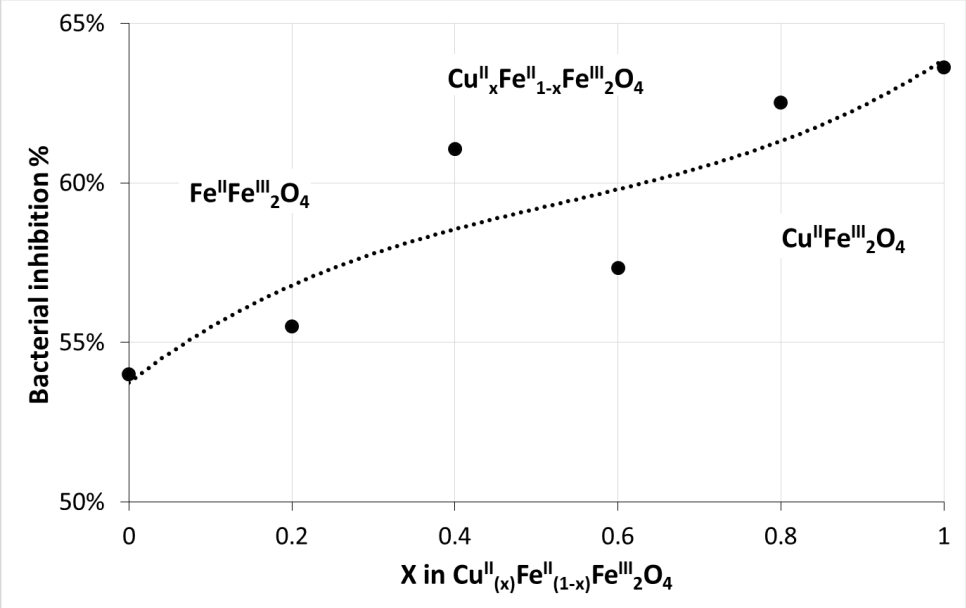

Figure 54. Comparison of bacterial inhibition percentage of doped copper ferrites against gram negative *Vibrio fischeri*

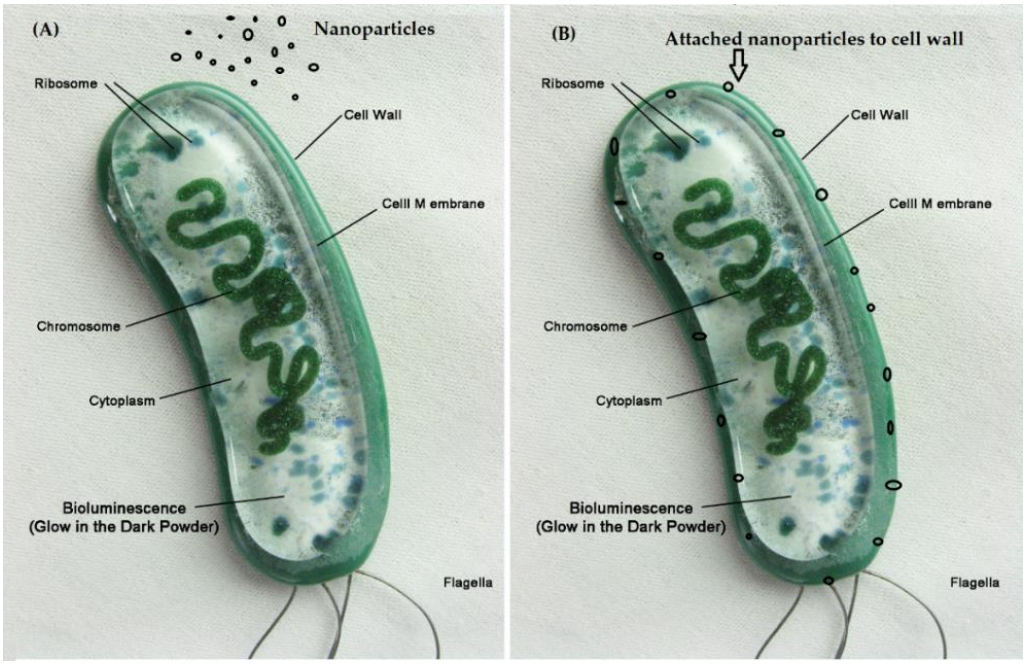

Figure 55. Proposed mechanism for the attachment of nanoparticles to *Vibrio fischeri*. (A) Bacteria and nanoparticles before attachment (B) after attachment

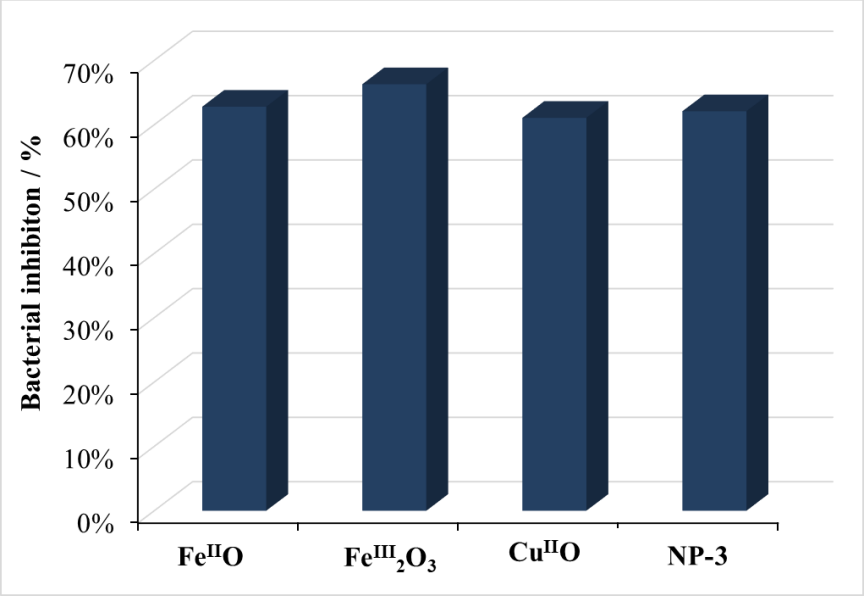

Figure 56. Comparison of bacterial inhibition percentage of $Fe^{II}O$, $Fe^{III}_2O_3$, $Cu^{II}O$, and doped NP-3 ($Cu^{II}_{0.4}Fe^{II}_{0.6}Fe^{III}_2O_4$)

5. New scientific results

A) The synthesis of iron(II)-doped copper ferrites NPs with alteration of the ratio of Cu^{2+} and Fe^{2+} in the composition given as $Cu^{II}_{(x)}Fe^{II}_{(1-x)}Fe^{III}_2O_4$ (where x = 0.0, 0.2, 0.4, 0.6, 0.8, 1.0 for NP-1, NP-2, NP-3, NP-4, NP-5 and NP-6, respectively) via simple co-precipitation technique as novel heterogeneous Fenton catalysts were characterized and their photocatalytic applications were investigated. Simple metal oxides ($Fe^{II}O$, $Cu^{II}O$, and $Fe^{III}_2O_3$) were also prepared to compare their corresponding features to those of the doped ferrites.

I) The particle size investigation confirmed that NPs were of submicrometer size, predominantly in the 70–200 nm range, which was favorable for the preparation of homogeneous aqueous dispersions.

II) XRD confirmed that NPs exhibit inverse spinel structure: metal ions with +2 charge (Fe^{2+} or Cu^{2+}) are in octahedral position, while the half of the Fe^{3+} ions are in tetrahedral one. This structure does not change during the substitution of Cu(II) ions to Fe(II) in the iron(II)-doped copper ferrites. This is confirmed by the very slight change in the main peak at about 35 deg (2θ) in the XRD diffractograms. The Raman spectra of NPs also

confirmed the inverse spinel structure. The vibrations under 600 cm^{-1} correspond to the M–O bonds at the octahedral sphere. Only one band belongs to the metal ions with tetrahedral coordination sphere—the symmetric stretching at 610 cm^{-1} (ν_s(M–O), E_g symmetry).

III) SEM confirmed the morphological changes occurred as a consequence of increasing Cu^{2+} ratio (x), the structure of NPs significantly changed from spherical (NP-1) to needle-like, embedded into clusters, in the case of NP-2 and NP-3. NP-4 formed larger needles on the surface, while NP-5 and NP-6 have some needle like crystals along with hexagonal crystals originating from a secondary nucleation. The EDS confirmed that major part of NPs were composed of Fe, Cu, and O, while some impurities in the form of Na and Cl were also present in some cases.

IV) An increase in the Cu^{2+}: Fe^{2+} ratio resulted in lower band-gap energies. NP-1 showed higher E_{bg} of 2.02 eV (613 nm), while NP-6 much lower E_{bg} of 1.25 eV (995 nm). It confirmed that copper ferrites may be able to harvest the energy of near infrared light in a photocatalytic system, too.

B) After successful structure elucidation of NPs, I investigated the photocatalytic performance of doped and simple metal oxide NPs, using two organic model compounds; Methylene blue (MB) and Rhodamine B (RhB) in photo-Fenton systems.

I) In the case of MB, the efficiency of six doped copper ferrites were analyzed at various reaction conditions. NP-3 proved to be the most efficient photocatalyst in the series studied. On the basis of the experiment, the optimized values for the reaction conditions such as catalyst dosage, hydrogen peroxide concentration, and pH were determined to be 400 mg/L, 1.76×10^{-1} mol/L, and 7.5, respectively. The total disappearance of the UV-visible spectra of MB confirmed the complete removal of the dye from the aqueous medium.

II) Also, in the case of RhB, NP-3 proved to be the most efficient photocatalyst in the series studied. The optimized values of the reaction conditions such

as catalyst dosage, hydrogen peroxide concentration, and pH were determined to be 500 mg/L, 8.88×10^{-2} mol/L, and 7.5, respectively.

C) To confirm the reusability and stability of catalysts at optimized reaction conditions, I checked NP-3 from the series of doped metal ferrites and simple metal oxide composite ($Fe^{II}O$, $Cu^{II}O$, and $Fe^{III}_2O_3$) for reusability in photocatalytic applications.

   I) Under five cycles of reusability experimental series, NP-3 and the composite ($Fe^{II}O$, $Cu^{II}O$, and $Fe^{III}_2O_3$) showed an increase in the reaction rate up to the third cycle, as the consequence of the potential degradation of initial impurities on the active sites of photocatalysts. A slight decrease in the fourth and fifth cycles could be attributed to the loss of the catalyst between the cycles.

   II) The leaching of metal ions into the solution was lower than 1%, confirmed by ICP and spectrophotometric measurements.

D) To compare the photocatalytic performance of simple metal oxides, doped (NP-3) and the composite of the metal oxides ($Fe^{II}O$, $Cu^{II}O$, and $Fe^{III}_2O_3$), all these catalysts were applied in photo-Fenton system under similar reaction conditions, using MB and RhB as model compounds.

   I) Using MB as model compound, the following sequence for reaction rate was observed: NP-3 > ($Fe^{II}O$, $Cu^{II}O$, and $Fe^{III}_2O_3$) > $Cu^{II}O$ > $Fe^{III}_2O_3$ > $Fe^{II}O$. This decreasing tendency may be attributed to higher degree of agglomeration and comparatively larger crystallite sizes.

   II) A similar sequence was observed for the use of RhB as model compound: $Cu^{II}O$ > ($Fe^{II}O$, $Cu^{II}O$, and $Fe^{III}_2O_3$) > NP-3 > $Fe^{III}_2O_3$ > $Fe^{II}O$. The small differences may originate from the lower band-gap energy and highly crystalline structure.

   III) On the basis of comparison studies, it can be confidently concluded that NP-3, composite of metal oxides ($Fe^{II}O$, $Cu^{II}O$, $Fe^{III}_2O_3$) and $Cu^{II}O$ alone have strong degradation potential for organic compounds.

E) The antimicrobial activity of doped copper ferrites and simple metal oxides were investigated in a bioluminescence inhibition assay. It was proved that all simple

metal oxides and all doped copper ferrites exhibited more than 60% antimicrobial property against the gram negative bacterium *Vibrio fischeri* in the bioluminescence inhibition assay.

On the basis of the above mentioned scientific results, it can be concluded that the $Cu^{II}_{(x)}Fe^{II}_{(1-x)}Fe^{III}_2O_4$ nanoparticles as novel heterogeneous Fenton catalysts prepared in this work showed significant activities in the photodegradation of Methylene Blue and Rhodamine B dyes. The increasing ratio of Cu^{2+} (x) in the iron(II)-doped ferrites resulted in the decrease of the band-gap energy and the crystal size. $Cu^{II}_{0.4}Fe^{II}_{0.6}Fe^{III}_2O_4$ (NP-3) proved to be the most active photocatalyst in the series of six NPs, partly due to its transition structure containing both spherical and small needle-like particles. At the optimized conditions, the efficiencies for MB and RhB degradation were several times higher in the presence of photocatalysts than that in their absence. Also, the metal oxide composite ($Cu^{II}O/Fe^{II}O/Fe^{III}_2O_3$) and $Cu^{II}O$ alone showed strong degradation potential for both model compounds at optimized conditions. Contrary to other heterogeneous Fenton systems, our catalysts exhibit higher efficiencies at neutral and alkaline pH, as well as better reusability and stability. In addition, simple metal oxides and doped ferrite (NP-3) exhibit enough antimicrobial property against the gram negative bacterium *Vibrio fischeri* in the bioluminescence inhibition assay. Our results unambiguously indicate that this type of NPs can be used in heterogeneous photo-Fenton systems to efficiently remove toxic organic compounds from wastewaters.

6. Acknowledgement

The proficient support of Prof. Dr. Prof. Ottó Horváth and Dr. Zsolt Valicsek during the whole study period is highly appreciated.

The competent assistances of Dr. Kristóf Kovács, Dr. Balázs Zsirka, Dr. Éva Kristóf-Makó, and Dr. Tatjána Juzsakova, Valéria Andirkó and Edina Ring-Nyári are gratefully acknowledged.

7. Funding

This work was supported by the Széchenyi 2020 under the GINOP-2.3.2-15-2016-00016 and from the Higher Educational Institutional Excellence Program 2019 the grant

of the Hungarian Ministry for Innovation and Technology. (Grant Number: NKFIH-1158-6/2019).

This work was financially supported by the Stipendum Hungaricum Scholarship Program under the Tempus Public Foundation (TPF) for PhD studies under bilateral collaboration with the Higher Education Commission (HEC) of Pakistan.

8. References

[1] Chen, D. and Ray, A. K., "Photocatalytic kinetics of phenol and its derivatives over UV irradiated TiO_2", *Applied Catalysis B: Environmental,* vol. 23, pp. 143-157, 1999.

[2] Mehrotra, K. and Ray, A. K., "Performance enhancement of photocatalytic reactor utilizing flow instability", *International Journal of Chemical Reactor Engineering,* vol. 1, A12, 2003.

[3] Kirchner, E. J., Fanoulis, E., and Dorussen, H., "Civil security in the EU: national persistence versus EU ambitions?", *European Security,* vol. 24, pp. 287-303, 2015.

[4] Wang, X., Pehkonen, S., and Ray, A. K., "Removal of aqueous Cr (VI) by a combination of photocatalytic reduction and coprecipitation", *Industrial & Engineering Chemistry Research,* vol. 43, pp. 1665-1672, 2004.

[5] Vinu, R., Akki, S. U., and Madras, G., "Investigation of dye functional group on the photocatalytic degradation of dyes by nano-TiO_2", *Journal of Hazardous Materials,* vol. 176, pp. 765-773, 2010.

[6] Neamtu, M., Yediler, A., Siminiceanu, I., Macoveanu, M., and Kettrup, A., "Decolorization of disperse red 354 azo dye in water by several oxidation processes—a comparative study", *Dyes and Pigments,* vol. 60, pp. 61-68, 2004.

[7] Rauf, M. and Ashraf, S. S., "Fundamental principles and application of heterogeneous photocatalytic degradation of dyes in solution", *Chemical Engineering Journal,* vol. 151, pp. 10-18, 2009.

[8] Forgacs, E., Cserhati, T., and Oros, G., "Removal of synthetic dyes from wastewaters: a review", *Environment International,* vol. 30, pp. 953-971, 2004.

[9] Gernjak, W., Maldonado, M., Malato, S., Caceres, J., Krutzler, T., Glaser, A., *et al.,* "Pilot-plant treatment of olive mill wastewater (OMW) by solar TiO_2 photocatalysis and solar photo-Fenton", *Solar Energy,* vol. 77, pp. 567-572, 2004.

[10] Malato, S., Blanco, J., Alarcón, D. C., Maldonado, M. I., Fernandez-Ibanez, P., and Gernjak, W., "Photocatalytic decontamination and disinfection of water with solar collectors", *Catalysis Today,* vol. 122, pp. 137-149, 2007.

[11] Esplugas, S., Gimenez, J., Contreras, S., Pascual, E., and Rodríguez, M., "Comparison of different advanced oxidation processes for phenol degradation", *Water Research,* vol. 36, pp. 1034-1042, 2002.

[12] Islam, N. and Miyazaki, K., "NanoSI: exploring nanotechnology research conflation and nano-innovation dynamism in the case of Japan", *Science and Public Policy,* vol. 36, pp. 170-182, 2009.

[13] Verma, S., "Phycosynthesis of silver nanoparticles using Spirulina platensis as a potential source of antibacterial agent", *PhD Thesis*, India, Corpus ID: 93864893, 2013.
[14] Khan, I., Saeed, K., and Khan, I., "Nanoparticles: Properties, applications and toxicities", *Arabian Journal of Chemistry,* vol. 12, pp. 908-931, 2019.
[15] Kreuter, J., "Application of nanoparticles for the delivery of drugs to the brain," in *International Congress Series*, 2005, vol. 1277, pp. 85-94.
[16] Luo, X., Morrin, A., Killard, A. J., and Smyth, M. R., "Application of nanoparticles in electrochemical sensors and biosensors", *Electroanalysis: An International Journal Devoted to Fundamental and Practical Aspects of Electroanalysis,* vol. 18, pp. 319-326, 2006.
[17] Rodríguez, J. A. and Fernández-García, M., *Synthesis, properties, and applications of oxide nanomaterials*: John Wiley & Sons, Inc., Hoboken, NJ, 2007.
[18] Fernandez-Garcia, M., Martinez-Arias, A., Hanson, J., and Rodriguez, J., "Nanostructured oxides in chemistry: characterization and properties", *Chemical Reviews,* vol. 104, pp. 4063-4104, 2004.
[19] Fernández-García, M. and Rodriguez, J. A., "Metal oxide nanoparticles", *Encyclopedia of Inorganic and Bioinorganic Chemistry,* 2011.
[20] Gleiter, H., "Nanostructured materials: state of the art and perspectives", *Nanostructured Materials,* vol. 6, pp. 3-14, 1995.
[21] Trudeau, M. and Ying, J., "Nanocrystalline materials in catalysis and electrocatalysis: structure tailoring and surface reactivity", *Nanostructured Materials,* vol. 7, pp. 245-258, 1996.
[22] Reddy, B., "Redox properties of oxides in "Metal Oxides"(Fierro, JLG:; Ed.)", *CRC Press, Boca Ratón,* 2006.
[23] He, Y., Miao, Y., Li, C., Wang, S., Cao, L., Xie, S., *et al.*, "Size and structure effect on optical transitions of iron oxide nanocrystals", *Physical Review B,* vol. 71, p. 125411, 2005.
[24] Matter, G. and Martinez-Arias, A., "Transport Properties and Oxygen Handling", *Synthesis, Properties and Application of Oxide Nanoparticles, Whiley, New Jersey,* pp. 150-164, 2007.
[25] Comninellis, C., Kapalka, A., Malato, S., Parsons, S. A., Poulios, I., and Mantzavinos, D., "Advanced oxidation processes for water treatment: advances and trends for R&D", *Journal of Chemical Technology & Biotechnology: International Research in Process, Environmental & Clean Technology,* vol. 83, pp. 769-776, 2008.
[26] Poyatos, J. M., Muñio, M., Almecija, M., Torres, J., Hontoria, E., and Osorio, F., "Advanced oxidation processes for wastewater treatment: state of the art", *Water, Air, and Soil Pollution,* vol. 205, p. 187, 2010.
[27] Pouran, S. R., Aziz, A. A., and Daud, W. M. A. W., "Review on the main advances in photo-Fenton oxidation system for recalcitrant wastewaters", *Journal of Industrial and Engineering Chemistry,* vol. 21, pp. 53-69, 2015.
[28] Dutta, K., Mukhopadhyay, S., Bhattacharjee, S., and Chaudhuri, B., "Chemical oxidation of methylene blue using a Fenton-like reaction", *Journal of Hazardous Materials,* vol. 84, pp. 57-71, 2001.

[29] Pérez, M., Torrades, F., Domènech, X., and Peral, J., "Fenton and photo-Fenton oxidation of textile effluents", *Water Research,* vol. 36, pp. 2703-2710, 2002.
[30] Rusevova, K., Kopinke, F.D., and Georgi, A., "Nano-sized magnetic iron oxides as catalysts for heterogeneous Fenton-like reactions—Influence of Fe(II)/Fe(III) ratio on catalytic performance", *Journal of Hazardous Materials,* vol. 241, pp. 433-440, 2012.
[31] Cai, H., Li, X., Ma, D., Feng, Q., Wang, D., Liu, Z., *et al.*, "Stable Fe_3O_4 submicrospheres with SiO_2 coating for heterogeneous Fenton-like reaction at alkaline condition", *Science of The Total Environment,* vol. 764, p. 144200, 2021.
[32] Ameta, R., Solanki, M. S., Benjamin, S., and Ameta, S. C., "Photocatalysis," in *Advanced Oxidation Processes for Wastewater Treatment*, ed: Elsevier, pp. 135-175, 2018.
[33] Serpone, N., "Photocatalysis", *Kirk-Othmer Encyclopedia of Chemical Technology,* 2000.
[34] Li, K., An, X., Park, K. H., Khraisheh, M., and Tang, J., "A critical review of CO_2 photoconversion: Catalysts and reactors", *Catalysis Today,* vol. 224, pp. 3-12, 2014.
[35] Mishra, M. and Chun, D. M., "α-Fe_2O_3 as a photocatalytic material: A review", *Applied Catalysis A: General,* vol. 498, pp. 126-141, 2015.
[36] Ahmed, S. N. and Haider, W., "Heterogeneous photocatalysis and its potential applications in water and wastewater treatment: a review", *Nanotechnology,* vol. 29, p. 342001, 2018.
[37] Biń, A. K. and Sobera-Madej, S., "Comparison of the advanced oxidation processes (UV, UV/H_2O_2 and O_3) for the removal of antibiotic substances during wastewater treatment", *Ozone: Science & Engineering,* vol. 34, pp. 136-139, 2012.
[38] Colmenares, J. C. and Xu, Y. J., "Heterogeneous photocatalysis", *Green Chemistry and Sustainable Technology,* Springer, Berlin, Heidelberg, 2016.
[39] Arimi, A., Megatif, L., Granone, L. I., Dillert, R., and Bahnemann, D. W., "Visible-light photocatalytic activity of zinc ferrites", *Journal of Photochemistry and Photobiology A: Chemistry,* vol. 366, pp. 118-126, 2018.
[40] Nakata, K., Ochiai, T., Murakami, T., and Fujishima, A., "Photoenergy conversion with TiO_2 photocatalysis: New materials and recent applications", *Electrochimica Acta,* vol. 84, pp. 103-111, 2012.
[41] Hashimoto, K., Irie, H., and Fujishima, A., "TiO_2 photocatalysis: a historical overview and future prospects", *Japanese Journal of Applied Physics,* vol. 44, p. 8269, 2005.
[42] Ding, Z., Lu, G., and Greenfield, P., "Role of the crystallite phase of TiO_2 in heterogeneous photocatalysis for phenol oxidation in water", *The Journal of Physical Chemistry B,* vol. 104, pp. 4815-4820, 2000.
[43] Górska, P., Zaleska, A., Kowalska, E., Klimczuk, T., Sobczak, J. W., Skwarek, E., *et al.*, "TiO_2 photoactivity in vis and UV light: the influence of calcination temperature and surface properties", *Applied Catalysis B: Environmental,* vol. 84, pp. 440-447, 2008.
[44] He, H., "Solvothermal synthesis and photocatalytic property of N doped TiO_2 powders", *Materials Research Innovations,* vol. 14, pp. 165-168, 2010.

[45] Farouk, H. U., Raman, A. A. A., and Daud, W. M. A. W., "TiO_2 catalyst deactivation in textile wastewater treatment: current challenges and future advances", *Journal of Industrial and Engineering Chemistry,* vol. 33, pp. 11-21, 2016.

[46] Burda, C., Lou, Y., Chen, X., Samia, A. C., Stout, J., and Gole, J. L., "Enhanced nitrogen doping in TiO_2 nanoparticles", *Nano Letters,* vol. 3, pp. 1049-1051, 2003.

[47] Liu, G., Han, C., Pelaez, M., Zhu, D., Liao, S., Likodimos, V., *et al.*, "Synthesis, characterization and photocatalytic evaluation of visible light activated C-doped TiO_2 nanoparticles", *Nanotechnology,* vol. 23, p. 294003, 2012.

[48] Chong, M. N., Jin, B., Chow, C. W., and Saint, C., "Recent developments in photocatalytic water treatment technology: a review", *Water Research,* vol. 44, pp. 2997-3027, 2010.

[49] Yang, X., Cao, C., Erickson, L., Hohn, K., Maghirang, R., and Klabunde, K., "Photo-catalytic degradation of Rhodamine B on C-, S-, N-, and Fe-doped TiO_2 under visible-light irradiation", *Applied Catalysis B: Environmental,* vol. 91, pp. 657-662, 2009.

[50] Chen, D., Huang, F., Ren, G., Li, D., Zheng, M., Wang, Y., *et al.*, "ZnS nano-architectures: photocatalysis, deactivation and regeneration", *Nanoscale,* vol. 2, pp. 2062-2064, 2010.

[51] Wu, W., Xiao, X., Zhang, S., Zhou, J., Ren, F., and Jiang, C., "Controllable synthesis of TiO_2 submicrospheres with smooth or rough surface", *Chemistry Letters,* vol. 39, pp. 684-685, 2010.

[52] Thurston, T. and Wilcoxon, J., "Photooxidation of organic chemicals catalyzed by nanoscale MoS_2", *The Journal of Physical Chemistry B,* vol. 103, pp. 11-17, 1999.

[53] Shakir, I., Shahid, M., and Kang, D. J., "MoO_3 and $Cu_{0.33}MoO_3$ nanorods for unprecedented UV/Visible light photocatalysis", *Chemical Communications,* vol. 46, pp. 4324-4326, 2010.

[54] Xiang, Q., Yu, J., and Jaroniec, M., "Graphene-based semiconductor photocatalysts", *Chemical Society Reviews,* vol. 41, pp. 782-796, 2012.

[55] Wu, W., Jiang, C., and Roy, V. A., "Recent progress in magnetic iron oxide–semiconductor composite nanomaterials as promising photocatalysts", *Nanoscale,* vol. 7, pp. 38-58, 2015.

[56] Kharisov, B. I., Dias, H. R., and Kharissova, O. V., "Mini-review: ferrite nanoparticles in the catalysis", *Arabian Journal of Chemistry,* vol. 12, pp. 1234-1246, 2019.

[57] Dom, R., Subasri, R., Radha, K., and Borse, P. H., "Synthesis of solar active nanocrystalline ferrite, MFe_2O_4 (M: Ca, Zn, Mg) photocatalyst by microwave irradiation", *Solid State Communications,* vol. 151, pp. 470-473, 2011.

[58] Casbeer, E., Sharma, V. K., and Li, X. Z., "Synthesis and photocatalytic activity of ferrites under visible light: a review", *Separation and Purification Technology,* vol. 87, pp. 1-14, 2012.

[59] Lim, C. W. and Lee, I. S., "Magnetically recyclable nanocatalyst systems for the organic reactions", *Nano Today,* vol. 5, pp. 412-434, 2010.

[60] Lu, H. C., Chang, J. E., Vong, W. W., Chen, H. T., and Chen, Y. L., "Porous ferrite synthesis and catalytic effect on benzene degradation", *International Journal of Physical Sciences,* vol. 6, pp. 855-865, 2011.

[61] Gaikwad, R. S., Chae, S. Y., Mane, R. S., Han, S. H., and Joo, O. S., "Cobalt ferrite nanocrystallites for sustainable hydrogen production application", *International Journal of Electrochemistry,* vol. 2011, pp. 1-6, 2011.

[62] Oliveira, L., Fabris, J., Rios, R., Mussel, W., and Lago, R., "$Fe_{3-x}Mn_xO_4$ catalysts: phase transformations and carbon monoxide oxidation", *Applied Catalysis A: General,* vol. 259, pp. 253-259, 2004.

[63] Sue, K., Aoki, M., Sato, T., Nishio-Hamane, D., Kawasaki, S.-i., Hakuta, Y., *et al.*, "Continuous hydrothermal synthesis of nickel ferrite nanoparticles using a central collision-type micromixer: effects of temperature, residence time, metal salt molality, and NaOH addition on conversion, particle size, and crystal phase", *Industrial & Engineering Chemistry Research,* vol. 50, pp. 9625-9631, 2011.

[64] Gibson, M. A. and Hightower, J. W., "Oxidative dehydrogenation of butenes over magnesium ferrite kinetic and mechanistic studies", *Journal of Catalysis,* vol. 41, pp. 420-430, 1976.

[65] Manova, E., Tsoncheva, T., Paneva, D., Mitov, I., Tenchev, K., and Petrov, L., "Mechanochemically synthesized nano-dimensional iron–cobalt spinel oxides as catalysts for methanol decomposition", *Applied Catalysis A: General,* vol. 277, pp. 119-127, 2004.

[66] Tihay, F., Roger, A., Pourroy, G., and Kiennemann, A., "Role of the alloy and spinel in the catalytic behavior of Fe−Co/cobalt magnetite composites under CO and CO_2 hydrogenation", *Energy & Fuels,* vol. 16, pp. 1271-1276, 2002.

[67] PalDey, S., Gedevanishvili, S., Zhang, W., and Rasouli, F., "Evaluation of a spinel based pigment system as a CO oxidation catalyst", *Applied Catalysis B: Environmental,* vol. 56, pp. 241-250, 2005.

[68] Silva, J. B., Diniz, C. F., Lago, R. M., and Mohallem, N. D., "Catalytic properties of nanocomposites based on cobalt ferrites dispersed in sol–gel silica", *Journal of Non-Crystalline Solids,* vol. 348, pp. 201-204, 2004.

[69] Xiong, C., Chen, Q., Lu, W., Gao, H., Lu, W., and Gao, Z., "Novel Fe-based complex oxide catalysts for hydroxylation of phenol", *Catalysis Letters,* vol. 69, pp. 231-236, 2000.

[70] Spretz, R., Marchetti, S. G., Ulla, M., and Lombardo, E. A., "Fe/MgO formulations for the catalytic combustion of methane", *Journal of Catalysis,* vol. 194, pp. 167-174, 2000.

[71] Goodarz Naseri, M., Saion, E. B., Abbastabar Ahangar, H., Shaari, A. H., and Hashim, M., "Simple synthesis and characterization of cobalt ferrite nanoparticles by a thermal treatment method", *Journal of Nanomaterials,* vol. 2010, pp. 1-8, 2010.

[72] Dou, R., Cheng, H., Ma, J., and Komarneni, S., "Manganese doped magnetic cobalt ferrite nanoparticles for dye degradation via a novel heterogeneous chemical catalysis", *Materials Chemistry and Physics,* vol. 240, p. 122181, 2020.

[73] Goyal, A., Bansal, S., Chudasama, B., Tikoo, K., Kumar, V., and Singhal, S., "Augmenting the catalytic performance of spinel nanoferrites ($CoFe_2O_4$ and $NiFe_2O_4$) via incorporation of Al into the lattice", *New Journal of Chemistry,* vol. 41, pp. 8320-8332, 2017.

[74] Manikandan, A., Sridhar, R., Antony, S. A., and Ramakrishna, S., "A simple aloe vera plant-extracted microwave and conventional combustion synthesis:

morphological, optical, magnetic and catalytic properties of $CoFe_2O_4$ nanostructures", *Journal of Molecular Structure,* vol. 1076, pp. 188-200, 2014.

[75] Kumar, P. V., Short, M. P., Yip, S., Yildiz, B., and Grossman, J. C., "High surface reactivity and water adsorption on $NiFe_2O_4$ (111) surfaces", *The Journal of Physical Chemistry C,* vol. 117, pp. 5678-5683, 2013.

[76] Liang, J., Wei, Y., Zhang, J., Yao, Y., He, G., Tang, B., *et al.*, "Scalable green method to fabricate magnetically separable $NiFe_2O_4$-reduced graphene oxide nanocomposites with enhanced photocatalytic performance driven by visible light", *Industrial & Engineering Chemistry Research,* vol. 57, pp. 4311-4319, 2018.

[77] Iftikhar, A., Yousaf, S., Ali, F. A. A., Haider, S., Khan, S. U. D., Shakir, I., *et al.*, "Erbium-substituted $Ni_{0.4}Co_{0.6}Fe_2O_4$ ferrite nanoparticles and their hybrids with reduced graphene oxide as magnetically separable powder photocatalyst", *Ceramics International,* vol. 46, pp. 1203-1210, 2020.

[78] Rahman, A., Warsi, M. F., Shakir, I., Shahid, M., and Zulfiqar, S., "Fabrication of Ce^{3+} substituted nickel ferrite-reduced graphene oxide heterojunction with high photocatalytic activity under visible light irradiation", *Journal of Hazardous Materials,* vol. 394, p. 122593, 2020.

[79] Khan, M. Z., Gul, I. H., Baig, M. M., and Khan, A. N., "Comprehensive study on structural, electrical, magnetic and photocatalytic degradation properties of Al^{3+} ions substituted nickel ferrites nanoparticles", *Journal of Alloys and Compounds,* vol. 848, p. 155795, 2020.

[80] Baynosa, M. L., Mady, A. H., Kumar, D. R., Sayed, M. S., Tuma, D., and Shim, J.-J., "Eco-friendly synthesis of recyclable mesoporous zinc ferrite@ reduced graphene oxide nanocomposite for efficient photocatalytic dye degradation under solar radiation", *Journal of Colloid and Interface Science,* vol. 561, pp. 459-469, 2020.

[81] Fu, Y. and Wang, X., "Magnetically separable $ZnFe_2O_4$–graphene catalyst and its high photocatalytic performance under visible light irradiation", *Industrial & Engineering Chemistry Research,* vol. 50, pp. 7210-7218, 2011.

[82] Šutka, A., Pärna, R., Kleperis, J., Käämbre, T., Pavlovska, I., Korsaks, V., *et al.*, "Photocatalytic activity of non-stoichiometric $ZnFe_2O_4$ under visible light irradiation", *Physica Scripta,* vol. 89, p. 044011, 2014.

[83] Wang, M., Sun, Y., Chen, H., Zhang, Y., Wu, X., Huang, K., *et al.*, "Enhanced photoelectrochemical activity of nanostructured $ZnFe_2O_4$ thin films prepared by the electrospray technique", *CrystEngComm,* vol. 19, pp. 772-775, 2017.

[84] Jumeri, F., Lim, H., Ariffin, S., Huang, N., Teo, P., Fatin, S., *et al.*, "Microwave synthesis of magnetically separable $ZnFe_2O_4$-reduced graphene oxide for wastewater treatment", *Ceramics International,* vol. 40, pp. 7057-7065, 2014.

[85] Zaharieva, K., Rives, V., Tsvetkov, M., Cherkezova-Zheleva, Z., Kunev, B., Trujillano, R., *et al.*, "Preparation, characterization and application of nanosized copper ferrite photocatalysts for dye degradation under UV irradiation", *Materials Chemistry and Physics,* vol. 160, pp. 271-278, 2015.

[86] Ponhan, W. and Maensiri, S., "Fabrication and magnetic properties of electrospun copper ferrite ($CuFe_2O_4$) nanofibers", *Solid State Sciences,* vol. 11, pp. 479-484, 2009.

[87] Lakhani, V., Zhao, B., Wang, L., Trivedi, U., and Modi, K., "Negative magnetization, magnetic anisotropy and magnetic ordering studies on Al^{3+}-substituted copper ferrite", *Journal of Alloys and Compounds,* vol. 509, pp. 4861-4867, 2011.

[88] Naseri, M. G., Saion, E. B., Ahangar, H. A., and Shaari, A. H., "Fabrication, characterization, and magnetic properties of copper ferrite nanoparticles prepared by a simple, thermal-treatment method", *Materials Research Bulletin,* vol. 48, pp. 1439-1446, 2013.

[89] Lou, J. C. and Chang, C. K., "Catalytic oxidation of CO over a catalyst produced in the ferrite process", *Environmental Engineering Science,* vol. 23, pp. 1024-1032, 2006.

[90] Mahmoodi, N. M., "Photocatalytic ozonation of dyes using copper ferrite nanoparticle prepared by co-precipitation method", *Desalination,* vol. 279, pp. 332-337, 2011.

[91] Goyal, A., Bansal, S., and Singhal, S., "Facile reduction of nitrophenols: Comparative catalytic efficiency of MFe_2O_4 (M= Ni, Cu, Zn) nano ferrites", *International Journal of Hydrogen Energy,* vol. 39, pp. 4895-4908, 2014.

[92] Kannaujia, R., Prasad, V., Rawat, P., Rawat, V., Thakur, A., Majumdar, S., *et al.*, "Facile synthesis of $CuFe_2O_4$ doped polyacrylic acid hydrogel nanocomposite and its application in dye degradation", *Materials Letters,* vol. 252, pp. 198-201, 2019.

[93] Wei, L., Zhang, Y., Chen, S., Zhu, L., Liu, X., Kong, L., *et al.*, "Synthesis of nitrogen-doped carbon nanotubes-$FePO_4$ composite from phosphate residue and its application as effective Fenton-like catalyst for dye degradation", *Journal of Environmental Sciences,* vol. 76, pp. 188-198, 2019.

[94] Kodasma, R., Palas, B., Ersöz, G., and Atalay, S., "Photocatalytic activity of copper ferrite graphene oxide particles for an efficient catalytic degradation of Reactive Black 5 in water", *Ceramics International,* vol. 46, pp. 6284-6292, 2020.

[95] Chen, P., Xing, X., Xie, H., Sheng, Q., and Qu, H., "High catalytic activity of magnetic $CuFe_2O_4$/graphene oxide composite for the degradation of organic dyes under visible light irradiation", *Chemical Physics Letters,* vol. 660, pp. 176-181, 2016.

[96] Ye, P., Wu, D., Wang, M., Wei, Y., Xu, A., and Li, X., "Coating magnetic $CuFe_2O_4$ nanoparticles with OMS-2 for enhanced degradation of organic pollutants via peroxymonosulfate activation", *Applied Surface Science,* vol. 428, pp. 131-139, 2018.

[97] Zhao, Y., Lin, C., Bi, H., Liu, Y., and Yan, Q., "Magnetically separable $CuFe_2O_4$/AgBr composite photocatalysts: preparation, characterization, photocatalytic activity and photocatalytic mechanism under visible light", *Applied Surface Science,* vol. 392, pp. 701-707, 2017.

[98] Arifin, M. N., Karim, K. M. R., Abdullah, H., and Khan, M. R., "Synthesis of titania doped copper ferrite photocatalyst and its photoactivity towards methylene blue degradation under visible light irradiation", *Bulletin of Chemical Reaction Engineering & Catalysis,* vol. 14, p. 219, 2019.

[99] Khan, A., Valicsek, Z., and Horváth, O., "Synthesis, Characterization and Application of Iron (II) Doped Copper Ferrites ($Cu^{II}_{(x)}Fe^{II}_{(1-x)}Fe^{III}_2O_4$) as Novel Heterogeneous Photo-Fenton Catalysts", *Nanomaterials,* vol. 10, p. 921, 2020.

[100] Khan, A., Valicsek, Z., and Horváth, O., "Comparing the Degradation Potential of Copper (II), Iron (II), Iron (III) Oxides, and Their Composite Nanoparticles in a Heterogeneous Photo-Fenton System", *Nanomaterials,* vol. 11, p. 225, 2021.

[101] Zhenyu, L., Guangliang, X., and Yalin, Z., "Microwave assisted low temperature synthesis of MnZn ferrite nanoparticles", *Nanoscale Research Letters,* vol. 2, p. 40, 2007.

[102] Wang, L. and He, H., "Surface alkaline-acidic characteristics and photo catalytic properties of $Co_{1-x}Zn_xFe_2O_4$ nano-particles synthesized by hydrothermal method", *Journal of Scientific Research and Reports,* pp. 263-274, 2014.

[103] Sathishkumar, P., Mangalaraja, R. V., Anandan, S., and Ashokkumar, M., "$CoFe_2O_4/TiO_2$ nanocatalysts for the photocatalytic degradation of Reactive Red 120 in aqueous solutions in the presence and absence of electron acceptors", *Chemical Engineering Journal,* vol. 220, pp. 302-310, 2013.

[104] Velinov, N., Manova, E., Tsoncheva, T., Estournès, C., Paneva, D., Tenchev, K., *et al.*, "Spark plasma sintering synthesis of $Ni_{1-x}Zn_xFe_2O_4$ ferrites: Mössbauer and catalytic study", *Solid State Sciences,* vol. 14, pp. 1092-1099, 2012.

[105] Albuquerque, A. S., Tolentino, M. V., Ardisson, J. D., Moura, F. C., de Mendonça, R., and Macedo, W. A., "Nanostructured ferrites: structural analysis and catalytic activity", *Ceramics International,* vol. 38, pp. 2225-2231, 2012.

[106] Feng, X., Mao, G., Bu, F., Cheng, X., Jiang, D., and Jiang, J., "Controlled synthesis of monodisperse $CoFe_2O_4$ nanoparticles by the phase transfer method and their catalytic activity on methylene blue discoloration with H_2O_2", *Journal of Magnetism and Magnetic Materials,* vol. 343, pp. 126-132, 2013.

[107] Hao, J., Yang, W., Zhang, Z., Pan, S., Lu, B., Ke, X., *et al.*, "Hierarchical flower-like $Co_{3-x}Fe_xO_4$ ferrite hollow spheres: facile synthesis and catalysis in the degradation of methylene blue", *Nanoscale,* vol. 5, pp. 3078-3082, 2013.

[108] Singh, C., Goyal, A., and Singhal, S., "Nickel-doped cobalt ferrite nanoparticles: efficient catalysts for the reduction of nitroaromatic compounds and photo-oxidative degradation of toxic dyes", *Nanoscale,* vol. 6, pp. 7959-7970, 2014.

[109] Bhukal, S., Bansal, S., and Singhal, S., "Magnetic Mn substituted cobalt zinc ferrite systems: structural, electrical and magnetic properties and their role in photo-catalytic degradation of methyl orange azo dye", *Physica B: Condensed Matter,* vol. 445, pp. 48-55, 2014.

[110] Bhukal, S., Bansal, S., and Singhal, S., "$Co_{0.6}Zn_{0.4}Cu_{0.2}Cd_xFe_{1.8-x}O_4$ ($0.2 \leqslant x \leqslant 0.8$) magnetic ferrite nano-particle: Synthesis, characterization and photo-catalytic degradation of methyl orange", *Journal of Molecular Structure,* vol. 1059, pp. 150-158, 2014.

[111] Guo, R., Fang, L., Dong, W., Zheng, F., and Shen, M., "Magnetically separable $BiFeO_3$ nanoparticles with a γ-Fe_2O_3 parasitic phase: controlled fabrication and enhanced visible-light photocatalytic activity", *Journal of Materials Chemistry,* vol. 21, pp. 18645-18652, 2011.

[112] Lassoued, A. and Li, J., "Magnetic and photocatalytic properties of Ni–Co ferrites", *Solid State Sciences,* vol. 104, p. 106199, 2020.

[113] Pankhurst, Q. A., Connolly, J., Jones, S. K., and Dobson, J., "Applications of magnetic nanoparticles in biomedicine", *Journal of Physics D: Applied Physics,* vol. 36, p. R167, 2003.

[114] Li, S., Wang, E., Tian, C., Mao, B., Kang, Z., Li, Q., *et al.*, "Jingle-bell-shaped ferrite hollow sphere with a noble metal core: Simple synthesis and their magnetic and antibacterial properties", *Journal of Solid State Chemistry,* vol. 181, pp. 1650-1658, 2008.

[115] Rana, S., Srivastava, R., Sorensson, M., and Misra, R., "Synthesis and characterization of nanoparticles with magnetic core and photocatalytic shell: anatase TiO_2–$NiFe_2O_4$ system", *Materials Science and Engineering: B,* vol. 119, pp. 144-151, 2005.

[116] Samavati, A. and Ismail, A., "Antibacterial properties of copper-substituted cobalt ferrite nanoparticles synthesized by co-precipitation method", *Particuology,* vol. 30, pp. 158-163, 2017.

[117] Sawai, J., Igarashi, H., Hashimoto, A., Kokugan, T., and Shimizu, M., "Evaluation of growth inhibitory effect of ceramics powder slurry on bacteria by conductance method", *Journal of Chemical Engineering of Japan,* vol. 28, pp. 288-293, 1995.

[118] Yamamoto, O., "Influence of particle size on the antibacterial activity of zinc oxide", *International Journal of Inorganic Materials,* vol. 3, pp. 643-646, 2001.

[119] Yamamoto, O., Hotta, M., Sawai, J., Sasamoto, T., and Kojima, H., "Influence of powder characteristic of ZnO on antibacterial activity", *Journal of the Ceramic Society of Japan,* vol. 106, pp. 1007-1011, 1998.

[120] Zhang, L., Jiang, Y., Ding, Y., Povey, M., and York, D., "Investigation into the antibacterial behaviour of suspensions of ZnO nanoparticles (ZnO nanofluids)", *Journal of Nanoparticle Research,* vol. 9, pp. 479-489, 2007.

[121] Ali, S. G., Ansari, M. A., Khan, H. M., Jalal, M., Mahdi, A. A., and Cameotra, S. S., "Antibacterial and antibiofilm potential of green synthesized silver nanoparticles against imipenem resistant clinical isolates of P. aeruginosa", *BioNanoScience,* vol. 8, pp. 544-553, 2018.

[122] Payne, J. N., Waghwani, H. K., Connor, M. G., Hamilton, W., Tockstein, S., Moolani, H., *et al.*, "Novel synthesis of kanamycin conjugated gold nanoparticles with potent antibacterial activity", *Frontiers in Microbiology,* vol. 7, p. 607, 2016.

[123] Ansari, M. A., Khan, H. M., Alzohairy, M. A., Jalal, M., Ali, S. G., Pal, R., *et al.*, "Green synthesis of Al_2O_3 nanoparticles and their bactericidal potential against clinical isolates of multi-drug resistant Pseudomonas aeruginosa", *World Journal of Microbiology and Biotechnology,* vol. 31, pp. 153-164, 2015.

[124] Jalal, M., Ansari, M. A., Ali, S. G., Khan, H. M., and Rehman, S., "Anticandidal activity of bioinspired ZnO NPs: effect on growth, cell morphology and key virulence attributes of Candida species", *Artificial Cells, Nanomedicine, and Biotechnology,* vol. 46, pp. 912-925, 2018.

[125] Nehra, P., Chauhan, R., Garg, N., and Verma, K., "Antibacterial and antifungal activity of chitosan coated iron oxide nanoparticles", *British Journal of Biomedical Science,* vol. 75, pp. 13-18, 2018.

[126] Ismail, R. A., Sulaiman, G. M., Abdulrahman, S. A., and Marzoog, T. R., "Antibacterial activity of magnetic iron oxide nanoparticles synthesized by laser ablation in liquid", *Materials Science and Engineering: C,* vol. 53, pp. 286-297, 2015.

[127] Zhang, S., Niu, H., Cai, Y., Zhao, X., and Shi, Y., "Arsenite and arsenate adsorption on coprecipitated bimetal oxide magnetic nanomaterials: $MnFe_2O_4$ and $CoFe_2O_4$", *Chemical Engineering Journal,* vol. 158, pp. 599-607, 2010.

[128] Din, M. I., Jabbar, S., Najeeb, J., Khalid, R., Ghaffar, T., Arshad, M., *et al.*, "Green synthesis of zinc ferrite nanoparticles for photocatalysis of methylene blue", *International Journal of Phytoremediation,* vol. 22(13), pp. 1440-1447, 2020.

[129] Guo, J. F., Ma, B., Yin, A., Fan, K., and Dai, W. L., "Photodegradation of rhodamine B and 4-chlorophenol using plasmonic photocatalyst of Ag–$AgI/Fe_3O_4@SiO_2$ magnetic nanoparticle under visible light irradiation", *Applied Catalysis B: Environmental,* vol. 101, pp. 580-586, 2011.

[130] Gonzalez-Sandoval, M., Beesley, A., Miki-Yoshida, M., Fuentes-Cobas, L., and Matutes-Aquino, J., "Comparative study of the microstructural and magnetic properties of spinel ferrites obtained by co-precipitation", *Journal of Alloys and Compounds,* vol. 369, pp. 190-194, 2004.

[131] Sharma, R., Thakur, P., Kumar, M., Thakur, N., Negi, N., Sharma, P., *et al.*, "Improvement in magnetic behaviour of cobalt doped magnesium zinc nano-ferrites via co-precipitation route", *Journal of Alloys and Compounds,* vol. 684, pp. 569-581, 2016.

[132] Laurent, S., Forge, D., Port, M., Roch, A., Robic, C., Vander Elst, L., *et al.*, "Magnetic iron oxide nanoparticles: synthesis, stabilization, vectorization, physicochemical characterizations, and biological applications", *Chemical Reviews,* vol. 108, pp. 2064-2110, 2008.

[133] Manova, E., Tsoncheva, T., Paneva, D., Popova, M., Velinov, N., Kunev, B., *et al.*, "Nanosized copper ferrite materials: mechanochemical synthesis and characterization", *Journal of Solid State Chemistry,* vol. 184, pp. 1153-1158, 2011.

[134] Nabi, M. A. U., Moin, M., Hasan, M., Arshad, M., Bibi, A., Amin, N., *et al.*, "Study of Electrical Transport Properties of Cadmium-Doped Zn–Mn Soft Ferrites by Co-precipitation Method", *Journal of Superconductivity and Novel Magnetism,* pp. 1-10, 2020.

[135] Amin, N., Hasan, M. S. U., Majeed, Z., Latif, Z., un Nabi, M. A., Mahmood, K., *et al.*, "Structural, electrical, optical and dielectric properties of yttrium substituted cadmium ferrites prepared by Co-Precipitation method", *Ceramics International,* vol. 46(13), pp. 20798-20809, 2020.

[136] Fotukian, S. M., Barati, A., Soleymani, M., and Alizadeh, A. M., "Solvothermal synthesis of $CuFe_2O_4$ and Fe_3O_4 nanoparticles with high heating efficiency for magnetic hyperthermia application", *Journal of Alloys and Compounds,* vol. 816, p. 152548, 2020.

[137] de Medeiros, F., Madigou, V., Lopes-Moriyama, A., de Souza, C. P., and Leroux, C., "Synthesis of $CoFe_2O_4$ nanocubes", *Nano-Structures & Nano-Objects,* vol. 21, p. 100422, 2020.

[138] Zhang, X., Chen, Z., Wu, C., Zhang, J., and Wang, F., "Solvothermal synthesis of spinel $ZnFe_2O_4$ nanoparticles with enhanced infrared radiation property", *Chemical Physics Letters,* vol. 732, p. 136647, 2019.

[139] Kumar, N., Shukla, A., Kumar, N., and Choudhary, R., "Effects of milling time on structural, electrical and ferroelectric features of mechanothermally synthesized multi-doped bismuth ferrite", *Applied Physics A,* vol. 126, p. 181, 2020.

[140] Naresh, U., Kumar, R. J., and Naidu, K. C. B., "Hydrothermal synthesis of barium copper ferrite nanoparticles: Nanofiber formation, optical, and magnetic properties", *Materials Chemistry and Physics*, vol. 236, p. 121807, 2019.
[141] Yao, T., Qi, Y., Mei, Y., Yang, Y., Aleisa, R., Tong, X., *et al.*, "One-step preparation of reduced graphene oxide aerogel loaded with mesoporous copper ferrite nanocubes: A highly efficient catalyst in microwave-assisted Fenton reaction", *Journal of Hazardous Materials*, vol. 378, p. 120712, 2019.
[142] Hou, X., Feng, J., Xu, X., and Zhang, M., "Synthesis and characterizations of spinel $MnFe_2O_4$ nanorod by seed–hydrothermal route", *Journal of Alloys and Compounds*, vol. 491, pp. 258-263, 2010.
[143] Naseri, M. G., Saion, E. B., Ahangar, H. A., Hashim, M., and Shaari, A. H., "Synthesis and characterization of manganese ferrite nanoparticles by thermal treatment method", *Journal of Magnetism and Magnetic Materials*, vol. 323, pp. 1745-1749, 2011.
[144] Shirsath, S. E., Wang, D., Jadhav, S. S., Mane, M., and Li, S., "Ferrites obtained by sol-gel method," in *Handbook of Sol-gel Science and Technology*, ed: Springer Cham, 2018, pp. 695-735.
[145] Ye, C. Q., "Sol-Gel Processes of Functional Powders and Films", *Chemical Reactions in Inorganic Chemistry*, pp. 31-50, 2018.
[146] Yang, Y., Jiang, Y., Wang, Y., Sun, Y., Liu, L., and Zhang, J., "Influences of sintering atmosphere on the formation and photocatalytic property of $BaFe_2O_4$", *Materials Chemistry and Physics*, vol. 105, pp. 154-156, 2007.
[147] Maksoud, M. A., El-ghandour, A., El-Sayyad, G. S., Awed, A., Ashour, A., El-Batal, A. I., *et al.*, "Incorporation of Mn^{2+} into cobalt ferrite via sol–gel method: insights on induced changes in the structural, thermal, dielectric, and magnetic properties", *Journal of Sol-Gel Science and Technology*, vol. 90, pp. 631-642, 2019.
[148] Venturini, J., Wermuth, T. B., Machado, M. C., Arcaro, S., Alves, A. K., da Cas Viegas, A., *et al.*, "The influence of solvent composition in the sol-gel synthesis of cobalt ferrite ($CoFe_2O_4$): A route to tuning its magnetic and mechanical properties", *Journal of the European Ceramic Society*, vol. 39, pp. 3442-3449, 2019.
[149] Li, H., Zhang, Y., Wang, S., Wu, Q., and Liu, C., "Study on nanomagnets supported TiO_2 photocatalysts prepared by a sol–gel process in reverse microemulsion combining with solvent-thermal technique", *Journal of Hazardous Materials*, vol. 169, pp. 1045-1053, 2009.
[150] Hazra, S. and Ghosh, N., "Preparation of nanoferrites and their applications", *Journal of Nanoscience and Nanotechnology*, vol. 14, pp. 1983-2000, 2014.
[151] Gheisari, K., Bhame, S., Oh, J., and Javadpour, S., "Comparative studies on the structure and magnetic properties of Ni–Zn ferrite powders prepared by glycine-nitrate auto-combustion process and solid state reaction method", *Journal of Superconductivity and Novel Magnetism*, vol. 26, pp. 477-483, 2013.
[152] Ceylan, A., Ozcan, S., Ni, C., and Shah, S. I., "Solid state reaction synthesis of $NiFe_2O_4$ nanoparticles", *Journal of Magnetism and Magnetic Materials*, vol. 320, pp. 857-863, 2008.
[153] Huang, K., Yu, J., Zhang, L., Xu, J., Li, P., Yang, Z., *et al.*, "Synthesis and characterizations of magnesium and titanium doped M-type barium calcium

hexaferrites by a solid state reaction method", *Journal of Alloys and Compounds*, vol. 825, p. 154072, 2020.

[154] Das, N., Majumdar, R., Sen, A., and Maiti, H. S., "Nanosized bismuth ferrite powder prepared through sonochemical and microemulsion techniques", *Materials Letters*, vol. 61, pp. 2100-2104, 2007.

[155] Abraime, B., El Maalam, K., Fkhar, L., Mahmoud, A., Boschini, F., Tamerd, M. A., *et al.*, "Influence of synthesis methods with low annealing temperature on the structural and magnetic properties of $CoFe_2O_4$ nanopowders for permanent magnet application", *Journal of Magnetism and Magnetic Materials*, vol. 500, p. 166416, 2020.

[156] Ray, A. K. and Beenackers, A. A., "Development of a new photocatalytic reactor for water purification", *Catalysis Today*, vol. 40, pp. 73-83, 1998.

[157] Mukherjee, P. S. and Ray, A. K., "Major challenges in the design of a large-scale photocatalytic reactor for water treatment", *Chemical Engineering & Technology: Industrial Chemistry-Plant Equipment-Process Engineering-Biotechnology,* vol. 22, pp. 253-260, 1999.

[158] Ray, A. K., "A new photocatalytic reactor for destruction of toxic water pollutants by advanced oxidation process", *Catalysis Today*, vol. 44, pp. 357-368, 1998.

[159] Hashim, N., "Visible light driven photocatalysis for degradation of diclofenac", PhD Thesis, The University of Western Ontario, 2016.

[160] Ray, A. K., "Design, modelling and experimentation of a new large-scale photocatalytic reactor for water treatment", *Chemical Engineering Science*, vol. 54, pp. 3113-3125, 1999.

[161] Hashim, N., Natarajan, P., and Ray, A. K., "Intrinsic kinetic study for photocatalytic degradation of diclofenac under UV and visible light", *Industrial & Engineering Chemistry Research*, vol. 53, pp. 18637-18646, 2014.

[162] Rodríguez, S. M., Richter, C., Galvez, J. B., and Vincent, M., "Photocatalytic degradation of industrial residual waters", *Solar Energy*, vol. 56, pp. 401-410, 1996.

[163] Gaya, U. I. and Abdullah, A. H., "Heterogeneous photocatalytic degradation of organic contaminants over titanium dioxide: a review of fundamentals, progress and problems", *Journal of Photochemistry and Photobiology C: Photochemistry Reviews*, vol. 9, pp. 1-12, 2008.

[164] Guo, S., Zhang, G., and Jimmy, C. Y., "Enhanced photo-Fenton degradation of rhodamine B using graphene oxide–amorphous $FePO_4$ as effective and stable heterogeneous catalyst", *Journal of Colloid Interface Science*, vol. 448, pp. 460-466, 2015.

[165] Chen, C., Lu, C., Chung, Y., and Jan, J., "UV light induced photodegradation of malachite green on TiO_2 nanoparticles", *Journal of Hazardous Materials*, vol. 141, pp. 520-528, 2007.

[166] Patil, S., Naik, H. B., Nagaraju, G., Viswanath, R., and Rashmi, S., "Sugarcane juice mediated eco-friendly synthesis of visible light active zinc ferrite nanoparticles: Application to degradation of mixed dyes and antibacterial activities", *Materials Chemistry and Physics*, vol. 212, pp. 351-362, 2018.

[167] Soltani, T. and Entezari, M. H., "Solar photocatalytic degradation of RB5 by ferrite bismuth nanoparticles synthesized via ultrasound", *Ultrasonics Sonochemistry*, vol. 20, pp. 1245-1253, 2013.

[168] Huda, A., Mahendra, I. P., Ichwani, R., Handoko, C. T., Ngoc, H. M., Yudono, B., *et al.*, "High efficient visible-light activated photocatalytic semiconductor SnO_2/Sn_3O_4 heterostructure in direct blue 71 (DB71) degradation", *Rasayan Journal of Chemistry*, vol. 12, pp. 308-318, 2019.

[169] Evgenidou, E., Fytianos, K., and Poulios, I., "Semiconductor-sensitized photodegradation of dichlorvos in water using TiO_2 and ZnO as catalysts", *Applied Catalysis B: Environmental*, vol. 59, pp. 81-89, 2005.

[170] Rincón, A. and Pulgarin, C., "Photocatalytical inactivation of E. coli: effect of (continuous–intermittent) light intensity and of (suspended–fixed) TiO_2 concentration", *Applied Catalysis B: Environmental*, vol. 44, pp. 263-284, 2003.

[171] Malato, S., Fernández-Ibáñez, P., Maldonado, M. I., Blanco, J., and Gernjak, W., "Decontamination and disinfection of water by solar photocatalysis: recent overview and trends", *Catalysis Today*, vol. 147, pp. 1-59, 2009.

[172] Konstantinou, I. K. and Albanis, T. A., "TiO_2-assisted photocatalytic degradation of azo dyes in aqueous solution: kinetic and mechanistic investigations: a review", *Applied Catalysis B: Environmental*, vol. 49, pp. 1-14, 2004.

[173] Chong, M. N., Lei, S., Jin, B., Saint, C., and Chow, C. W., "Optimisation of an annular photoreactor process for degradation of Congo Red using a newly synthesized titania impregnated kaolinite nano-photocatalyst", *Separation and Purification Technology*, vol. 67, pp. 355-363, 2009.

[174] Iqubal, M. A. and Sharma, R., "Surface interaction of ribonucleic acid constituents with spinel ferrite nanoparticles: a prebiotic chemistry experiment", *RSC Advances*, vol. 6, pp. 68574-68583, 2016.

[175] Soltani, T. and Entezari, M. H., "Photolysis and photocatalysis of methylene blue by ferrite bismuth nanoparticles under sunlight irradiation", *Journal of Molecular Catalysis A: Chemical*, vol. 377, pp. 197-203, 2013.

[176] Soltani, T. and Entezari, M. H., "Sono-synthesis of bismuth ferrite nanoparticles with high photocatalytic activity in degradation of Rhodamine B under solar light irradiation", *Chemical Engineering Journal*, vol. 223, pp. 145-154, 2013.

[177] Ghanadzadeh, A., Zanjanchi, M.A. and Tirbandpay, R.,, "The role of host environment on the aggregative properties of some ionic dye materials", *Journal of Molecular Structure*, vol. 616, pp. 167-174, 2002.

[178] Shirayama, H., Tohezo, Y., and Taguchi, S., "Photodegradation of chlorinated hydrocarbons in the presence and absence of dissolved oxygen in water", *Water Research*, vol. 35, pp. 1941-1950, 2001.

[179] Wang, Y. and Hong, C. S., "TiO_2-mediated photomineralization of 2-chlorobiphenyl: the role of O2", *Water Research*, vol. 34, pp. 2791-2797, 2000.

[180] Chong, M. N., Jin, B., Zhu, H., Chow, C., and Saint, C., "Application of H-titanate nanofibers for degradation of Congo Red in an annular slurry photoreactor", *Chemical Engineering Journal*, vol. 150, pp. 49-54, 2009.

[181] Saquib, M. and Muneer, M., "TiO_2-mediated photocatalytic degradation of a triphenylmethane dye (gentian violet), in aqueous suspensions", *Dyes and Pigments*, vol. 56, pp. 37-49, 2003.

[182] Mahmoodi, N. M., "Manganese ferrite nanoparticle: Synthesis, characterization, and photocatalytic dye degradation ability", *Desalination and Water Treatment*, vol. 53, pp. 84-90, 2015.

[183] Mahmoodi, N. M., "Zinc ferrite nanoparticle as a magnetic catalyst: synthesis and dye degradation", *Materials Research Bulletin,* vol. 48, pp. 4255-4260, 2013.
[184] Abbas, N., Rubab, N., Sadiq, N., Manzoor, S., Khan, M.I., Fernandez Garcia, J., Barbosa Aragao, I., Tariq, M., Akhtar, Z. and Yasmin, G., , "Aluminum-Doped Cobalt Ferrite as an Efficient Photocatalyst for the Abatement of Methylene Blue", *Water,* vol. 12, p. 2285, 2020.
[185] Mandal, A., Ojha, K., De Asim, K., and Bhattacharjee, S., "Removal of catechol from aqueous solution by advanced photo-oxidation process", *Chemical Engineering Journal,* vol. 102, pp. 203-208, 2004.
[186] Xu, S., Feng, D., and Shangguan, W., "Preparations and photocatalytic properties of visible-light-active zinc ferrite-doped TiO_2 photocatalyst", *The Journal of Physical Chemistry C,* vol. 113, pp. 2463-2467, 2009.
[187] Sen, Z., *Solar energy fundamentals and modeling techniques: atmosphere, environment, climate change and renewable energy*: Springer Science & Business Media, 2008.
[188] Pathania, D., Sharma, S., and Singh, P., "Removal of methylene blue by adsorption onto activated carbon developed from Ficus carica bast", *Arabian Journal of Chemistry,* vol. 10, pp. S1445-S1451, 2017.
[189] Albert, M., Lessin, M. S., and Gilchrist, B. F., "Methylene blue: dangerous dye for neonates", *Journal of Pediatric Surgery,* vol. 38, pp. 1244-1245, 2003.
[190] Högfeldt, E., *Stability constants of metal-ion complexes: part A: inorganic ligands* vol. 21: Pergamon Pr, 1982.
[191] Tatarchuk, T., Bououdina, M., Macyk, W., Shyichuk, O., Paliychuk, N., Yaremiy, I., *et al.*, "Structural, optical, and magnetic properties of Zn-doped $CoFe_2O_4$ nanoparticles", *Nanoscale Research Letters,* vol. 12, p. 141, 2017.
[192] Shi, X., Tian, A., You, J., Yang, H., Wang, Y., and Xue, X., "Degradation of organic dyes by a new heterogeneous Fenton reagent-Fe_2GeS_4 nanoparticle", *Journal of Hazardous Materials,* vol. 353, pp. 182-189, 2018.
[193] Milošević, M. D., Logar, M. M., Poharc-Logar, A. V., and Jakšić, N. L., "Orientation and Optical Polarized Spectra (380–900 nm) of Methylene Blue Crystals on a Glass Surface", *International Journal of Spectroscopy,* vol. 2013, p. 923739, 2013.
[194] Wu, J. M. a. Z., T.W., "Photodegradation of rhodamine B in water assisted by titania films prepared through a novel procedure", *Journal of Photochemistry and Photobiology A: Chemistry,* vol. 162, pp. 171-177, 2004.
[195] Szabó-Bárdos, E., Kulcsár, P., Kováts, N., Békéssy, Z., Eck-Varanka, B., and Horváth, O., "Assessment of the potential bactericide effect of self-cleaning floors: a proposed protocol", *Luminescence,* vol. 35, pp. 434-436, 2020.
[196] Shen, Y., Wu, Y., Xu, H., Fu, J., Li, X., Zhao, Q., *et al.*, "Facile preparation of sphere-like copper ferrite nanostructures and their enhanced visible-light-induced photocatalytic conversion of benzene", *Material Research Bulletin,* vol. 48, pp. 4216-4222, 2013.
[197] Shannon, R. D., "Revised effective ionic radii and systematic studies of interatomic distances in halides and chalcogenides", *Acta Crystallographica A,* vol. 32, pp. 751-767, 1976.

[198] Anandan, S., Selvamani, T., Prasad, G.G., Asiri, A.M. and Wu, J.J., "Magnetic and catalytic properties of inverse spinel $CuFe_2O_4$ nanoparticles", *Journal of Magnetism and Magnetic Materials,* vol. 432, pp. 437-443, 2017.

[199] Mubarak Ali, D., Arunkumar, J., Pooja, P., Subramanian, G., Thajuddin, N. and Alharbi, N.S., "Synthesis and characterization of biocompatibility of tenorite nanoparticles and potential property against biofilm formation. 23(4), pp.421-428.", *Saudi Pharmaceutical Journal,* vol. 23, pp. 421-428, 2015.

[200] Su, C., Wang, H. and Liu, X., "Controllable fabrication and growth mechanism of hematite cubes 46(2), pp.209-214.", *Crystal Research and Technology,* vol. 46, pp. 209-214, 2011.

[201] Yu, W., Zhang, T., Zhang, J., Qiao, X., Yang, L. and Liu, Y., "The synthesis of octahedral nanoparticles of magnetite", *Materials Letters,* vol. 60, pp. 2998-3001, 2006.

[202] Abdou, S. M. a. M., H., "Characterization of table salt samples from different origins and ESR detection of the induced effects due to gamma irradiation", *In Journal of Physics: Conference Series,* vol. 1253, p. 012036, 2019.

[203] Chandramohan, P., Srinivasan, M., Velmurugan, S., and Narasimhan, S., "Cation distribution and particle size effect on Raman spectrum of $CoFe_2O_4$", *Journal of Solid State Chemistry,* vol. 184, pp. 89-96, 2011.

[204] Lassoued, A., Lassoued, M. S., Dkhil, B., Gadri, A., and Ammar, S., "Structural, optical and morphological characterization of Cu-doped α-Fe_2O_3 nanoparticles synthesized through co-precipitation technique", *Journal of Molecular Structure,* vol. 1148, pp. 276-281, 2017.

[205] Ameri, B., Davarani, S.S.H., Roshani, R., Moazami, H.R. and Tadjarodi, A., "A flexible mechanochemical route for the synthesis of copper oxide nanorods/nanoparticles/nanowires for supercapacitor applications: The effect of morphology on the charge storage ability. 695, pp.114-123.", *Journal of Alloys and Compounds,* vol. 695, pp. 114-123, 2017.

[206] Sayed, F. N. a. P., V., "Facile and sustainable synthesis of shaped iron oxide nanoparticles: effect of iron precursor salts on the shapes of iron oxides. 5(1), pp.1-14.", *Scientific Reports,* vol. 5, pp. 1-14, 2015.

[207] Masunga, N., Mmelesi, O.K., Kefeni, K.K. and Mamba, B.B., "Recent advances in copper ferrite nanoparticles and nanocomposites synthesis, magnetic properties and application in water treatment: Review", *Journal of Environmental Chemical Engineering,* vol. 7, p. 103179, 2019.

[208] Litter, M. I. and Blesa, M. A., "Photodissolution of iron oxides. IV. A comparative study on the photodissolution of hematite, magnetite, and maghemite in EDTA media", *Canadian Journal of Chemistry,* vol. 70, pp. 2502-2510, 1992.

[209] Dhineshbabu, N., Rajendran, V., Nithyavathy, N., and Vetumperumal, R., "Study of structural and optical properties of cupric oxide nanoparticles", *Applied Nanoscience,* vol. 6, pp. 933-939, 2016.

[210] Ahmed, Y., Yaakob, Z., and Akhtar, P., "Degradation and mineralization of methylene blue using a heterogeneous photo-Fenton catalyst under visible and solar light irradiation", *Catalysis Science Technololgy,* vol. 6, pp. 1222-1232, 2016.

[211] Wang, N., Zheng, T., Zhang, G., and Wang, P., "A review on Fenton-like processes for organic wastewater treatment", *Journal of Environmental Chemical Engineering*, vol. 4, pp. 762-787, 2016.
[212] Mills, A. a. W., J., "Photobleaching of methylene blue sensitised by TiO_2: an ambiguous system? ", *Journal of Photochemistry and Photobiology A: Chemistry*, vol. 127, pp. 123-134, 1999.
[213] Wang, X., Pan, Y., Zhu, Z., and Wu, J., "Efficient degradation of rhodamine B using Fe-based metallic glass catalyst by Fenton-like process", *Chemosphere*, vol. 117, pp. 638-643, 2014.
[214] Guo, S., Zhang, G., and Jimmy, C. Y., "Enhanced photo-Fenton degradation of rhodamine B using graphene oxide–amorphous $FePO_4$ as effective and stable heterogeneous catalyst", *Journal of Colloid and Interface Science*, vol. 448, pp. 460-466, 2015.
[215] Salem, M. A., Abdel-Halim, S. T., El-Sawy, A. E.-H. M., and Zaki, A. B., "Kinetics of degradation of allura red, ponceau 4R and carmosine dyes with potassium ferrioxalate complex in the presence of H_2O_2", *Chemosphere*, vol. 76, pp. 1088-1093, 2009.
[216] Zhang, L., Nie, Y., Hu, C., and Qu, J., "Enhanced Fenton degradation of Rhodamine B over nanoscaled Cu-doped $LaTiO_3$ perovskite", *Applied Catalysis B: Environmental*, vol. 125, pp. 418-424, 2012.
[217] Rahman, Q. I., Ahmad, M., Misra, S. K., and Lohani, M., "Effective photocatalytic degradation of rhodamine B dye by ZnO nanoparticles", *Materials Letters*, vol. 91, pp. 170-174, 2013.
[218] Hoshino, N., Kimura, T., Hayakawa, F., Yamaji, A., and Ando, T., "Bactericidal activity of catechin-copper (II) complexes against Staphylococcus aureus compared with Escherichia coli", *Letters in Applied Microbiology*, vol. 31, pp. 213-217, 2000.
[219] Hu, C. H. and Xia, M. S., "Adsorption and antibacterial effect of copper-exchanged montmorillonite on Escherichia coli K88", *Applied Clay Science*, vol. 31, pp. 180-184, 2006.
[220] Gomes, G. A., da Costa, G.L. and da Silva Figueiredo, A.B.H., "Synthesis of ferrite nanoparticles $Cu_{1-x}Ag_xFe_2O_4$ and evaluation of potential antibacterial activity", *Journal of Materials Research and Technology*, vol. 7(3), pp. 381-386, 2018.